Petrography and U-Pb SHRIMP zircon geochronology of basement samples from a key area in central Dronning Maud Land, East Antarctica:

Implications for the eastern extension of the Grenville-age Maud Belt in Antarctica

Master of science thesis in Geoscience

Stephen Larsen

Department of Earth Science

University of Bergen

2017

Abstract

Central Dronning Maud Land, East Antarctica represents a key area for the understanding of previous supercontinent assemblies. This study reports U/Pb SHRIMP ages and petrographic descriptions for nine samples collected in central Dronning Maud Land during the GeoMaud 1995/96 expedition in East Antarctica. This study further densifies an interesting area with limited previous geochronological data. The new U/Pb ages reveal basement crystallisation ages ranging between ca. 1130–1025 Ma, indicating that the study area is a part of the Mesoproterozoic Maud Belt that formed along the margin of the Kalahari Craton. This is further supported by petrographic characteristics that reveal granodioritic to tonalitic protolithic compositions, indicating that the basement formed within a volcanic arc system. Subsequent metamorphism during the Late Mesoproterozoic was not recorded in this study. No igneous or metamorphic activity was present between ca. 1025–650 Ma. Mafic igneous formation prior to metamorphism was recorded at ca. 637 and 613 Ma. This could imply that the Mozambique ocean was not fully closed at that time. Subsequent Late Neoproterozoic/Early Paleozoic U/Pb ages recorded metamorphic ages at two different stages at ca. 590–550 Ma and ca. 530–510 Ma. These events are characterised by high-grade metamorphism. Petrographic characteristics point towards granulite facies metamorphism related to the "Pan-African" event during collision between parts of East and West Gondwana. Limited evidence points to earliest metamorphic age recorded at ca. 611 Ma, earlier than previously assumed. Recent aeromagnetic surveys revealed the sub-ice boundary between the Maud Belt and the Tonian Oceanic Arc Super Terrane (TOAST). This anomaly projects into central Dronning Maud Land. However, this study reveals that all samples belong to the Mesopreoterozoic Maud Belt, and that this boundary is not present within the study area. Thus, the boundary must be located slightly further east than previously proposed.

Acknowledgements

I extend my absolute gratitude to my supervisors Prof. Joachim Jacobs and Dr. Anna Ksienzyk for great supervision throughout my M.Sc. project at the University of Bergen. I am grateful that Joachim Jacobs gave me the opportunity to work on this interesting and challenging project, and for critical discussions and feedback during important stages during my studies. I thank Anna for support during sample preparations, and excellent, constructive feedback.

Thank you to Irina Dumitru for preparing the thin sections, and Martina Suppersberger Hamre for helping and introducing me to all stages of mineral separation. My gratitude extends to Hallgeir Sirevaag and Johannes Wiest for critical reviews and discussions. I would like to thank Fernando Bea for providing me with images from the SHRIMP Ion Microprobe Laboratory of The University of Granada. I thank the team at the Laboratory for mounting, preparation and analysis of the samples.

I would like to thank the team at FT-Bergen team for good discussions, support and cooperation.

Thank you to the group at Hjørnerommet for excellent company and good times during the writing process. I also thank my partner Vilde Nesbø Bakke for her support and discussion throughout the time of my master project, and for reviews on several parts of this project. Lastly, I would like to thank my family for the support through my time as a student at the University of Bergen.

Bergen, 26.05.2017

Stephen Larsen

Contents

1. Introduction

Antarctica is the southernmost continent on Earth. It covers a large area of ca. 14,000,000 square kilometres. About 98% of the continent is covered by ice, making geological surveys difficult, as only a few outcrops are exposed throughout Antarctica. With modern technology, using aeromagnetic surveys, new geophysical data have been presented and give an insight into the sub-glacial geology of the continent. In combination with field work, the understanding of the Antarctic continent has improved tremendously over the years. Antarctica is now regarded as an important continent within the Precambrian and Paleozoic supercontinent assemblies

1.1 Study Area

This project is located in Dronning Maud Land. This part of East Antarctica is situated between 20° west and 45° east, covers an area of 2,700,000 square kilometres and is claimed by Norway. The study area is situated in the northern part of central Dronning Maud Land, between 8–14° east (Fig. 1.1). Samples were collected within Orvinfjella and Wohlthatmassiv (Fig. 1.1).

1.2 Aim of study

This project was aimed at further constraining the nature of the basement within central Dronning Maud Land (DML). U/Pb SHRIMP geochronology and petrography on nine samples collected during the GeoMaud 1995/96 expedition to East Antarctica, will provide new data on an area where only a limited number of U/Pb ages have been published. These new ages will help us to determine whether this basement province consists entirely of the Mesoproterozoic Maud Belt, as previously assumed. Recent aeromagnetic surveys within Dronning Maud Land have revealed a major linear magnetic anomaly (the Forster Magnetic Anomaly) that can be traced from an area east of western Dronning Maud Land, continuing north-eastward, projecting into the area of this study. The Forster Magnetic Anomaly (FMA), is interpreted to represent the main boundary between the Maud Belt within central and western Dronning Maud Land, and the Tonian Oceanic Arc Super Terrane (TOAST) in SE Dronning Maud Land. The FMA is separating two fundamentally different basement provinces with contrasting U/Pb ages and geochemical properties. This magnetic anomaly abruptly stops just south of the study area, and it has recently been suggested that the main boundary between the two terranes might be within the Orvinfjella and Wohlthatmassiv region. Hence, new U/Pb data from this area might reveal whether this boundary is present in this region.

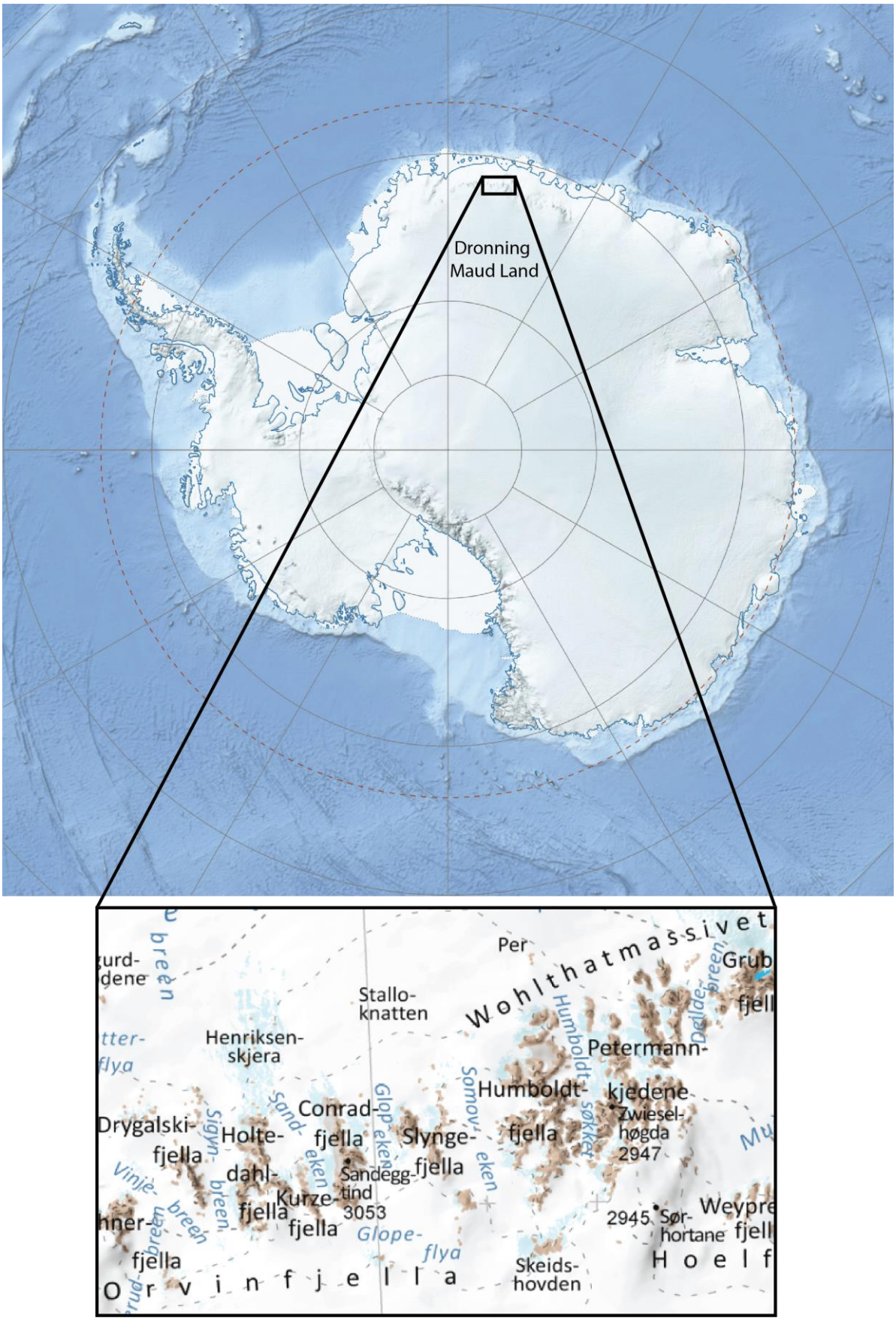

Fig. 1.1: Map of Antarctica, with the study area marked with a black rectangle. The bottom image shows the study area of this project. Figure modified from NPI, 2017 (Downloaded from: http://www.npolar.no/en/services/maps/printed/topographic-antarctica.html).

A secondary aim of this project is to determine whether metamorphic ages older than ca. 570 Ma are present in this region. In the Schirmacher Oasis, north of the study area (Fig. 2.1), metamorphic ages as old as ca. 625 Ma have been reported. These older ages are so far unknown from the study area of this project. New U/Pb dating could bring evidence of metamorphic overprinting prior to what has previously been assumed.

1.3 Previous Studies

As previously mentioned, very limited geochronological data have been published within the study area. The first geological studies were done by soviet geologists in the 1960s. They produced reconnaissance geological maps, summarised in Ravich and Solov' ev (1966), Ravich and Kamenev (1972) and Kamenev et al. (1990). East German and Indian expeditions in the early 1990s were focused on the Schirmacher Oasis area, the Grubergebirge and the Schüssel area. This work is summarised in Bormann and Fritzsche (1995), Joshi et al. (1991) and Kaul et al. (1991). Mikhalsky et al. (1995) reported three conventional U/Pb ages within the area, where a felsic gneiss with metamorphic zircons yielded and age of 588 ± 4 Ma. Another sample of post tectonic syenite recorded a U/Pb crystallisation age of 512 ± 2 Ma and a mafic schist recorded 570 ± 4 Ma (Mikhalsky et al., 1995). The first thorough geochronological study was published by Jacobs et al. (1998). They reported U/Pb SHRIMP ages for 12 samples, where metavolcanic basement samples recorded ages ranging from ca. 1130–1070 Ma. These ages were interpreted to represent the time of basement crystallisation (Jacobs et al., 1998). The crystallisation of the basement was subsequently followed by metamorphic zircon re-crystallisation at ca. 1085–1075 Ma (Jacobs et al., 1998). Following this event, charnockite and anorthosite intruded the Mesoproterozoic basement at ca. 600 Ma and 585 Ma (Jacobs et al., 1998). The intrusive activity was followed by medium to high-grade metamorphism reaching granulite facies during two periods at ca. 570–550 and ca. 530–515 Ma (Jacobs et al., 1998). Late tectonic activity was based on metagranodiorite emplacement at ca. 530 Ma (Jacobs et al., 1998).

2. Geological and Geodynamic Framework

The ages of the geological domains of East Antarctica span several billions of years. Three main age groups are present within the East Antarctic continent: Cratonic fragments with ages of ca. 3000 Ma, Late Mesoproterozoic/Early Neoproterozoic (LM/EN) ages ranging from ca. 1300–900 Ma, and Late Neoproterozoic/Early Paleozoic (LN/EP) ages between ca. 650–490 Ma (Fitzsimons, 2000a; Pierce et al., 2014). In East Antarctica, four Archean cratonic fragments crop out in the Grunehogna Craton, the Shackleton Range, the Ruker Craton and the Napier Craton (Fig. 2.1). Due to the ice-covered bedrock, the extent of the cratonic fragments is not well constrained. Paleoproterozoic basement such as the Øygarden Group, Lambert Terrane and Coats Land Block is exposed, often close to the cratonic fragments (Fig. 2.1). Mesoproterozoic basement rocks are exposed in the Maud Belt (western and central Dronning Maud Land) and in the Rayner Province (east of Lützow Holm Complex) (Fig. 2.1). Most of the basement rocks from the Rayner Province to Shackleton Range show LN/EP metamorphic overprinting to varying degrees.

The geological evolution of East Antarctica is affected by several major orogenic events that are summarised within this chapter.

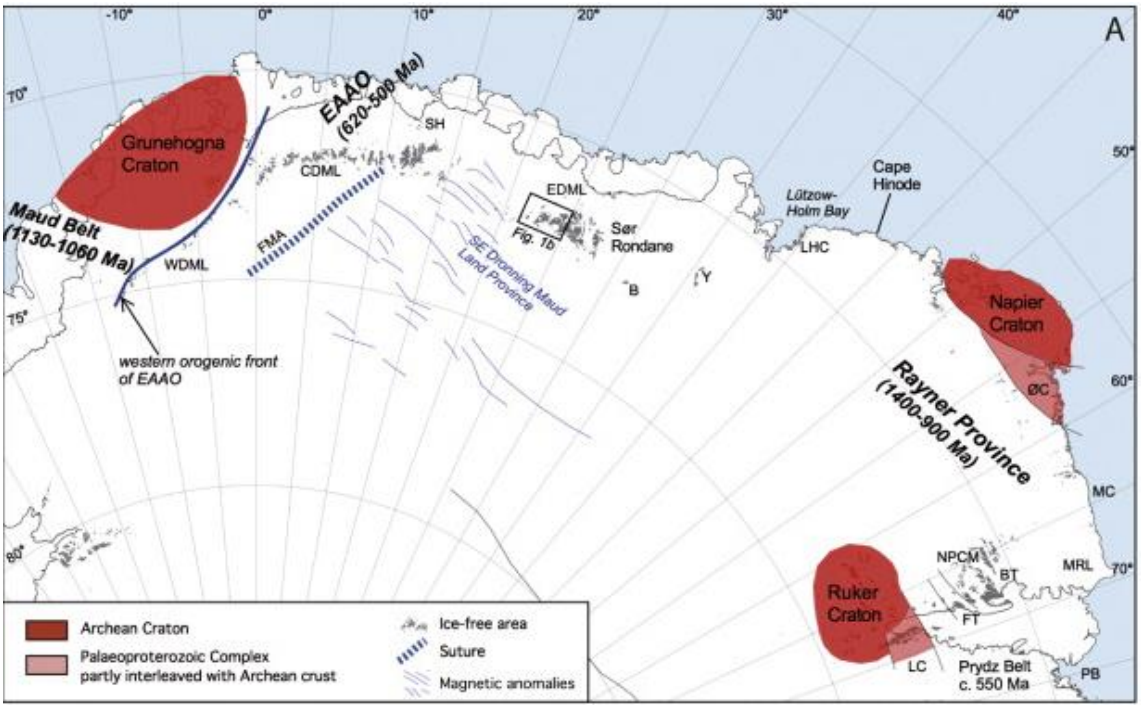

Fig. 2.1: Overview map of the main geological provinces of East Antarctica with cratonic fragments in red. Abbreviations: B - Belgica Mts.; BT - Beaver Terrane; CDML – Central Dronning Maud Land; EAAO - East African-Antarctic Orogen; EDML – Eastern Dronning Maud Land; FT - Fischer Terrane; LC - Lambert Complex; LHC - Lützow-Holm Complex; MC - Mawson Coast; MRL - Mac. Robertson Land; NPCM - northern Prince Charles Mts.; PB - Prydz Bay; SH - Schirmacher Oasis; WDML - western Dronning Maud Land; Y - Yamato Mts; ØC - Øygarden Complex; C – Coats Land. Figure from Elburg et al. (2015)

2.1 East Antarctica and the Kalahari Craton within Rodinia

It has been proposed that the accretion and orogenic events during the Mesoproterozoic and early Neoproterozoic (ca. 1300–900 Ma) were the result of the formation of the supercontinent Rodinia (Hoffman, 1992). The assembly of the supercontinent Rodinia caused worldwide orogenic events between 1300 Ma and 900 Ma, connecting all continents known at that time to form this Late Mesoproterozoic supercontinent (Li et al., 2008). The first recognition of a possible Precambrian supercontinent was made by Valentine and Moores (1970). Li et al. (2008) undertook a comprehensive review of the various existing models of the Rodinia supercontinent (e.g. AUSMEX, AUSWUS, SWEAT and “Missing Link”). The model that Li et al. (2008) proposed is based on the "Missing-Link" model that was first described by Li et al. (1995) where the south China block was juxtaposed between the East Antarctic continent and Laurentia. The “Missing Link” model was proposed based on several mismatches with the SWEAT hypothesis form (Dalziel, 1991; Hoffman, 1991; Moores, 1991). The SWEAT model, proposing a connection between Laurentia, Australia and East Antarctica, was suggested by Bell and Jefferson (1987), based on stratigraphic correlations and palaeomagnetic constraints across the Pacific. Eisbacher (1985) came to similar conclusions based on stratigraphic correlations alone. The exact configuration of the continents within Rodinia is still a matter of debate, and the latest review by Dalziel (2013) points to new evidence for the Southwest US–East Antarctica (SWEAT) hypothesis (Fig. 2.2). This new evidence is based on ca. 1200–900 Ma zircon populations from glacial deposits in the Transantarctic Mountains that could be related to a ca. 1.1 Ga orogenic extension from western Laurentia and into East Antarctica (Goodge et al., 2010). This connection is further supported by similar ages and geochemical properties in granites from both East Antarctica and Laurentia (Goodge et al., 2008). Furthermore, the Umkondo Large Igneous Province (LIP) in the Grunehogna Craton further supports the East Antarctica-Laurentia connection (Jacobs et al., 2008b). The Umkondo LIP was situated on the Kalahari Craton and was active at 1112–1106 Ma. These correlate with age, rock types and Pb-isotopes compared to the Kaweenawan LIP located in Laurentia (Loewy et al., 2011).

The position of the Kalahari Craton and East Antarctica according to the SWEAT hypothesis during the formation of Rodinia is shown in Fig. 2.2.

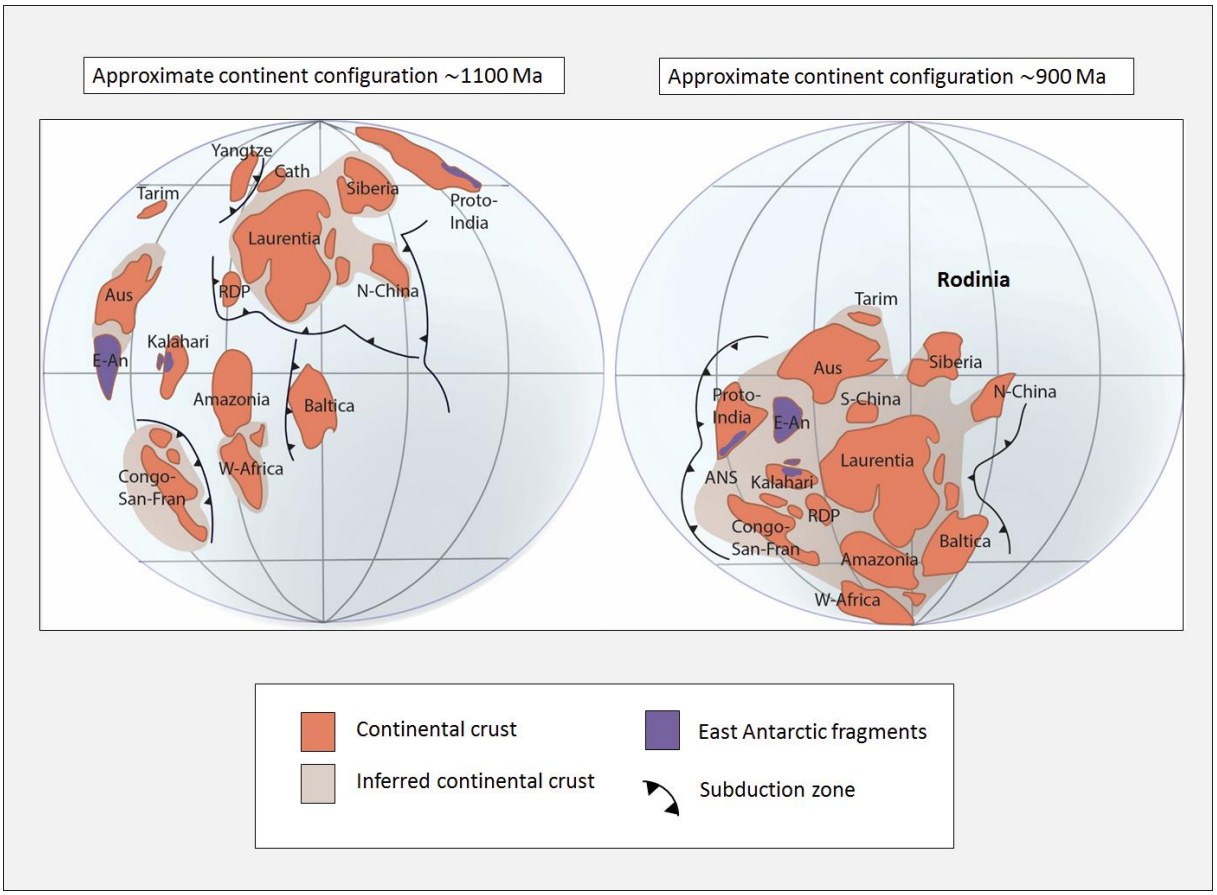

Fig. 2.2: A possible configuration of the supercontinent Rodinia at ca. 1100 Ma and ca. 900 Ma. This model is based on the SWEAT hypothesis (Dalziel, 1991; Hoffman, 1991; Moores, 1991). Abbreviations: N-China – North China; S-China – South China; RDP – Rio De La Plata; W-Africa – West Africa; ANS – Arabian-Nubian Shield; E-An – East Antarctica; Aus – Australia; Cath – Cathaysia; Congo-San-Fran – Congo-San-Fransisco. Figure from Li et al. (2008).

2.1.1 The formation of the western and central Dronning Maud Land basement

The basement rocks of western and central Dronning Maud Land formed within a mature island arc setting along the eastern margin of the Kalahari Craton at ~1.1 Ga (Bauer et al., 2003b; Jacobs et al., 2008a; Jacobs et al., 1998). Subsequently, the rocks underwent the first high-grade metamorphic event coupled with emplacement of large syntectonic granitoid bodies between ca. 1090 and 1060 Ma (Arndt et al., 1991; Jacobs et al., 1998). The regional metamorphism marked a collisional event that incorporated Dronning Maud Land within Rodinia (Jacobs et al., 2008a). The Kalahari Craton evolved from Proto-Kalahari that consists of smaller Archean cratonic fragments (Zimbabwe Craton, Kaapvaal Craton (Africa) and the Grunehogna Craton (western DML) (ZKG)) (Jacobs et al., 2008b). Proto-Kalahari likely formed a single entity during the latest

Mesoproterozoic (e.g. Gose et al., 1997; Jones et al., 2003; Peters et al., 1991) (Fig. 2.3). During the formation of Rodinia in the Mesoproterozoic, the Proto-Kalahari Craton underwent a period of major crustal growth related to the formation of island arcs along the north-western, south-western and southern margin (e.g. Becker et al., 2006; Jacobs et al., 1993; Thomas et al., 1994) (Fig 2.4).

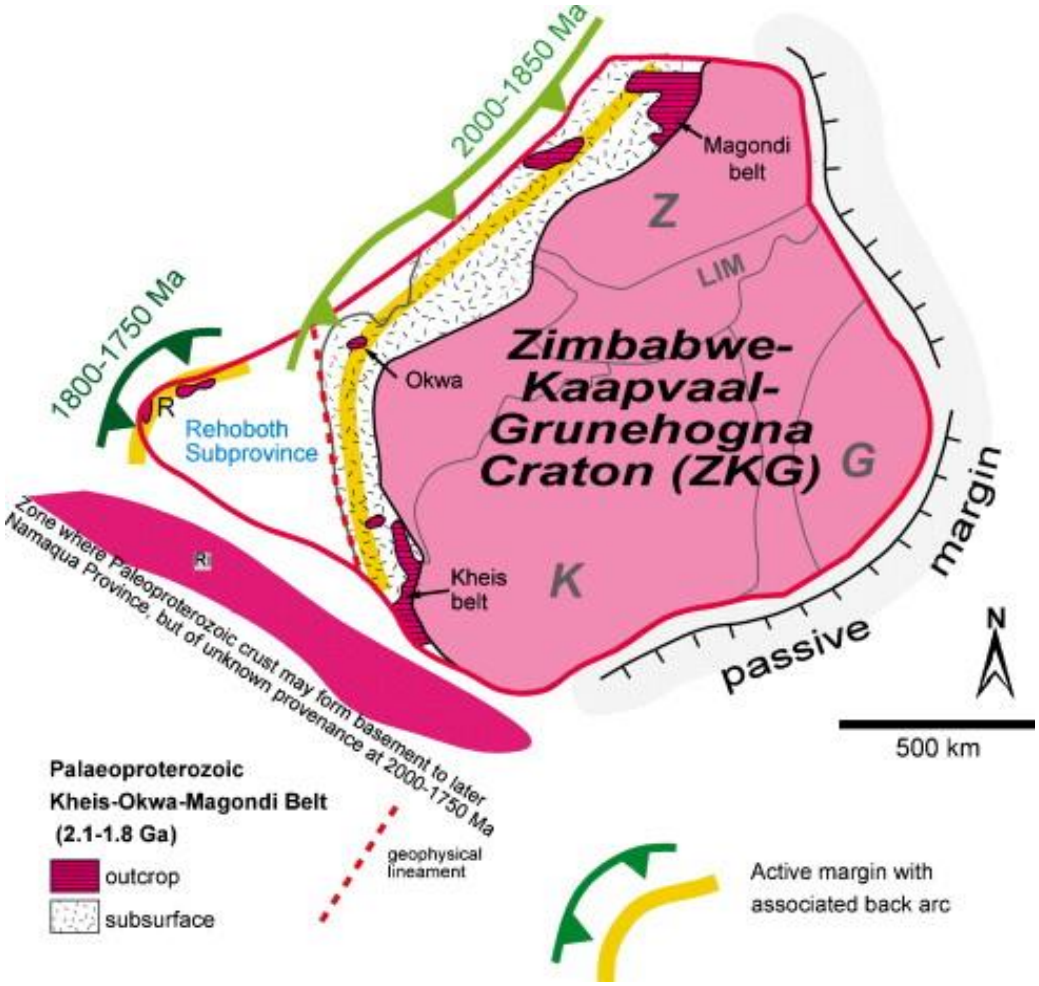

Fig. 2.3: Palaeogeographic reconstruction of the Proto-Kalahari Craton at ca. 1750 Ma. Abbreviations: G - Grunehogna Craton; K - Kaapvaal Craton; LIM - Limpopo Belt; R - Rehoboth; Ri - Richtersveld; Z - Zimbabwe Craton. Figure from Jacobs et al. (2008b).

This major crustal growth around the Proto-Kalahari Craton resulted in almost a doubling in size of the craton (Jacobs et al., 2008b), forming the Kalahari Craton. The colliding counter-part during the amalgamation of Rodinia is, as of yet an ongoing debate (Jacobs et al., 2008b). Several authors have proposed various positions of the Kalahari Craton (e.g. Collins and Pisarevsky, 2005; Dalziel, 1991; Gose et al., 1997; Hanson et al., 1998; Hoffman, 1991; Jacobs et al., 2003*a*; Jacobs et al., 1996; Jacobs et al., 1997; Powell et al., 2001a; Powell et al., 2001b). Many reconstructions position the Kalahari Craton

in contact with either western Australia (WAlahari) or Laurentia (Fitzsimons, 2003; Pisarevsky et al., 2003; Powell and Pisarevsky, 2002). However, new evidence was presented by Ksienzyk and Jacobs (2015), indicating that the WAlahari connection was unlikely based on detrital zircon analyses. Therefore, a collision of the Kalahari Craton with south-western Laurentia is a more likely scenario (Ksienzyk and Jacobs, 2015).

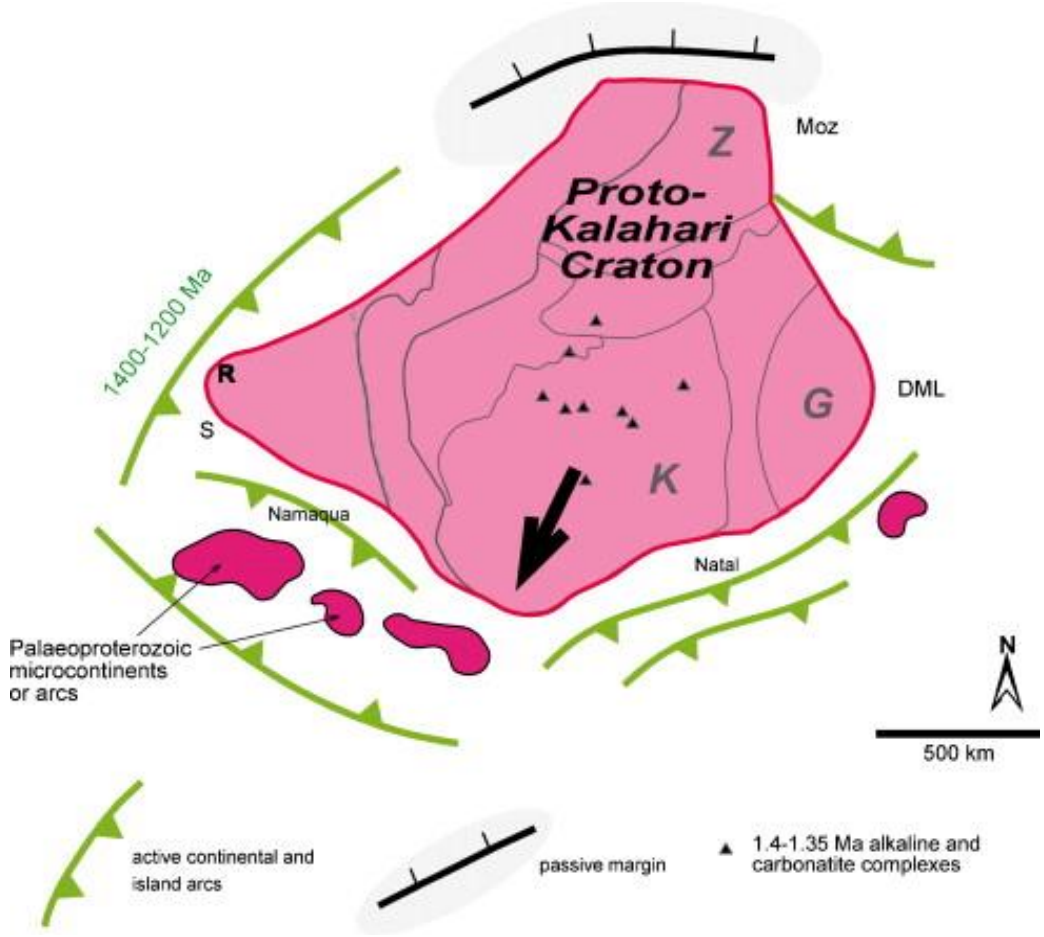

Fig. 2.4: Palaeogeographic reconstruction of the Proto-Kalahari Craton at 1200 Ma. Large island arc terranes along the southwestern, southern and southeastern margins of the Proto-Kalahari Craton are later accreted to Proto-Kalahari during major crustal growth during the formation of Rodinia. Abbreviations: G - Grunehogna Craton; DML - Dronning Maud Land; K - Kaapvaal Craton; Moz - northern Mozambique; R - Rehoboth; S - Sinclair; Z - Zimbabwe Craton. Figure from Jacobs et al. (2008b).

The Mesoproterozic basement in western and central Dronning Maud Land formed along the eastern and south-eastern margin of the Kalahari Craton, and subsequently amalgamated to the Kalahari Craton, forming the Namaqua-Natal-Maud Belt (Jacobs et al., 1993; Thomas et al., 1994) as a result of continent-continent collision (Fig. 2.5). During the main collision with either western Australia or Laurentia, metamorphic overprinting in the Namaqua-Natal-Maud belt occurred between ca. 1200–1000 Ma (Jacobs et al., 1998; Jacobs et al., 2008b; Jacobs et al., 1993; Thomas et al., 1994).

The Namaqua-Natal-Maud belt can today be traced through the southern margin of the Kalahari Craton (south-east Africa) and into Dronning Maud Land (East Antarctica), forming the western and central DML basement (Jacobs et al., 2008b).

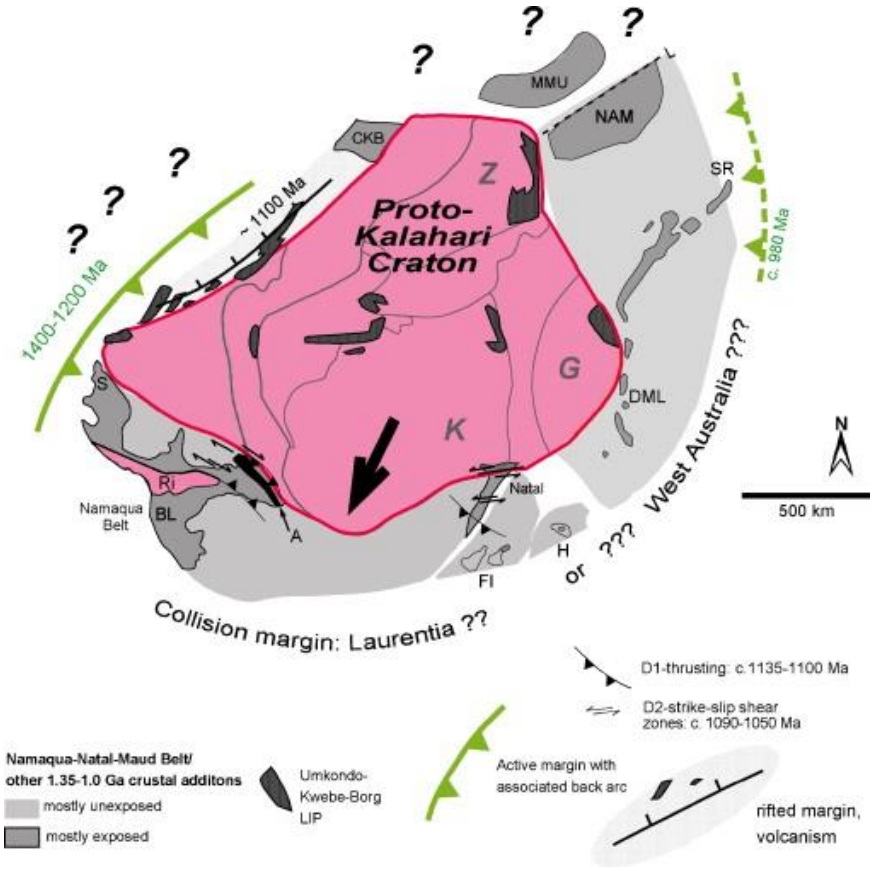

Fig. 2.5: Palaeogeographic reconstruction of the Proto-Kalahari Craton at 1080 Ma, showing collision and accretion during the formation of Rodinia. The Proto-Kalahari Craton collided with either Laurentia or West Australia. Abbreviations: A - Areachap terrane; BL - Bushmanland Terrane; CKB - Choma-Kaloma Block; FI - Falkland Islands; G - Grunehogna Craton; DML - Dronning Maud Land; H - Haag Nunatak; K - Kaapvaal Craton; L - Lurio Belt; MMU - Marupa–Malawi–Unango terrane; NAM - Nampula Province; S - Sinclair; SR - Sør Rondane; R - Rehoboth; Ri - Richtersveld; Z - Zimbabwe Craton. Figure from Jacobs et al. (2008b).

2.2 The assembly of various parts of East and West Gondwana

The assembly of various parts of East and West Gondwana was accomplished by a complex series of accretions and collisions between various continental fragments. West Gondwana assembled simply by amalgamation of the South-American continent to West-Africa at ca. 600 Ma, compared with a more complex situation during the amalgamation of East Gondwana (Fitzsimons, 2000b; Meert and Van Der Voo, 1997). East Gondwana

consists of the Arabian-Nubian Shield, Proto-India, Madagascar, Seychelles, Sri Lanka, a significant part of East Antarctica and Australia.

The accretion and collision between the continents forming East Gondwana, and subsequently colliding with West Gondwana, marks the formation of the supercontinent Gondwana (ca. 650–500 Ma) (Stern, 1994).

For the formation of Gondwana, Meert (2003) proposed a model which is based on a two-stage assembly. This model proposes that two major orogens formed during the amalgamation. This idea was later supported by Grantham et al. (2008). The first orogen resulted from collision and accretion of the Arabian-Nubian shield, followed by oblique collision with eastern Africa, Madagascar, Sri Lanka, Seychelles and India at ca. 750–620 Ma. This formed the N-S oriented East African Orogen (EAO) (Stern, 1994). The second orogen formed as a result of oblique collision between East Antarctica, Australia and the Rayner Province with the Kalahari Craton and Eastern India at ca. 570–530 Ma. This event formed the orogen known as Kuunga Orogen (Meert et al., 1995). The collision forming the Kuunga Orogen, intersecting with the EAO, marks the final assembly of Gondwana (Meert, 2003). Traces of the southern extent of the EAO (Mozambique Belt), into Dronning Maud Land were first proposed by Shiraishi et al. (1994), and later supported by the work of Jacobs et al. (1998). This was based on striking similarities in the LN/EP metamorphic overprinting in the DML basement and in the Mozambique Belt (Jacobs et al., 1998). This has been further supported by Jacobs et al. (2008a), linking voluminous granitoid intrusions related to the orogenic collapse in both Dronning Maud Land and in northern Mozambique.

Based on the likely southern extent of the East African Orogen (Stern, 1994), Jacobs and Thomas (2004) suggested to use the name East African-Antarctic Orogen (EAAO).

2.2.1 The “Pan-African” orogenic event

The Pan-African orogenic event occurred during the formation of the supercontinent Gondwana. The term “Pan-African” was first used by Kennedy (1964), and was then interpreted as a tectono-thermal event around 500 Ma. However, later studies from Kröner (1984) recognised this as the final stage of the orogenic cycle, and the term “Pan-African” has since then been extend to describe the tectonic, magmatic and metamorphic events of Neoproterozoic to earliest Paleozoic age. The Pan-African orogenic event therefore describes the orogenic cycle with accretion of microcontinents and collision of

several continental blocks, as well as closure of major oceans during the period between ca. 870–550 Ma. These events formed the extensive East African-Antarctic Orogen between East- and West Gondwana (Dalziel, 1991; Kröner and Stern, 2004).

2.2.2 The East African-Antarctic Orogen (EAAO)

The East African-Antarctic orogen is an extensive orogenic belt stretching from Arabia in the North, following along the African margin, and into East Antarctica (Fig. 2.6). The EAAO formed the main collisional orogen between parts of East and West Gondwana during the "Pan-African" event, resulting in the massive orogen that extends over ~ 8000 km (Jacobs et al., 1998; Jacobs and Thomas, 2002; Jacobs and Thomas, 2004; Shackleton, 1996; Stern, 1994). As previously addressed, the northern extent of the EAAO consists of the accretionary Arabian-Nubian Shield, and the southern extent consists of the Mozambique Belt, characterised by continent-continent collision. The Mozambique Belt continues into East Antarctica in the southern extent (Jacobs et al., 1998; Jacobs and Thomas, 2002; Jacobs and Thomas, 2004; Muhongo and Lenoir, 1994; Stern, 1994). The EAAO has been compared with a Tibetan-style continental collision (Burke and Dewey, 1972), with comparable crustal thickening. The entire orogen formed in a major sinistral transpressional setting during the formation of Gondwana. In the southern extent of the EAAO, a southward-directed escape tectonic model, similar with the modern Himalayan-type has been proposed by Jacobs and Thomas (2004), within the southern margin of the Kalahari Craton, as well as in East Antarctica (Fig. 2.7). This was based on several points of evidence, including the presence of major dextral transpressive structures in the Heimefrontfjella in an overall sinistral shear setting, as well as the Coats Land block that represents a crustal entity within the orogen which not subjected to "Pan-African" metamorphic overprinting. This would indicate that the Coats Land block was subjected to significant tectonic translation (Jacobs and Thomas, 2004).

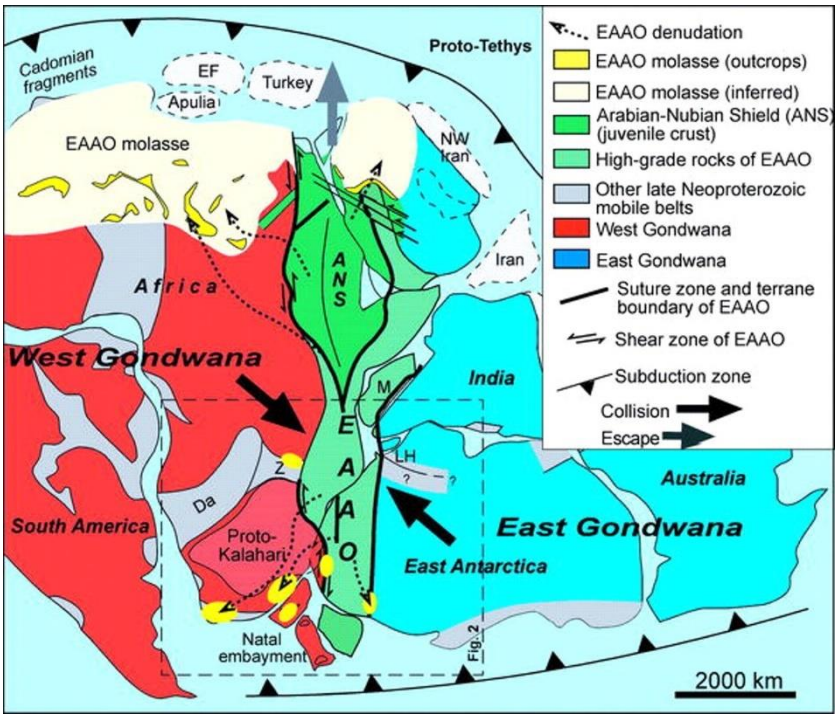

Fig. 2.6: East African-Antarctic Orogen (EAAO), forming the main collisional orogenic belt between East and West Gondwana. Abbreviations: ANS - Arabian-Nubian shield; Da - Damara belt; EF - European fragments; LH - Lützow-Holm Bay; M - Madagascar; Z - Zambesi belt. Figure from Jacobs and Thomas (2004).

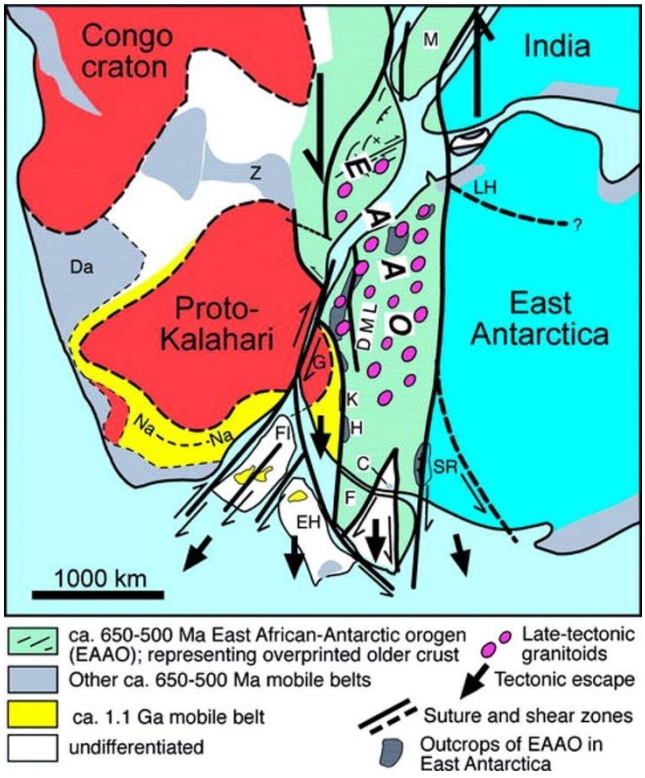

Fig. 2.7: Escape tectonics model for the southern part of the EAAO. Abbreviations: C - Coats Land; DML - Dronning Maud Land; EF - European fragments; EH - Ellsworth-Haag; F - Filchner block; FI - Falkland Islands; G - Grunehogna; H - Heimefrontfjella; K - Kirwanveggen; Na-Na - Namaqua-Natal; SR - Shackleton Range; ANS - Arabian-Nubian shield; Da - Damara belt; LH - Lützow-Holm Bay; M - Madagascar; Z - Zambesi belt. Figure from Jacobs and Thomas (2004).

The Arabian-Nubian Shield (ANS)

The Arabian-Nubian shield (ANS) represents the northern accretionary part of the East African-Antarctic Orogen (Fig. 2.6). It extends over ~3000 km from north to south with a width of > 500 km on both sides of the red sea (Kröner and Stern, 2004). The formation of the Arabian-Nubian shield was a result of several accretions of arc terranes spanning a period of ca. 100 Ma that started 750 Ma ago (Blasband et al., 2000). It is characterised by the collage of juvenile Neoproterozoic crustal units such as old ophiolites as well as island arcs (Meert, 2003; Stern, 1994). The Arabian-Nubian shield is distinct from the Mozambique belt with characteristically lower metamorphic grade, and its juvenile Neoproterozoic nature. The ophiolitic units represent the earliest record of major ophiolitic units on earth (Kröner and Stern, 2004; Stern, 1994).

The Mozambique Belt (MB)

The Mozambique belt (MB) is recognised by medium to high-grade metamorphic gneisses and voluminous granitoids that stem from old Mesoproterozoic and Archean crust that was highly reworked during the Pan-African orogenic event (Kröner and Stern, 2004). It represents the southern part of the EAAO, and extends southward from the ANS, into southern Ethiopia, Kenya, Somalia, via Tanzania to Malawi and Mozambique and into central Dronning Maud Land, East Antarctica (Jacobs et al., 1998). The Mozambique belt is also recognised in the southern tip of India as well as Madagascar (Kröner and Stern, 2004) (Fig. 2.8). The northern part of the Mozambique belt is, similar with Dronning Maud Land, characterised by voluminous post-orogenic granitoid intrusions with similar ages (Jacobs et al., 2008a).

In the northern part of the Mozambique Belt, the NE/SW trending Lurio Belt is interpreted to represent the suture zone between the Kalahari Craton and the Congo-Tanzania Craton, i.e the Kuunga Orogeny, extending and intersecting with the Mozambique belt (Bingen et al., 2009) (Fig. 2.8).

The Mozambique Belt formed the orogen that connected the Congo-Tanzania Craton and the Kalahari Craton with the Indian Craton, East Antarctica, Madagascar and Sri Lanka (Fig. 2.8).

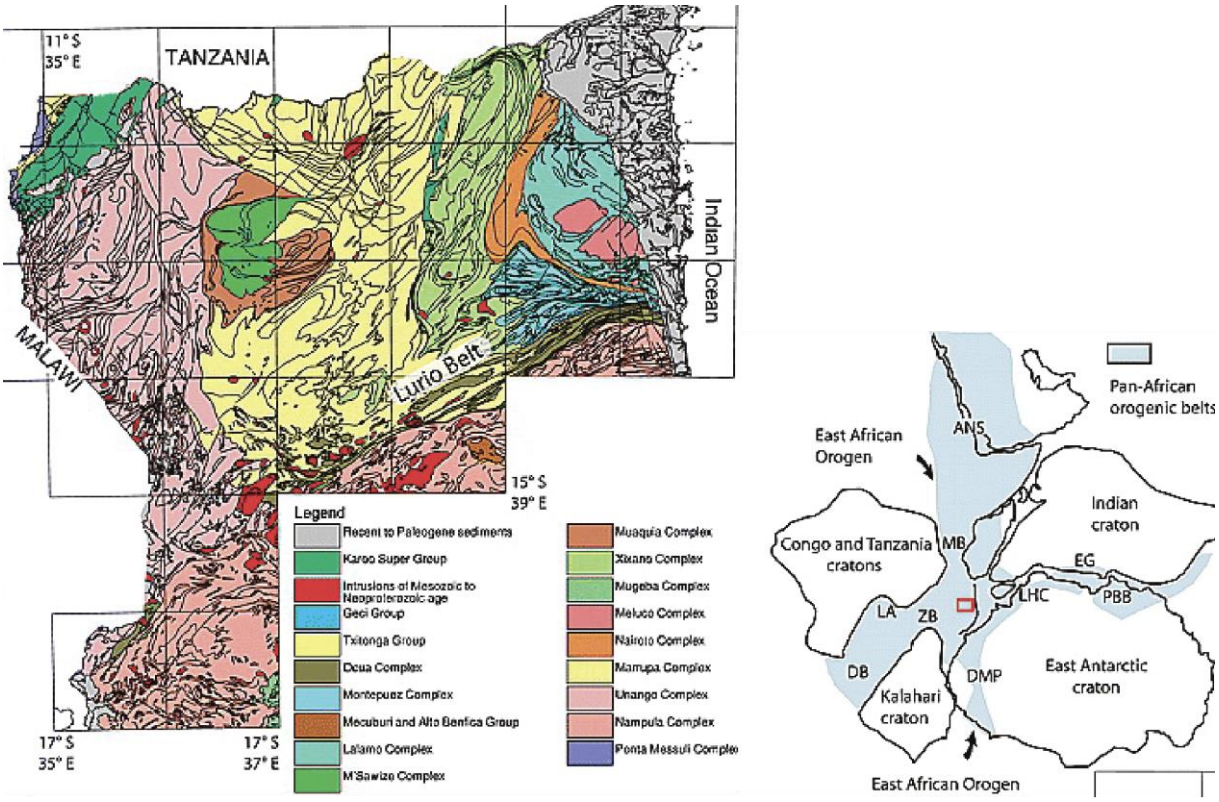

Fig. 2.8: The Lurio Belt likely represents the suture zoned between the Kalahari Craton and the Congo-Tanzania Craton. The red rectangle shows the position of the map relative to the continents' positions in Gondwana. Figure from Viola et al. (2008).

2.3 The geology of Dronning Maud Land, East Antarctica

2.3.1 Western Dronning Maud Land

The north-westernmost part of Dronning Maud Land consists of the Grunehogna Craton dated by Rb-Sr and Pb-isotopes to ca. 3.0 Ga (Barton et al., 1987). Located East of the Grunehogna Craton are the Mesoproterozoic basement rocks of the Maud belt, with a strong LN/EP overprinting (Jacobs et al., 1998). The basement rocks of the Maud Belt are, as previously addressed, metavolcanics rocks that formed within mature island arcs or continental arcs (Grosch et al., 2007; Jacobs et al., 1998). In the Heimefronfjella of western DML, a major ca. 20 km wide dextral shear zone (Hemefront Shear Zone (HSZ)) separates the typical Maud Belt (LN/EP overprinted) rocks from the Natal province which is characterised by Late Mesoproterozoic/Early Neoproterozoic crust unaffected by LN/EP overprinting (Jacobs et al., 2003*a;* Jacobs et al., 1996).

The relationship between the Namaqua-Natal Belt and The Maud Belt is still a matter of debate, and various authors have previously proposed that they formed within the same arc system around the Kalahari Craton (e.g. Grantham et al., 1995; Groenewald et

al., 1995; Jackson, 1999). These models linked the southern arcs of the Namaqua-Natal sector with the Maud Belt sector in previous models (Groenewald et al., 1991; Jacobs et al., 1993). However, studies from Frimmel (2004) and Mendonidis et al. (2015), further separate the Namaqua-Natal Belt from the Maud Belt, based on U/Pb ages of ca. 1200 Ma in the Namaqua-Natal province, compared with the typical ca. 1100 Ma ages of the Maud Belt. This would indicate that the Namaqua-Natal Belt probably formed within the southern margin of the Kalahari Craton, and probably amalgamated to the Kalahari Craton prior to the Maud Belt. This proposal is further supported in previous studies from e.g. Bauer et al. (2003b), Bisnath et al. (2006), Grosch et al. (2007) and Marschall et al. (2013), suggesting that the Maud Belt formed within a separate arc system where the subduction was directed beneath the Kalahari Craton, forming a continental arc or an island arc with a mixture of continental components and island arc components (Fig. 2.9). This proposal is based on inherited zircons, in combination with geochemical signatures of a continental arc system (Grosch et al., 2007).

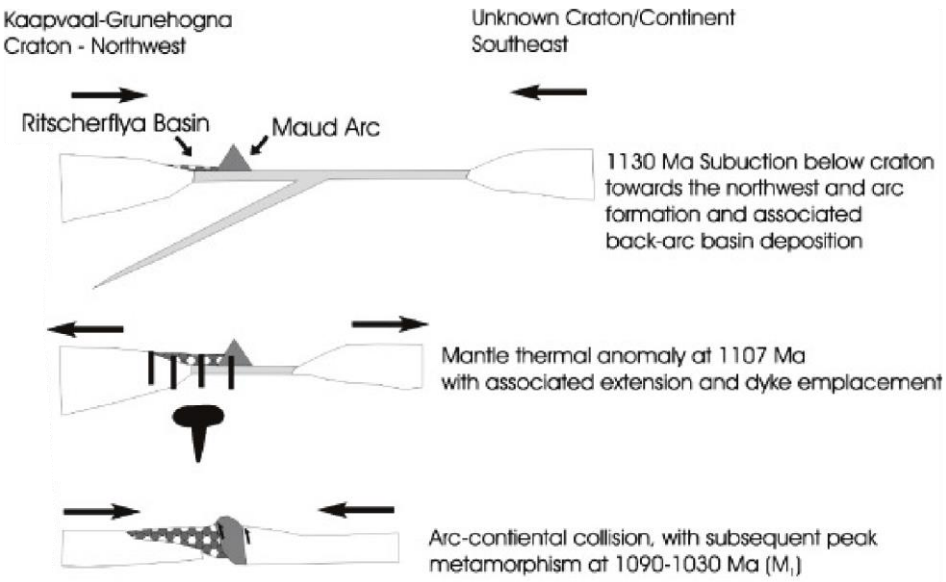

Fig. 2.9: Model depicting the formation of the Maud Belt with the subduction slab oriented beneath the Kalahari Craton. Figure modified from Bisnath et al. (2006).

2.3.2 Eastern Dronning Maud Land

The Sør Rondane Mountains (SRM) in eastern Dronning Maud Land are divided into two distinct terranes: the NE-Terrane and the SW-Terrane, subdivided by the Main Tectonic Boudary (MTB) (Osanai et al., 2013). The NE-Terrane of the SRM is characterised by mainly granulite facies metasupracrustal rocks with metamorphic ages

younger than ca. 750 Ma (Shiraishi et al., 2008). The supracrustal sequence has been deposited on top of an unknown basement that could be similar to the Rayner-type basement (Shiraishi et al., 2008). The granulite metamorphism in the NE-Terrane has been dated to ca. 640–600 Ma by U-Pb zircon geochronology (Osanai et al., 2013). Granulite metamorphism is associated with a clockwise PT-path, followed by amphibolite facies retrogression dated to ca. 590–530 Ma (Osanai et al., 2013).

The SW-Terrane is subdivided into two main parts, separated by the km-wide Main Shear Zone (MSZ). The northern terrane is characterised by a varied mix of volcano-sedimentary protoliths reaching greenschist to amphibolite facies that has island arc to continental margin-type geochemical characteristics (Ruppel et al., 2015). The southern terrane is characterised by a gabbro-trondhjemite-tonalite-granodiorite (GTTG) suite (Osanai et al., 2013). The crystallisation ages of these rocks range from ca. 995–920 Ma (Elburg et al., 2015; Ikeda and Shiraishi, 1998; Kamei et al., 2013; Shiraishi et al., 2008; Takahashi et al., 1990).

Contrasting PT-paths between the NE-Terrane (clockwise) and the SW-Terrane (counter clockwise), have been reported (Adachi et al., 2013; Baba et al., 2013; Osanai et al., 2013), and are interpreted as a result of the NE-Terrane thrusting over the SW-Terrane, thus representing a suture zone (Jacobs et al., 2015).

Recent work published by Jacobs et al. (2015) in the SE-DML province between Wohlthatmassiv (central DML) and the Sør Rondane Mountains revealed a previously unstudied terrane. This area consists of small nunataks in an otherwise largely ice-covered region. The analysed basement samples from this study revealed a juvenile basement sequence with crystallisation ages ranging from ca. 1000–900 Ma, followed by a LN/EP metamorphic overprinting at amphibolite to granulite facies (Jacobs et al., 2015). These rocks show similarities with the rocks of the SW-Terrane of the SRM, and are interpreted to represent the same oceanic arc domain forming the Tonian Oceanic Arc Super Terrane (TOAST) (Jacobs et al., 2015). The degree of metamorphism is what separates the SE DML (amphibolite to granulite) area from the SW-Terrane of SRM (greenschist to amphibolite) (Jacobs et al., 2015; Ruppel et al., 2015).

Aeromagnetic data (Mieth et al., 2014; Riedel et al., 2013) revealed that the study area of Jacobs et al. (2015) represents and extensive block in the SE DML Province. The new data indicate that this geophysically defined block probably represents the sub-ice continuation of major Tonian oceanic terranes, namely the Tonian Oceanic Arc Super Terrane (TOAST) (Jacobs et al., 2015). The western boundary of the TOAST is

represented by the Forster Magnetic Anomaly (FMA), which is interpreted as the main suture zone between the Maud Belt and the TOAST south of central Dronning Maud Land (Jacobs et al., 2015; Riedel et al., 2013).

The Forster Magnetic Anomaly (FMA)

The Forster Magnetic Anomaly (FMA) (Fig. 2.10) is located east of the Jutulstraumen, starting around 72°S/007°E, stretching as far south as approximately 75°S/1°W (Riedel et al., 2013). The NE/SW-striking anomaly is projecting towards the southern margin of the Kurze Mts. in the south-eastern margin of the study area of this project. The magnetic anlomaly does however abruptly stop just south of the study area of this project (Kurze Mts.), hence field work and analyses of samples from this key area would bring new insights into the nature of this boundary, and wether it in fact continues into this area (Riedel et al., 2013).

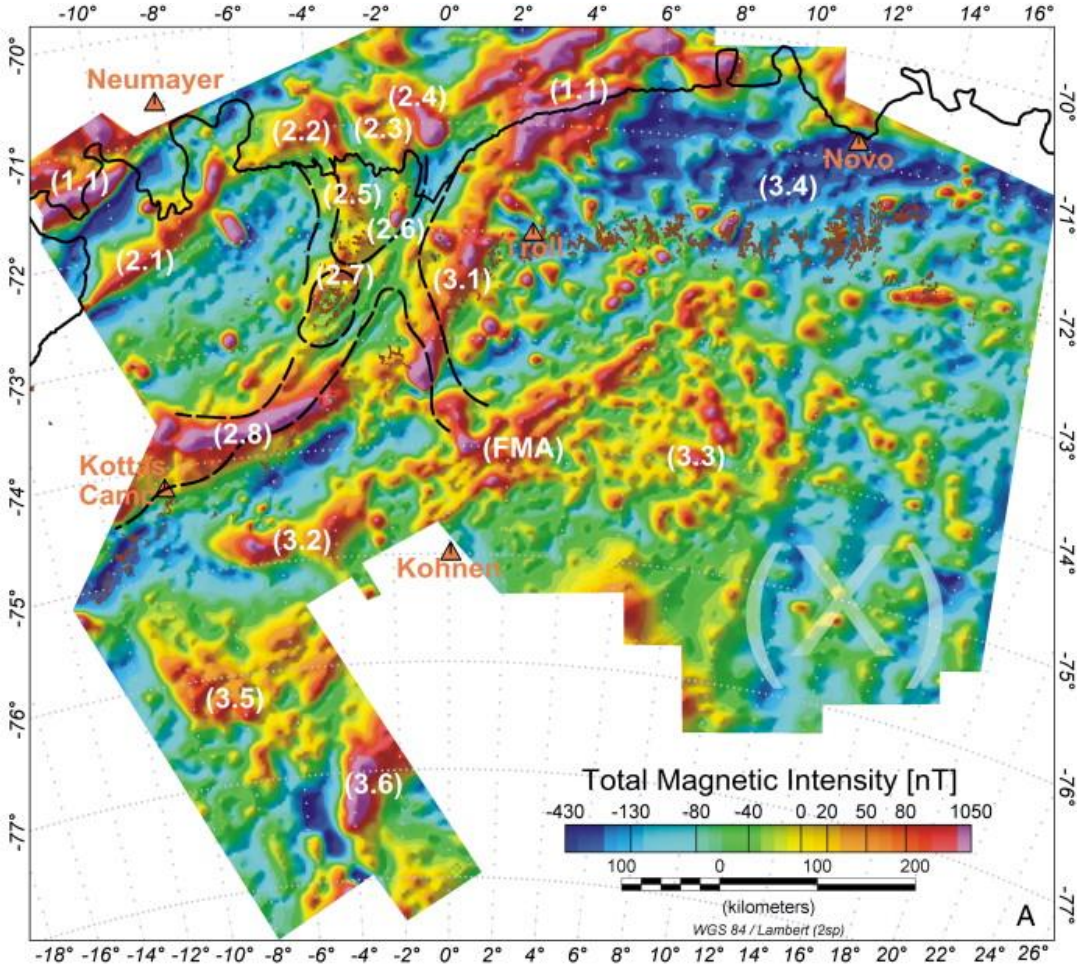

Fig. 2.10: Total magnetic intensity map of Dronning Maud Land. The Forster Magnetic anomaly is represented by the elongated anomaly in the centre of the map, stretching north-east towards central Dronning Maud Land. Figure modified from Riedel et al. (2013).

2.3.3 Central Dronning Maud Land

Central Dronning Maud Land shares many similarities with parts of western DML. The basement consists of Mesoproterozoic metavolcanics rocks that were subsequently metamorphosed at amphibolite to granulite facies at 1090 Ma (Jacobs et al., 1998). Central Dronning Maud Land is part of the Maud Belt and is characterised by a strong metamorphic LN/EP overprinting event related to the "Pan-African", reaching high-grade granulite facies throughout the area (Jacobs et al., 1998). The peak metamorphic event within central DML revealed U/Pb ages at ca. 570–550 Ma and ca. 530–515 Ma (Jacobs et al., 2003*b*).

Syn-tectonic anorthosite and charnockite intrusions (ca. 600 Ma) are exposed in large areas in central DML. This is followed by post-tectonic granitoid batholiths emplaced at ca. 512 Ma (Jacobs et al., 1998; Mikhalsky et al., 1995). In the Schirmacher Oasis area (Fig. 2.1), Henjes-Kunst (2004) reported granulite facies metamorphism dated by U/Pb analyses at ca. 625 Ma. These metamorphic ages predate the current metamorphic ages reported south of this area (Jacobs et al., 1998).

2.3.4 The Maud Belt

The Maud belt is characterised by the Mesoproterozoic basement rocks with strong (LN/EP) metamorphic overprinting. The belt stretches along the northern part of central Dronning Maud Land, then south-west along the western margin of the Grunehogna Craton, and continues southwest into Heimefrontfjella. As addressed, the 20 km wide dextral shear zone in Heimefrontfjella (HSZ) is interpreted to separate fundamentally different domains in this region (Jacobs et al., 1997; Jacobs et al., 1998). The south-eastern side of the Heimefront shear zone is characterised by Maud Belt ages (1130–1040 Ma) with following polyphase high-grade "Pan-african" metamorphic overprinting (Jacobs et al., 1996; Jacobs et al., 1998), whilst the north-western side of the boundary is characterised by older Grenville-age crust that is unaffected by "Pan-african" overprinting (Mendonidis et al., 2015; Ruppel et al., 2015). This boundary is interpreted to represent the western front of the East African-Antarctic Orogen, and the boundary that separates the Grunehogna Craton and the Natal sector from the Maud Belt, i.e the western boundary of the Maud Belt (Jacobs and Thomas, 2002; Shackleton, 1996). This is also supported by aeromagnetic mapping in combination with field observations (Golynsky and Jacobs, 2001). The eastern boundary of the Maud Belt is still a matter of ongoing debate, and is not yet fully constrained (Jacobs et al., 2015). As previously

addressed, the Forster Magnetic Anomaly (FMA) (Fig. 2.10) (Riedel et al., 2013) is interpreted as the main boundary between the Maud Belt and the TOAST (Jacobs et al., 2015). This boundary however, has not yet been discovered within the nunataks in northern central Dronning Maud Land. Thus, discovering this boundary would give new insights into the nature of the eastern boundary of the Maud Belt.

2.4 Geological Evolution of Central Dronning Maud Land

Following the basement formation during the Mesoproterozoic event related to the supercontinent Rodinia, the period between ca. 1050 and 650 Ma shows limited evidence of any tectonic activity, except for a granitoid intrusion dated to ca. 760 Ma within the Schirmacher Oasis area (Jacobs, Unpublished). However, during the Late Neoproterozoic-Early Palaeozoic, a significant "Pan-African" overprint and deformation occurred in DML. This tectonic collision history can be divided into three main phases (Jacobs et al., 2008a):

Phase 1: At ca. 625 Ma the earliest recorded granulite facies metamorphism in DML was reached within the Schirmaker Oasis area (Henjes-Kunst, 2004) (Fig. 2.1). This was followed by charnockite and anorthosite intrusions at ca. 600 Ma with penetrative deformation from some anorthosites at ca. 585 Ma (Jacobs et al., 1998). During this event, many of the zircons that crystallised during the Mesoproterozoic have been overgrown by metamorphic zircon rims. This tectonic event is associated with shallowly inclined structures that probably were a result of nappe emplacements, however the age of these structures is unknown (Jacobs et al., 2008a).

Phase 2: The main metamorphic event and deformation in DML occurred during this phase, reaching medium to high-grade metamorphism. This phase is bracketed with metamorphic zircon rims between ca. 590 and 550 Ma (Jacobs et al., 1998; Jacobs et al., 2003*b*). The event is interpreted to represent the collision phase forming tight and isoclinal upright folds trending E-W and ESE-WNW. Other important features associated within the collision phase; a major sinistral shear zone along the southern margin of the mountain rage in Orvinfjella, as well as transpressive structures in Wohlthatmassiv (Bauer et al., 2004). These structures correlate well with the overall sinistral transpressional setting in the Mozambique belt of Africa (Jacobs et al., 1998). The timing of the main collisional phase has been based on the formation of discrete extensional shear zones as well as undeformed pegmatite intrusions and granite veins, which constrain a Cambrian age for the collision event (Jacobs et al., 2003*b*).

Phase 3: This phase is recognised by a late-tectonic stage during which extension and tectonic exhumation occurred along with magmatism and southward crustal extrusion between ca. 530 and 485 Ma, exposing mid to lower crustal levels (Engvik and Elvevold, 2004; Jacobs et al., 2003*a;* Jacobs and Thomas, 2004). The event also resulted in syn-tectonic shearing as well as late- to post-tectonic intrusions and isothermal decompression (Colombo and Talarico, 2004; Jacobs et al., 2003*a*). The igneous melts that formed in the late-tectonic stage consisted of voluminous granitoids, which is part charnockitic. This extensive magmatic suite is covering an area of at least 15,000km^2 (Roland, 2004*b;* Roland, 2004*a*). Based on Eby (1992), this granitoid suite was classified as an A_2-type granite, which is related to post-collisional magmatism during orogenic collapse, and could possibly be accompanied by delamination of the orogenic root (Jacobs et al., 2008a). These granitoid bodies can also be correlated further north to the Lurio belt in north-eastern Mozambique, but do however, not extend further north (Jacobs et al., 2008a). To form the large volumes of granites and charnockites that are present in DML, the proposed tectonic model is the delamination model presented by Jacobs et al. (2008a) (Fig. 2.11).

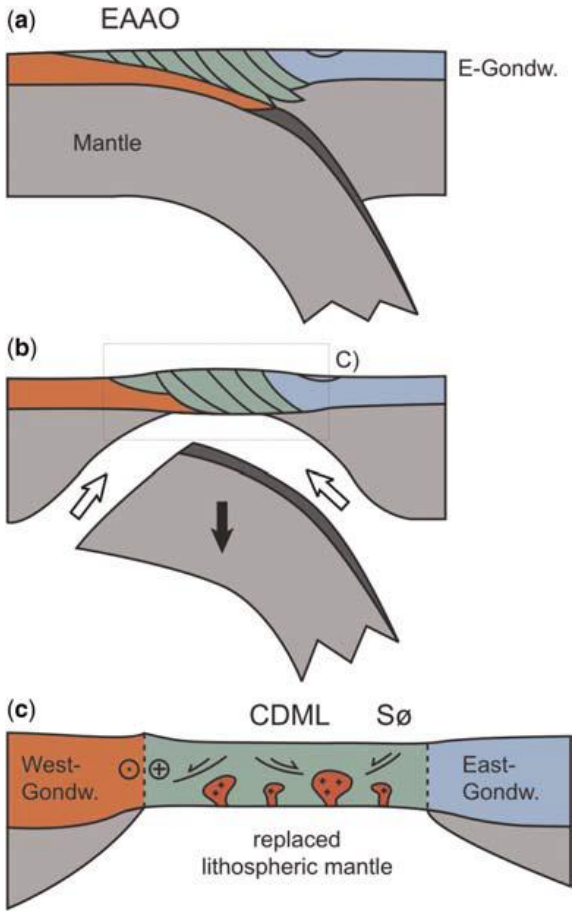

Fig. 2.11: The possible delamination model after Jacobs et al. (2008a). This model points to a likely reason for the formation of large voluminous granitoids where delamination is causing uplift and decompression.

Fig. 2.12 summarises the different tectonic/geological domains of East Antarctica based on the evolution of the continent. The East Antatctic continent has been rotated into its Gondwana possition. This figure summarises the previously adressed areas of East Antarctica and Dronning Maud Land. The northward extention of the Maud Belt can be into East Africa as part of the Mozambique belt (Bisnath et al., 2006).

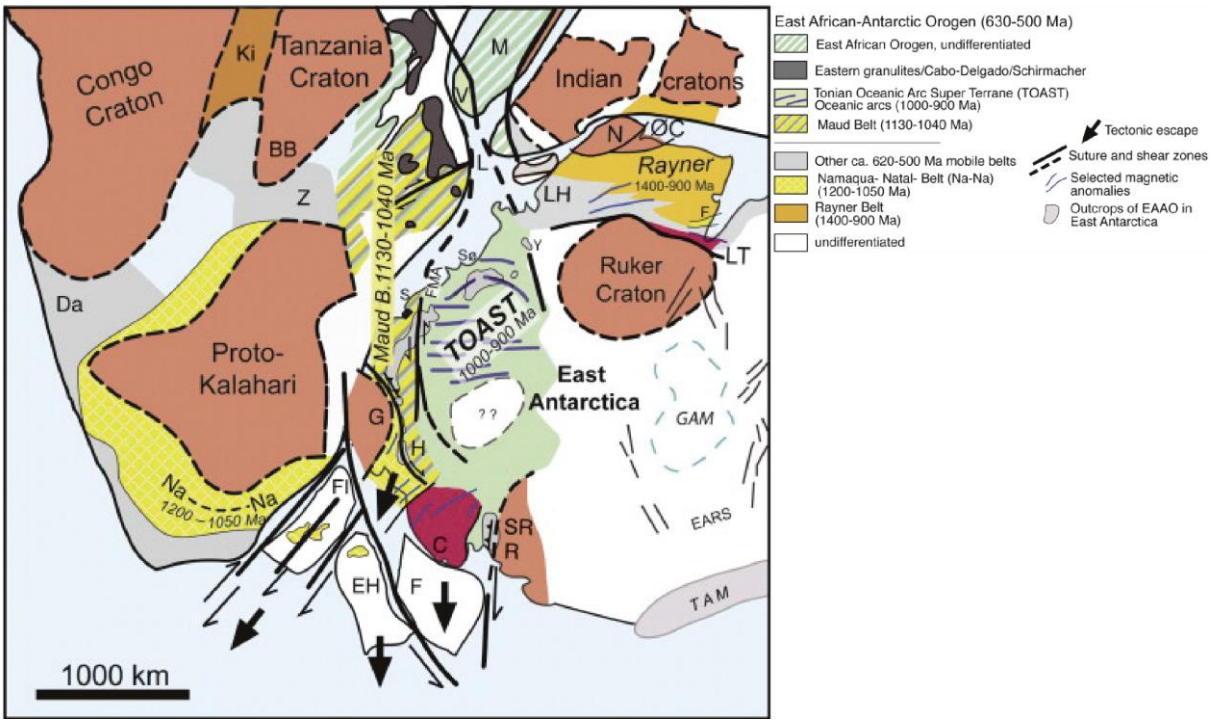

Fig. 2.11: Geodynamic map of East Antarcica in a Gondwana reconstruction. Abbreviations: C - Coats Land; DML - Dronning Maud Land; Da - Damara belt; EH - Ellsworth-Haag; F - Filchner block; FI - Falkland Islands; G - Grunehogna; H - Heimefrontfjella; L - Lurio Belt; LA - Lambert Terrane; N - Napier Complex; Na–Na - Namaqua–Natal; ØC - Øygarden Complex; S - Schirmacher Oasis; Sø - Sør Rondane, SR - Shackleton Range; TAM - Transantarctic Mts., LH - Lützow–Holm Bay; M - Madagascar; R - Read Block; V - Vohibori; Y - Yamato Mts.; Z - Zambesi belt. Figure modified from Jacobs et al. (2015).

3. Principles of U-Pb Zircon Geochronology

3.1 The mineralogy of zircon

Zircon ($ZrSiO_4$) is a tetragonal orthosilicate. Isolated SiO_4 tetrahedra are connected along the edges and corners with intervening ZrO_8 octahedra (Harley and Kelly, 2007). The alternating SiO_4 tetrahedra and ZrO_8 octahedra form chains along the c-axis, separated by a void between the chains. In naturally occurring zircons, this void is usually filled with impurities, and contain Rare Earth Elements (REE) as well as P, Sc, Nb, Hf, Ti, U and Th (Hoskin and Schaltegger, 2003). The overall simple structure of the zircon mineral with chains of SiO_4 and ZrO_8, separated with by void results in a moderately high density of the mineral (4.66 g/cm^3). This mineral structure greatly contributes to the minerals low absolute thermal expansion and compressibility (Harley and Kelly, 2007). From room temperature to its stability limit at 1690°C, only 0.6% volume expansion occurs. These mineral characteristics are what makes zircon extremely physically resistant, and stable under high temperatures and pressures (Harley and Kelly, 2007). Zircon minerals crystallise at temperatures between 700–830°C. Grains with a very high U content, often receive damage to the crystal lattice due to radioactive decay, causing metamictisation. Zircons with oscillatory zoned cores and Th/U ratios around 1 are typical for igneous zircons (e.g. Corfu et al., 2003). Metamorphic zircons are often rounded with dark, unzoned or sector zoned grains with a Th/U ratio of <0.1 (e.g. Möller et al., 2003).

3.2 The U-Pb isotopic system

The U/Pb system has become the most popular isotopic system for geochronologists. The main reason why this system is beneficial, is the power of having two separate uranium isotopes (^{235}U and ^{238}U) decaying simultaneously to two different Pb isotopes (^{207}Pb and ^{206}Pb, respectively) (Williams, 1998). This means that two individual isotopic systems (clocks), with identical chemical properties and diffusion rates simultaneously decay within the same system (Cherniak and Watson, 2003). The half-life of the two different systems does however vary: $^{238}U \rightarrow {}^{206}Pb$ ($T_{1/2} = 4.5$ Ga), $^{235}U \rightarrow {}^{207}Pb$ ($T_{1/2} = 0.7$ Ga). One can calculate the individual radiometric ages for the two isotopic systems by the known present ratio of $\frac{^{238}U}{^{235}U} = 137.82$ (Condon et al., 2010). Furthermore, the ^{207}Pb/^{206}Pb age can be calculated:

$$^{207}Pb = {}^{235}U(e^{\lambda 235t} - 1) \quad (1)$$

$$^{206}Pb = {}^{238}U(e^{\lambda 238t} - 1) \quad (2)$$

$$\frac{^{207}Pb}{^{206}Pb} = \frac{(e^{\lambda 235t} - 1)}{137.82(e^{\lambda 238t} - 1)} \quad (3)$$

The Concordia diagram

The Concordia diagram uses the strength of the U/Pb isotopic system by combining the two different decay series. The daughter/parent ratios of U/Pb for ^{235}U and ^{238}U are plotted on the X and Y-axis (Williams, 1998). This diagram was first devised by Ahrens (1955), and later refined by Wetherill (1956). Based on the two systems, a reference curve is plotted to show the difference in ratios between $^{238}U/^{206}Pb$ and $^{235}U/^{207}Pb$ over time (Concordia line). Several analyses from one sample can be plotted in the diagram to calculate a common Concordia age for the sample. If the system is closed, the analyses will plot along the Concordia line. This means that the $^{238}U/^{206}Pb$, $^{235}U/^{207}Pb$ and $^{207}Pb/^{206}Pb$ ages are the same, and that the system has remained closed and gives "concordant" ages (Williams, 1998). If, however, the system has not remained entirely closed, the calculated ages will plot outside of the Concordia line and are therefore "discordant". Discordant analyses occur when the ratios of the two different systems contrast from the expected ratio in a closed system. If the system experiences Pb-loss, the analyses will form a line outside of the Concordia with two intercepts on the Concordia line. This line is called the Discordia line. The upper intercept between the Concordia line and the Discordia line (the oldest intercept) can be interpreted to represent the crystallisation age of the zircons, whilst the lower intercept (the youngest intercept) can be interpreted to represent a later tectono-thermal overprinting.

Tera-Wasserburg Concordia diagram

The Tera-Wasserburg Concordia diagram was proposed by Tera and Wasserburg (1972). This alternative diagram plot the $^{238}U/^{206}Pb$ ratio on the X-axis and the $^{207}Pb/^{206}Pb$ on the Y-axis. There are several benefits to using this plot (Williams, 1998). Firstly, the analyses plot directly as they are measured. The $^{235}U/^{207}Pb$ ratio is calculated as a derivative based on the isotopic composition of U. Secondly, the error in measuring the $^{238}U/^{206}Pb$ and $^{207}Pb/^{206}Pb$ is much less correlated, as these are measured values, compared to $^{235}U/^{207}Pb$ and $^{238}U/^{206}Pb$. Thirdly, the plotted analyses without correction for initial Pb, will form a mixing line that intersects with the $^{207}Pb/^{206}Pb$ (Y-axis) at the initial Pb composition. The Tera-Wasserburg plot gives visual advantages over the normal Concordia. This is especially the case when interpreting polyphase metamorphic samples, where both ancient and recent Pb-loss is more distinguishable in a Tera-Wasserburg Concordia diagram.

3.3 Sensitive High Resolution Ion Microprobe (SHRIMP) geochronology

The Sensitive High Resolution Ion Microprobe (SHRIMP), or secondary high mass resolution ion microprobe, is designed to analyse complex minerals on very high resolutions. SHRIMP is most commonly used to analyse U-Th-Pb ratios in minerals. The benefit of using this instrument for geochronology is that complex grains with a history of metamorphism can be measured accurately (Williams, 1998). An example of this is a zircon grain with an igneous core, and a metamorphic rim. Using the SHRIMP instrument makes it possible to analyse both the core and the rim of the same zircon grain.

A beam of primary ions $(O_2)^{1-}$ is shot onto the mineral surface at a 45° angle to the direction of the surface (Fig. 3.1). The beam creates a small impact crater on the surface with a diameter between ca. 5–30 µm, and a depth of ca. 1 µm. The impact of the primary beam releases secondary ions from the sample (Stern, 1997). The secondary ions released from the mineral surface are accelerated though the instrument, into the electrostatic analyser (Fig. 3.1). The electrostatic analyser filters the secondary ions based on the kinetic energy (Stern, 1997). The filtered secondary ions are accelerated into the magnetic sector, in which the ions are filtered based on the mass/charge ratio of the ions (Fig.3.1). When the secondary ions pass through the magnetic sector, the ions continue to the detectors, where the ions pass through a collector slit (Fig.3.1).

When preforming U-Th-Pb geochronology, the U, Th and Pb from the secondary ions are measured, along with reference peaks for Zr_2O^+, ThO^+ and UO^+.

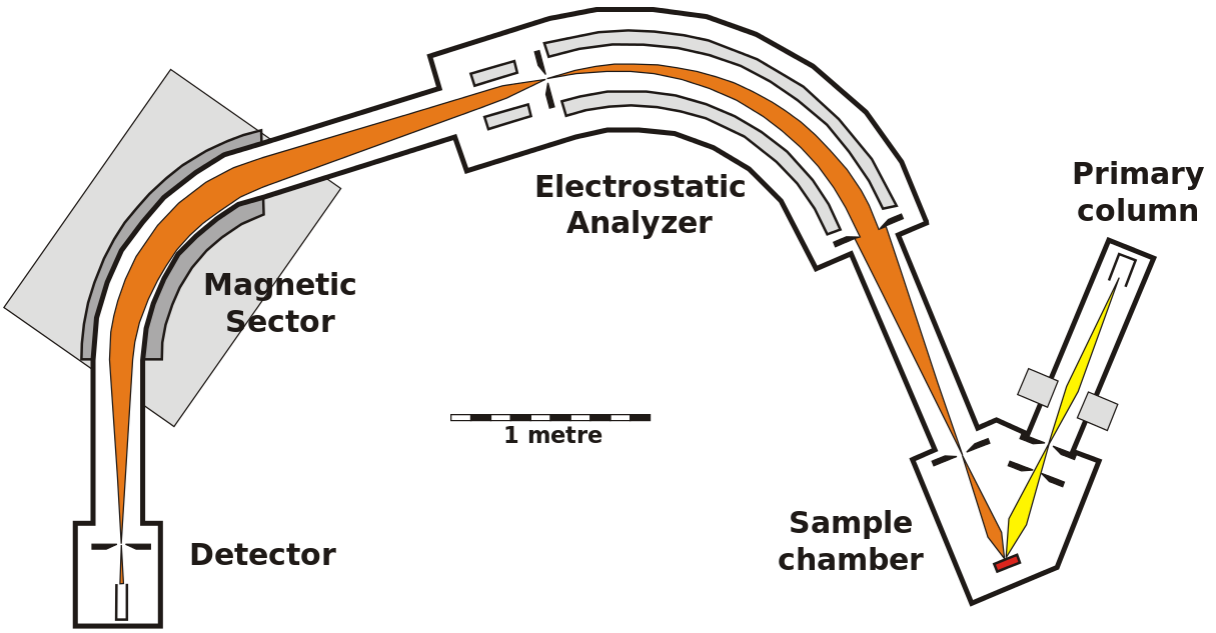

Fig. 3.1: Schematic diagram of the SHRIMP, showing the path of the primary beam onto the sample surface, and the path of the secondary ions through the instrument. Figure modified from Williams (1998).

4. Samples and Methods

4.1 Samples

Nine samples were selected for U/Pb SRHIMP analysis at the SHRIMP Ion Microprobe Laboratory of The University of Granada. The samples selected for this project, were collected during the GeoMaud 1995/96 expedition to East Antarctica. Sample locations are shown in Fig. 4.1. Prior to mineral separation the nine samples were cut for thin sections. The thin sections were prepared at The University of Bergen for detailed petrographic descriptions.

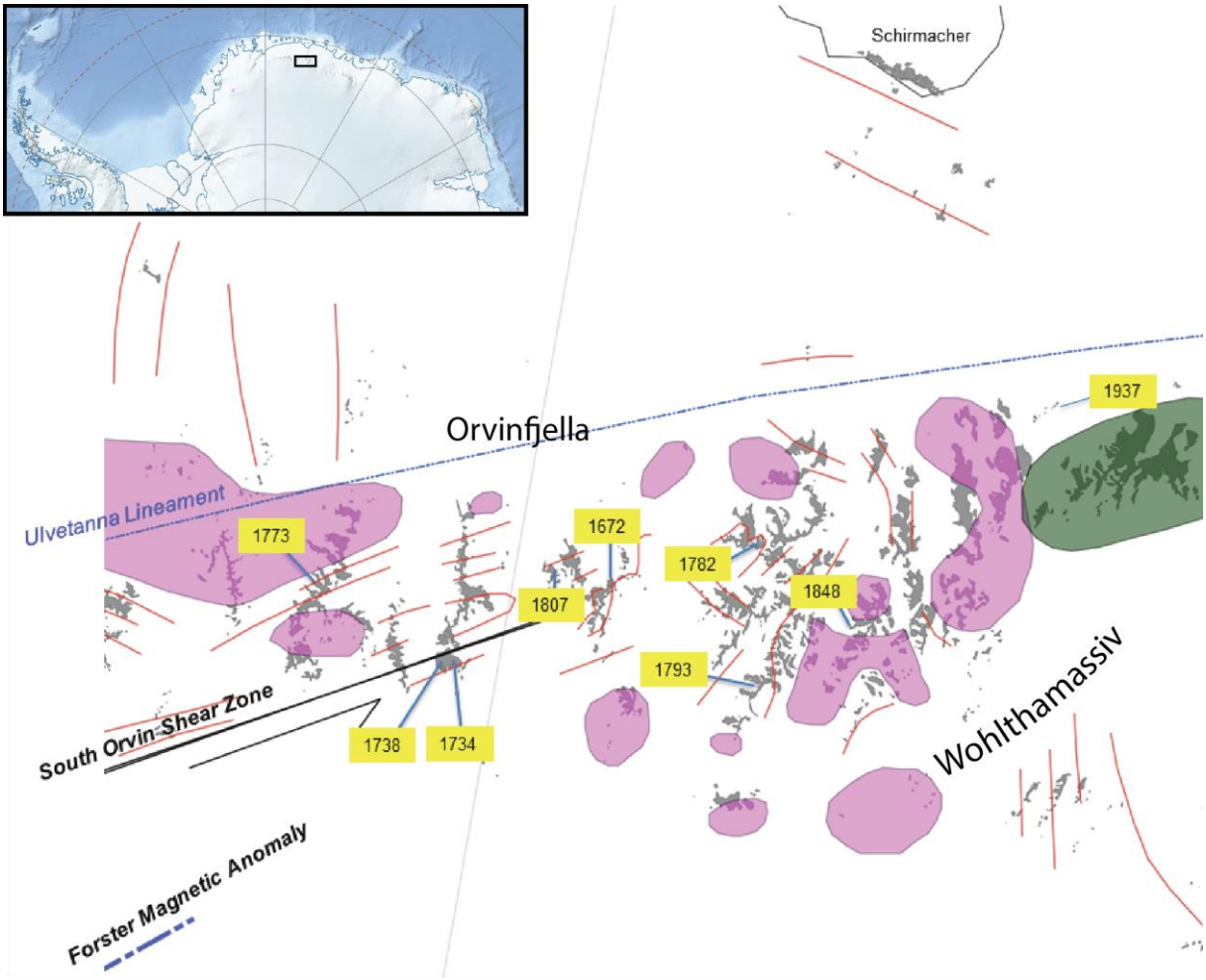

Fig. 4.1: Map showing the locations for the samples analysed in this study (sample numbers are marked in yellow). The blue lines indicate the location of the samples. The dashed blue lines represent magnetic anomalies. The black line represents the South Orvin Shear Zone. The green area represents anorthosite and the pink areas represent granitoid intrusions.

4.2 Methods

4.2.1 Sample preparation

Crushing and separation

Nine samples were chosen for geochronological analyses. The first stage of separation was crushing of the samples. Crushing and mineral separation of the samples were done at the University of Bergen using first a sledgehammer to crush the sample to pebbles with a size ca. 2–3 cm. The second stage of crushing was done with a Fritsch Pulverisette 13 discmill (Fig. 4.2A). By using the discmill the samples were crushed to size finer than 315 µm. Any larger particles were separated using a sieve. The samples with a grain size smaller than 315 µm were further separated on a Holman-Wilfley shaking table (Fig. 4.2B). During this separation, the heaviest fractions were separated from the lighter fractions to further reduce the sample size. The separated heavy fraction was dried and later used for magnetic separation. The magnetic separation was preformed using first a hand magnet to get rid of ferromagnetic minerals. For further magnetic separation of the minerals, Frantz Magnetic Separator was used in two stages (Fig. 4.2C). The magnetic separator was set to a tilt of 15° both forwards and sideways. On the first run the voltage was set to 0.6V to remove weak ferromagnetic minerals such as hematite. On the second run the voltage was increased to 1.2V. After all the samples were finished with magnetic separation, the next part of mineral separation was two stages of heavy liquid separation using LST (Low toxicity Sodium Heteropolytungstates) that has a density of: $2.83 g/cm^3$, and DIM (Di-Iodomethane) with a density of: $3.31 g/cm^3$. If the samples had a small enough volume, LST separation was not needed. Therefore, only DIM separation was used for smaller samples, without doing LST separation first. This was the case for one sample which went straight through DIM separation. In the LST separation (Fig. 4.2D), the heavier particles such as zircon and apatite sink through the solution, separating minerals such as quartz and feldspar from the sample. Following the LST separation, the samples were subsequently cleaned with deionised water and dried. The DIM separation represented the final stage of mineral separation. All the samples went through DIM (Fig. 4.2E) where zircons (4.60–4.70 g/cm^3) were separated from other heavier minerals, leaving a very concentrated amount of zircon grains in the sample. The sample was then cleaned with acetone and dried for picking.

Fig. 4.2: Overview of the steps during the mineral separation. A: Fritsch Pulverisette 13 discmill. B: Holman-Wilfley shaking table. C: Frantz Magnetic Separator. D: LST (Low toxicity Sodium Heteropolytungstates). E: DIM (Di-Iodomethane)

Sample picking and analysis preparation

All zircons were handpicked under a Zeiss microscope from the mineral separates (Fig. 4.3A). For all the samples, except for two, 300 zircons were picked. Two of the samples (J1672 and J1837) did not contain enough zircons, and therefore, 150 and 170 zircons were picked respectively. The 300 grains were picked onto a glass plate and later put into a plastic container (Fig. 4.3B). The picked samples were then sent to the SHRIMP Ion Microprobe Laboratory of The University of Granada for mounting, preparation, imaging and analysis (Fig. 4.4).

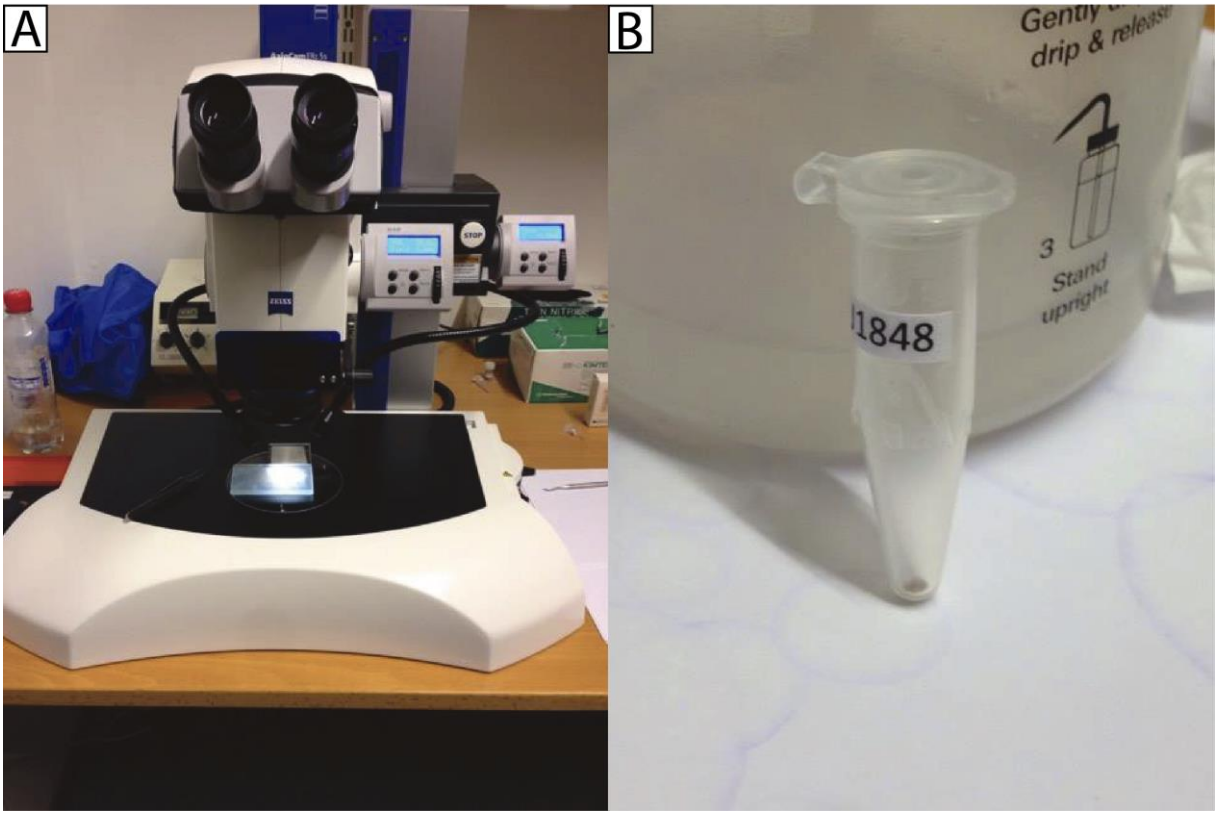

Fig. 4.3: The picking process. A: Zeiss picking microscope with the glasses containing the samples and the tweezers for picking. B: Plastic containers storing the ca. 300 picked zircon grains. The caps were taped, and the samples were shipped to The University of Granada in these containers.

The imaging of the mount was done in four steps: (1) Transmitted light optical imaging, (2) Reflected light optical imaging, (3) SEM Cathodoluminescence imaging, and finally (4) Low magnification SE-SEM imaging for navigation on the mount. The transmitted light and reflected light images were used to identify inclusions and fractures in the grains. The cathodoluminescence images were used to identify internal structures and zoning. The completed mounts and images were sent back to the University of Bergen for selection of spots for analysis. Each sample contained around 100 zircons. Of these, around 20–30 spots were chosen for analyses.

Fig. 4.4: SHRIMP Ion Microprobe Laboratory at The University of Granada.

4.2.2 SHRIMP Analysis

All the samples were handpicked and cast in epoxy discs with a diameter of 3.5 cm. The unknowns were mounted together with several grains of TEMORA-1 standard (for isotope ratios; Black et al. (2003)), one grain of SL13 standard (for U concentrations; Claoué-Long et al. (1995)) and a few grains from the REG zircon (rich in common Pb for calibrating masses). The mount was polished and imaged. Before analysis, the mount was extensively cleaned and coated with ultra-pure gold (8–10 nanometres thick). The analytical method followed Williams and Claesson (1987). Each of the spots selected for analysis was rastered with the primary beam at 120 seconds prior to the analysis. Then, 6 scans followed the isotope peak sequence ^{196}Zr2O, ^{204}Pb, $^{204.1}$background, ^{206}Pb, ^{207}Pb, ^{208}Pb, ^{238}U, ^{248}ThO, ^{254}UO. Every peak of every scan is measured sequentially ten times with the following total counting times per scan: 2 seconds for mass 196; 5 seconds for masses 238, 248, and 254; 15 seconds for masses 204, 206, and 208; and 20 seconds for mass 207. The primary beam, composed of $^{16}O^{16}O^{+}$, is set to an intensity of about 5 nA, with a 120 µm Kohler aperture, which generates 17 x 20 µm elliptical spots on the target. The secondary beam exit slit is fixed at 80 µm, achieving a resolution of about 5000 at 1% peak height. For calibration during analysis, these following three steps were followed: (1) Mass calibration using REG zircon with high U, Th and common Pb (ca. 2.5 Ga). (2) Calibration using SL13 zircon with U-concentrations (238 ppm U). (3) Calibration with TEMORA-1 standards for isotope ratios (416.8 ± 1.1 Ma). Data reduction was completed with the SHRIMPTOOLS software that was specifically made for IBERSIMS. The software is used to calculate the intensity of each measured isotope in two steps. The first step is to use a STATA letter-value algorithm to identify outliers. The second step is to calculate 204/206, 207/206, 208/206, 254/238 ratios based on Dodson (1978) double linear interpolation method. Based on Williams (1998) the ^{206}Pb/^{238}U is calculated from the measured $^{206}Pb^{+}/^{238}U^{+}$ and UO^{+}/U^{+}. All errors in the analyses are given at the

95% confidence level. For the high-U zircons (U > 2500 ppm), a further correction was needed based on the algorithm of Williams and Hergt (2000). The reported single-grain ages of this study are $^{206}Pb/^{238}U$ ages.

4.2.3 Data Processing

Some of the raw data from the zircon analyses had to be corrected for common Pb to obtain correct results. All analysed grains were calculated without common Pb correction, as well as 207-corrected, 204-corrected and 208-corrected ratios. Based on the percentage of common Pb estimated from ^{204}Pb counts (f_{206_4}), the analyses with a high relative percentage of common Pb (compared with the other analyses in the sample) were corrected. The common Pb uncorrected ratios were used as the baseline ratios. The analyses with high relative common Pb percentage were changed to 204-corrected or 208-corrected ratios. The modified ratios for each sample were wither entirely 204-corrected or 208-corrected. Usually, the corrected ratios were used 1-4 analysed spots in each sample. For 4 of the samples 208-corrected ratios were applied entirely i.e. no common Pb or 204-corrected ratios were used. The 208-corrected ratios were applied in cases when neither uncorrected or 204-corrected ratios gave sufficient results.

Some of the analysed samples had large calculated age errors. The samples with more than 5% calculated age error at 2σ were discarded from further consideration, and are not presented in the Concordia plots. These analyses will be available in the appendix (greyed out).

Data interpretation

All Concordia ages in this study were calculated in Isoplot version 3.75, an extensional application for Excel 2003 (Ludwig, 2012). Whenever possible, Concordia ages and weighted mean ages were calculated for entire samples or specific age groups within samples. In most cases, a Discordia line was calculated with a lower and upper intercept. For this study, all the figures concerning geochronology were made using Isoplot. The presented ages of this study are ages with a 2σ error.

5. Results

5.1 Petrography

J1672 Tonalitic gneiss

J1672 has a greyish to white colour with thin, dark bands of around 1 mm (Fig. 5.1). The main minerals in the sample are quartz, plagioclase, microcline, amphibole (hornblende) and biotite. The hornblende and biotite are mainly present within the darker bands (Fig. 5.2 A and B) of the sample. The brighter parts of the sample contain mostly quartz, plagioclase and microcline, generally with a random distribution (Fig. 5.2 A and B). The quartz grains have varying sizes, where some of the grains are large and elongated with undulose extinction (Fig. 5.2 D). Around the larger grains are smaller re-crystallised grains of quartz. Typical accessory minerals within the sample are garnet, allanite and zircon. The zircons have typically crystallised within quartz grains or along grain boundaries of quartz and plagioclase (Fig. 5.2 C and D).

Typical metamorphic reactions within the sample are small re-crystallised grains of quartz with bulging edges, resulting from Grain Boundary Migration (GBM).

The sample shows foliation fabric with the biotite and hornblende defining the dark foliation bands of ca. 1 mm, and represents an S-tectonite.

Fig. 5.1: Sample J1672. Length of sample: 7 cm.

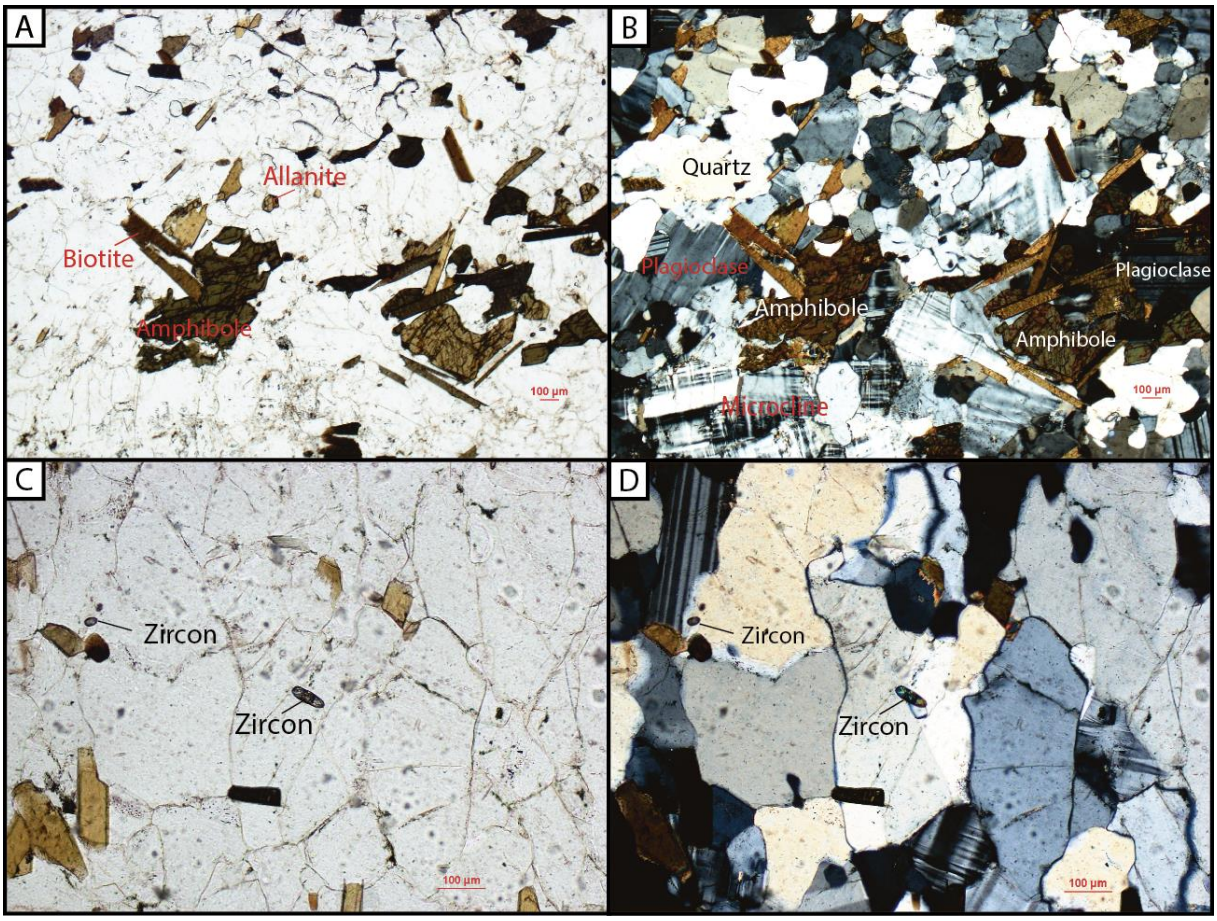

Fig. 5.2: Photomicrographs of sample J1672. A: General image in plane polarised light (PPL) showing amphibole (hornblende) and biotite. Other visible minerals are allanite (orthite). The bright part consists of quartz, feldspar (microcline) and plagioclase. B: The same image in cross polarised light (XPL) showing the finer grained quartz, plagioclase and microcline. C: PPL image of zircons in the sample. The high-relief grains are zircons. D: Same image in XPL showing that zircons occur typically within quartz grains or along edges of quartz and plagioclase grains.

J1734 Quartzofeldspathic garnet gneiss

J1734 is composed of alternating pink to white and grey to black segments or lenses (Fig. 5.3). Round, brown to orange spots without preferred orientation, are scattered throughout the sample. The lenses within the sample appear mineralogically different. The main mineral composition in the sample consists of quartz, microcline, plagioclase and biotite (Fig. 5.3A and B). Also, abundant garnet is present. The dark sequences in the sample are richer in biotite, and garnet. The bright sequences in the sample consist mostly of quartz, plagioclase and large grains of microcline. Typical accessory minerals in thin section are zircons. The zircons have often crystallised within triple-junctions or along edges of quartz grains (Fig. 5.3D). The microcline grains are often large with re-crystallised edges, indicating dynamic re-crystallisation at temperatures of > 450°C (Fig. 5.4C). The orange/brownish spots in the sample consist of garnets. Typical metamorphic reactions in the sample include quartz and microcline grains that have dynamically re-

crystallised, and the grains often show undulose extinction. Bulging grain boundaries of the larger quartz grains are visible, indicating dynamic re-crystallisation (GBM). The sample has a lineation fabric, indicating that this is an L-tectonite, where the amphibole and biotite define the lineation.

Fig. 5.3: Sample J1734. Pen for scale.

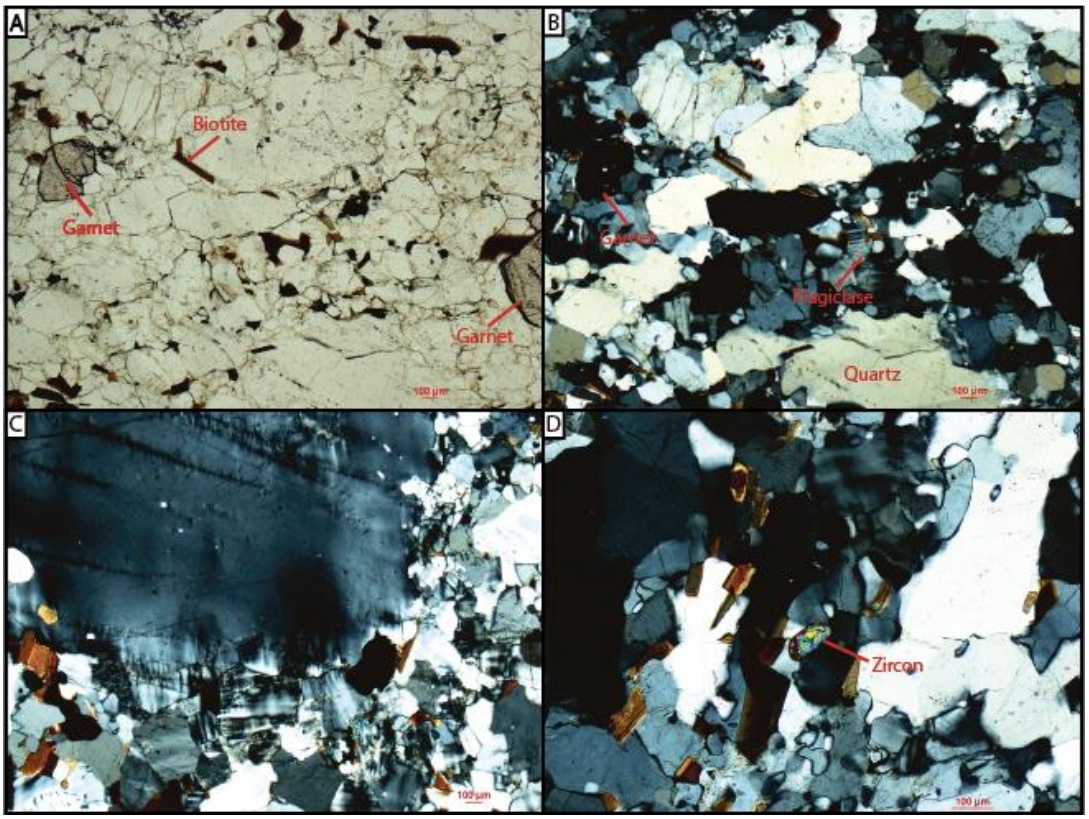

Fig. 5.4: Photomicrographs of sample J1734. A: PPL of the general composition with garnets and biotite. The brighter parts are quartz, feldspar and plagioclase. B: Same image in XPL showing fine grained re-crystallised quartz, as well as some lager quartz grains with undulose extinction. Other present minerals are plagioclase. C: Re-crystallised microcline from the larger grain, indicative of temperatures >450°C. D: Image of zircon contact relationship. The zircons typically crystalise in triple junctions or along grain boundaries.

J1738 Metarhyolite

The sample has mainly an orange colour with small patchy dark elongated minerals that are < 1 mm thick (Fig. 5.5). Also present is a ca. 8 mm darker band, representing an area with darker minerals, and slightly different composition. The sample also has small spots with orange to brown colour. The main minerals within the sample are quartz, K-feldspar (microcline) and some biotite (Fig. 5.6A), along with abundant garnet (Fig. 5.6C and D). This is represented by the small orange to brown patchy minerals visible on the sample. Typical accessory minerals in the sample are zircons. The darker band of ca. 8 mm contain more biotite, giving it the darker appearance. The elongated darker minerals in the sample are ribbon quartz, which often shows undulose extinction (Fig. 5.6A, C and D). These elongated, large grains of quartz often show fissures within the grains. Also, smaller re-crystallised quartz grains are present.

Typical metamorphic indicators are present in the sample with ribbon quartz with undulose extinction, smaller re-crystallised grains of quartz, and the presence of garnets. Another important feature in this sample is the deformation fissures within the larger grains of quartz, indicating deformation of the quartz at lower temperatures (Fig. 5.6B).

This sample represents an S-tectonite, where quartz and biotite define the darker foliation bands of the sample.

Fig. 5.5: Sample J1738. Length of the sample: 10.5 cm.

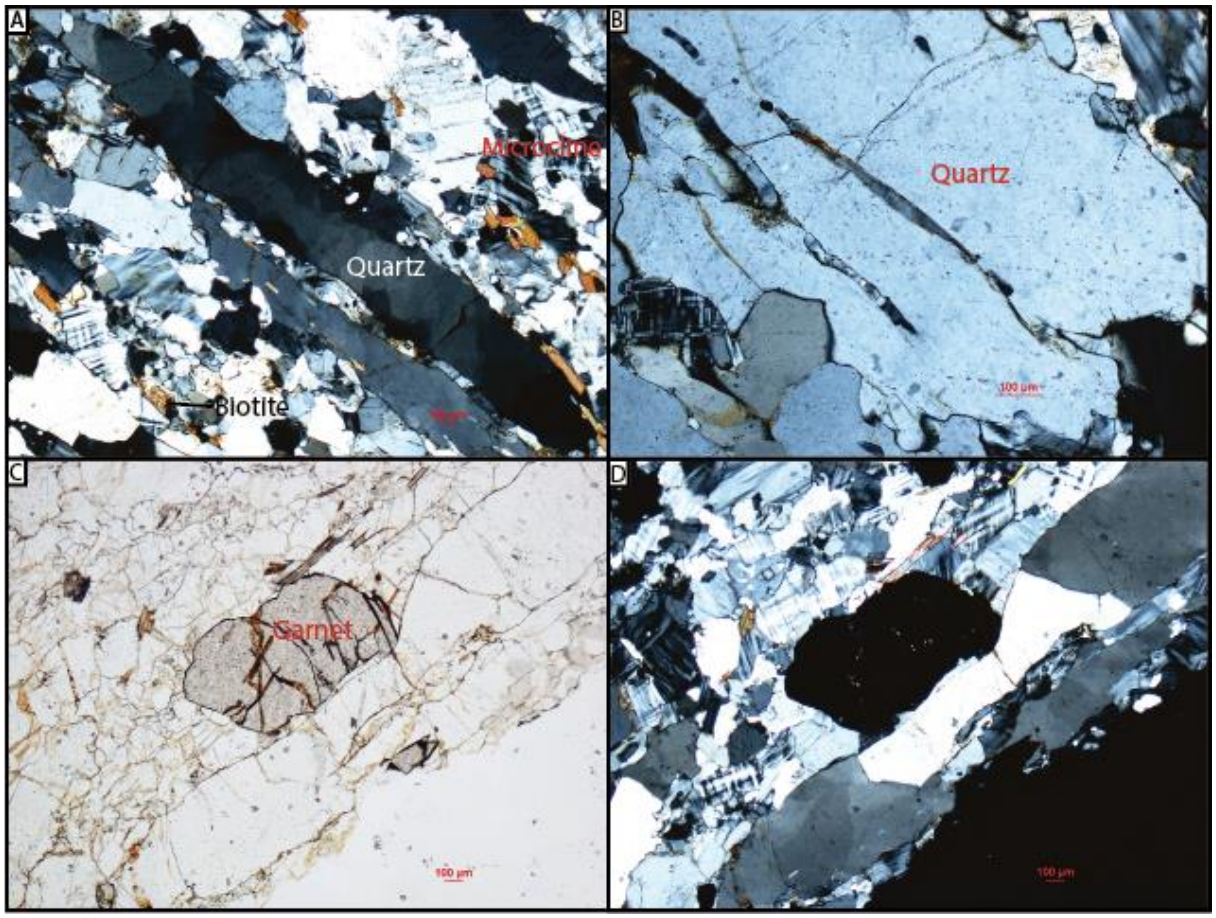

Fig. 5.6: Photomicrographs of sample J1738. A: General XPL image of the sample, with ribbon quartz showing undulose extinction, finer grained quartz, microcline and biotite. B: XPL image of deformation fissures in the quartz. C: PPL image of garnet grain. D: XPL image of garnet grain. The elongated quartz grain shows undulose extinction.

J1773 Garnet-bearing migmatite

The sample has a bright white colour with small grey and orange to brown spots (Fig. 5.7). The bright part of J1773 consists mainly of quartz and K-feldspar (microcline), making up the main mineral composition of the sample (Fig. 5.8A and B). The smaller grey grains are ribbon quartz. Larger grains of ribbon quartz are often characterised by undulose extinction. Smaller orange/brown spots visible around the sample represent grains of garnet (Fig. 5.8A). Typical accessory minerals present in thin section are orthopyroxene and zircon (Fig. 5.8A and B).

This sample shows typical signs of metamorphic alteration, with ribbon quartz showing undulose extinction, smaller re-crystallised grains of quartz, along with the presence of garnet and orthopyroxene. J1773 represents an L-tectonite, where the ribbon quartz defines the linear pattern in the sample.

Fig. 5.7: Sample J1773. Length of sample: ca. 6.5 cm.

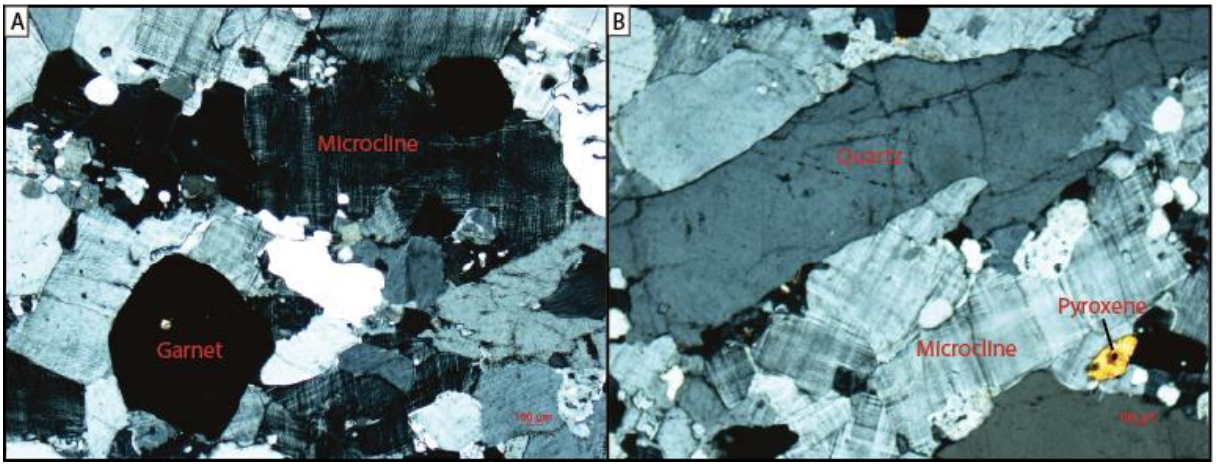

Fig. 5.8: Photomicrographs of J1773. A: Coarse grained microcline, quartz and garnet. Some fine-grained re-crystallised grains are present in the top left area of the image. B: Large ribbon quartz with microcline around. A small grain of orthopyroxene is visible in the bottom right corner.

J1782 Garnet gneiss

The sample looks very different from the previous samples with one completely bright part that abruptly changes to dark, black bands with a thickness of ca. 10 mm and 3 mm (Fig. 5.9). The bright part of the sample consists mainly of quartz. Some garnet is also present (Fig. 5.10C and D). The darker part of the sample primarily consists of biotite and garnets as well as some quartz and plagioclase (Fig. 5.9A and B). The main mineral composition of the sample is primarily quartz and plagioclase, with abundant biotite and garnet, mostly present in the darker bands (Fig. 5.10A, B, C and D). Typical accessory minerals in thin section are zircons, apatite and orthopyroxene (Fig. 5.10B, C and D).

Typical metamorphic alteration in this sample is mostly represented by re-crystallised quartz grains and the presence of garnets. This sample represents an S-tectonite, where the dark bands of garnet and biotite define the foliation.

Fig. 5.9: Sample J1782. Width of the sample: ca. 7 cm.

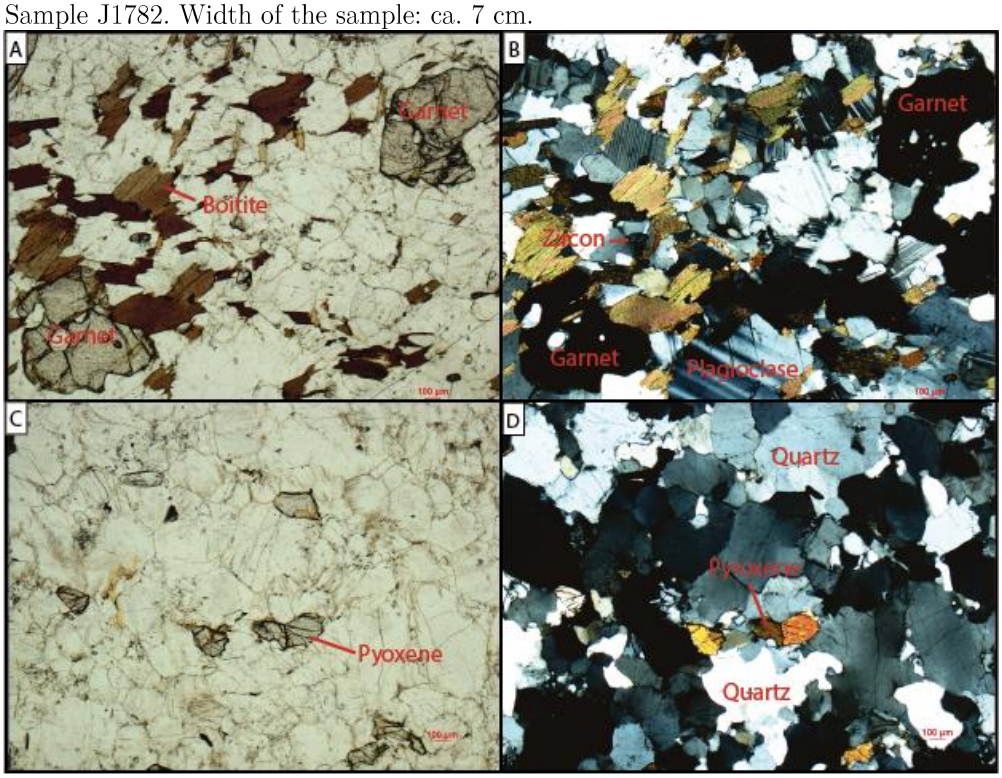

Fig. 5.10: Photomicrographs of J1782. A: PPL image of the darker part of the sample. This area is richer in biotite and garnet. B: XPL of the same area. Showing quartz and plagioclase around the biotite and garnet. The typical contact relationship of zircon around grain boundaries. C: PPL image of the brighter part of J1782, showing orthopyroxene. D: XPL of the same area, showing re-crystallised quartz, and in some cases undulose extinction.

J1793 Migmatitic Tonalite

The sample has a dark colour with bright, white lenses or bands that are ca. 2 mm thick, with a different composition (Fig. 5.11). The main minerals in this sample are quartz, plagioclase, amphibole and biotite (Fig. 5.12A and B). Typically, the bright lenses consist entirely of quartz. Other accessory minerals present in thin section are titanite and zircon.

Typical metamorphic reactions in the sample are re-crystallised quartz grains, often from elongated grains. The presence of patchy biotite crystallisation around the grain boundaries of quartz, plagioclase and amphibole, indicate that retrogradation has occurred. The sample has thin bands and lenses representing the foliation, where the bright quartz lenses define the foliation of the S-tectonite.

Fig. 5.11: Sample J1793. Length of sample: 5.5 cm.

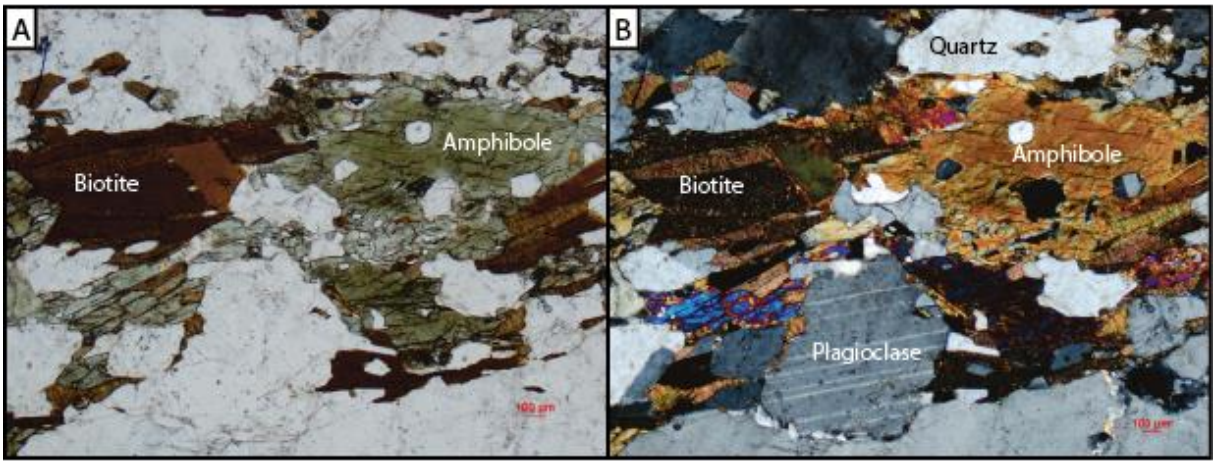

Fig. 5.12: Photomicrographs of sample J1793. A: PPL image showing the general composition of the sample with the green mineral representing amphibole (hornblende). The dark brown mineral is biotite. B: XPL image from the same area, showing large grains of quartz and plagioclase. Some quartz grains show undulose extinction.

J1807 Orthopyroxene-bearing enderbite

This sample has a grey colour with alternating white bands with a thickness of ca. 2–3 mm (Fig. 5.13). The brighter bands are not always continuous and often pinch out. The main minerals present in the sample are quartz, plagioclase and biotite, with some microcline (Fig. 5.14A and B). Other accessory minerals present in the sample are orthopyroxene, zircon and apatite (Fig. 5.14A and B).

Typical metamorphic reactions present in the sample are elongated quartz grains with undulose extinction and the presence of symplectitic biotite intergrowth with quartz, which indicates retrogradation (Fig. 5.14C and D). There are often many smaller re-crystallised quartz grains along the margins of the larger quartz grains, indicating dynamic re-crystallisation (Fig. 5.14B and D).

The sample shows a foliation where the bright quartz-rich bands define the foliation of the S-tectonite.

Fig. 5.13: Sample J1807. Length of the sample: 6 cm.

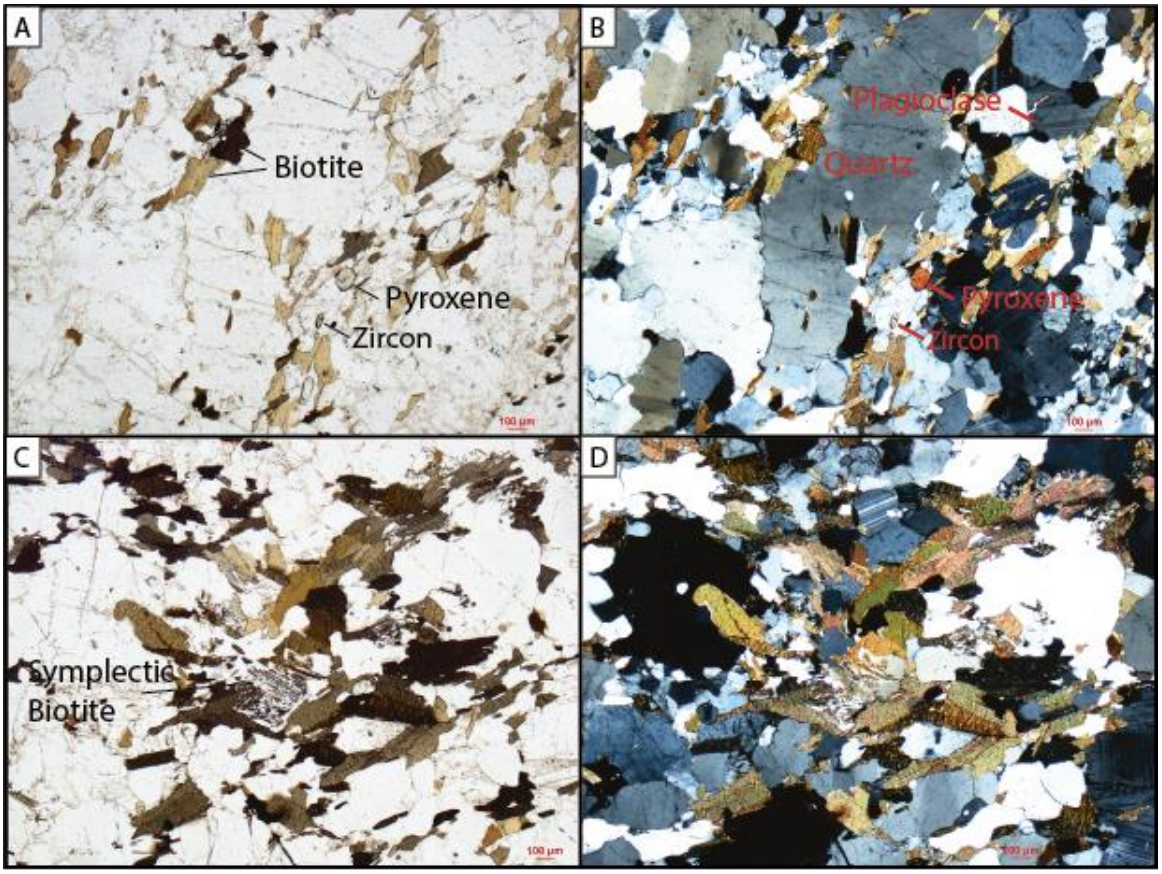

Fig. 5.14: Photomicrographs of sample J1807. A: PPL image of the general composition with biotite, orthopyroxene and zircons visible. B: XPL image of the same area showing large elongated quartz grains, as well as some smaller re-crystallised quartz grains. C: PPL image of symplectitic biotite growth within quartz grains. D: XPL image of the same symplectitic biotite.

J1848 Garnet gneiss, supracrustals

The sample has a dark colour with very thin, bright bands of ca. 1–2 mm (Fig. 5.15). The bright bands often form continuous bands that do however, sometimes bend around the darker parts. The lower part of the sample has a brighter colour with thin dark bands. This area also has orange to brown small grains. The main minerals in this sample are quartz and plagioclase, with abundant garnet, biotite and some microcline (Fig. 5.16A, B, C, D and E). Typical accessory minerals present in thin section are zircon and apatite (Fig. 5.16A, B, C, D and E). The zircons in this sample have typically crystallised between grains of quartz and plagioclase.

There are typical metamorphic reactions present in the sample such as patchy biotite overgrowth (Fig. 5.16A and C), sericitisation of plagioclase indicating hydrothermal influence during metamorphism, and re-crystallised quartz with bulging grain boundaries.

The sample shows a foliation that is defined by the bright quartz-rich bands, and represents an S-tectonite.

Fig. 5.15: Sample J1848. Length of the sample: 11.5 cm.

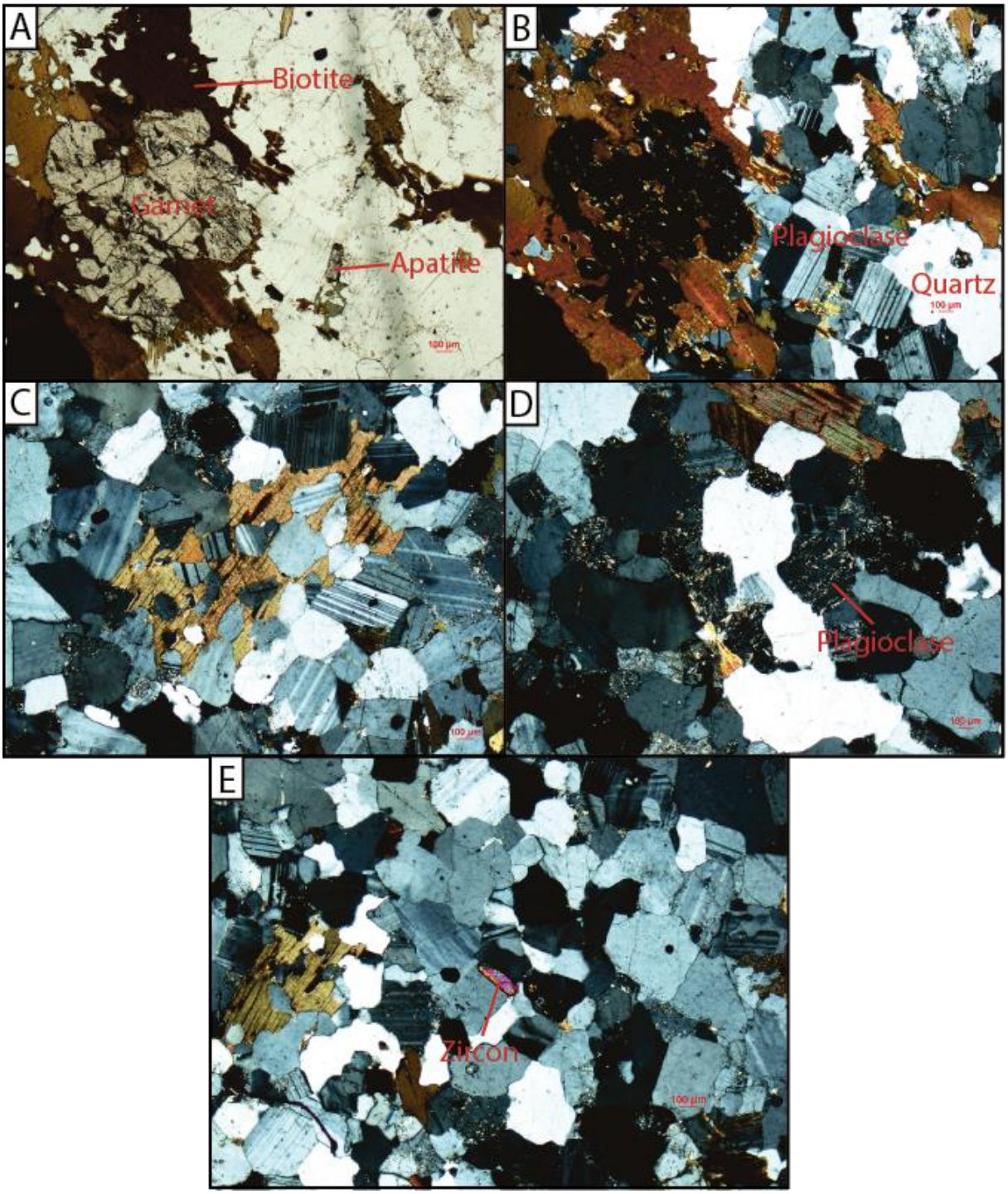

Fig. 5.16: Photomicrographs of sample J1848. A: A general PPL image of the sample showing garnet, biotite and apatite. B: XPL image of the same area displaying plagioclase and quartz. C: Patchy biotite crystallised between quartz and plagioclase grains (XPL). D: XPL image of sericitised plagioclase, which is common in this sample. E: XPL image of a typical zircon grain, showing the contact relationship between zircons and quartz and plagioclase.

J1937 Mafic granulite

This sample is generally dark in colour, with brighter grey bands of up to 2 cm. The darker part of the sample contains large grains of completely black minerals (Fig. 5.17). The main minerals present in this sample are amphibole (hornblende), pyroxene (both orthopyroxene and clinopyroxene), plagioclase, quartz and biotite (Fig 5.18). The darker bands are dominated by amphibole and pyroxene (Fig. 5.18A, B and C). The lighter coloured bands in the sample typically have more quartz and plagioclase (Fig. 5.18D, E and F).

Metamorphic reactions present in the sample are amphibole overgrowing orthopyroxene (Fig. 5.18C), the presence of orthopyroxene and clinopyroxene together, deformation twinning within the plagioclase grains, and in some cases bending of the twins (Fig. 5.18D, E and F).

The sample shows foliation, which is defined by the brighter grey quartz and plagioclase rich bands. Therefore, this represents an S-tectonite.

Fig. 5.17: Sample J1937. Length of the sample: 8 cm.

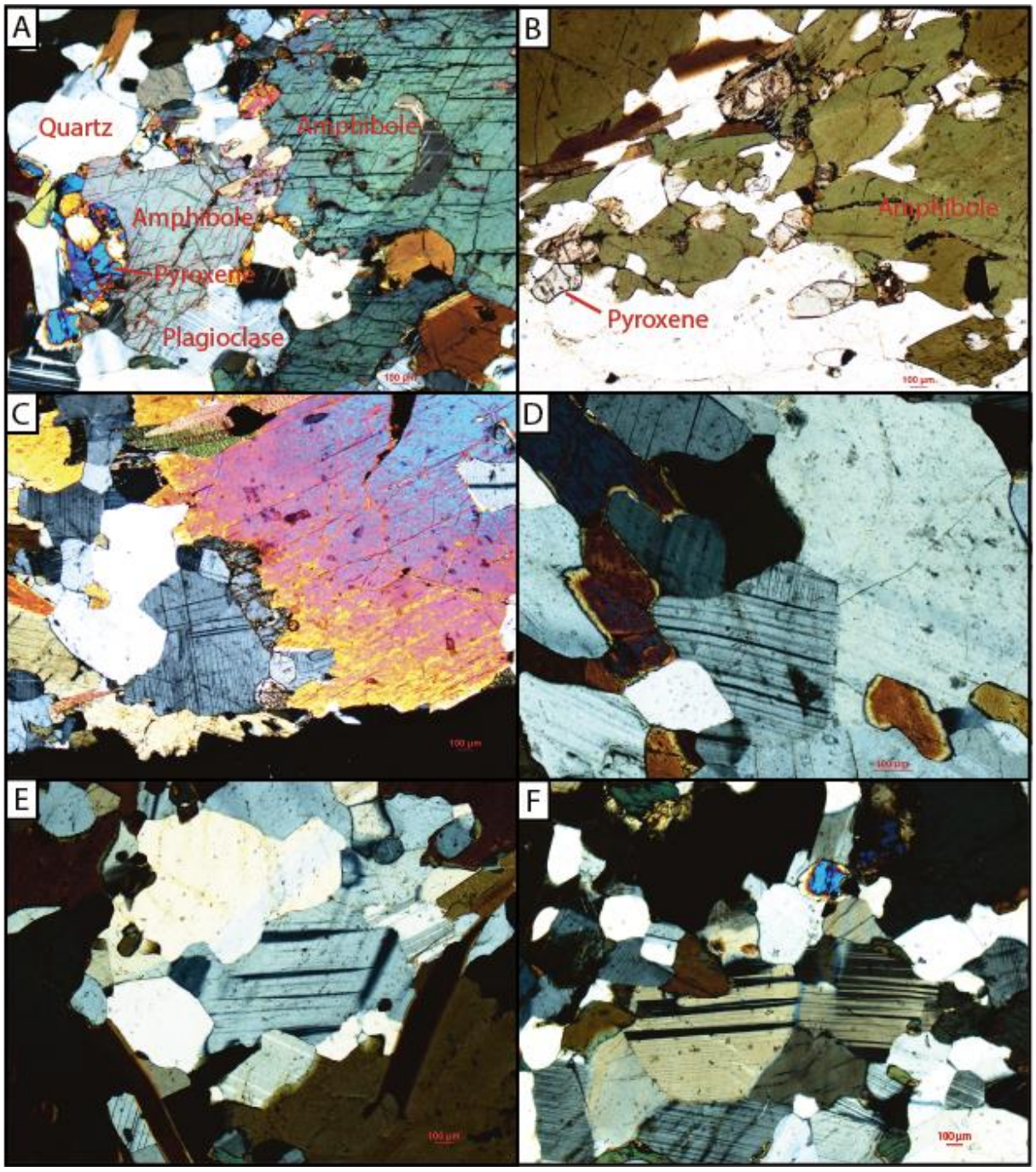

Fig. 5.18: Photomicrographs of sample J1937. A: General XPL photomicrograph of the most common minerals in the thin section. B: PPL photomicrograph of pyroxene and amphibole. C: XPL photomicrograph where amphibole is overgrowing orthopyroxene. D: XPL image of bent plagioclase. E: Deformation twinning in plagioclase. F: Deformation twinning in plagioclase.

5.2 Zircon description and geochronology

The geochronological results will be presented for each individual sample. All the calculated Concordia ages and relevant intercept ages will be presented in a summary at the end of this chapter. The analyses in the Concordia plots have been given different colours based on whether the analyses represent concordant crystallisation ages, metamorphic ages or discordant analyses. The red ellipses represent the concordant crystallisation ages for the analyses. The yellow ellipses represent concordant metamorphic ages for the analyses. The white ellipses represent discordant ages and are excluded from the age calculations. In the post-CL images the colours of the circles that mark the spots are similarly marked to show where the analyses plot in the Tera-Wasserburg Concordia diagram.

J1672 Tonalitic gneiss

The sample contains a mixture of clear and dark zircons, often with inclusions. The grains are mostly elongated with rounded terminations. The grains appear mostly subhedral. The length of the zircons is up to 300 µm, with aspect ratios of up to 3 (Fig. 5.19). Many of the zircons show oscillatory zoning with thin, dark, structureless rims in CL that in most cases were too thin to analyse.

Twenty-five zircons were analysed in twenty-six areas, three rims and twenty-three oscillatory zoned cores. The rims have a Th/U ranging from 0.005–0.02, and the cores with a Th/U from 0.19–0.65.

All analyses, except one, show little common Pb. Therefore, common Pb uncorrected ratios were used apart from one analysis where 204-corrected ratios were used instead.

Nineteen analyses of oscillatory zoned cores give a Concordia age of 1090 ± 5 Ma with a mean square weighted deviation (MSWD) of 0.96 (Fig. 5.19). One core analysis had large errors and two analyses were discordant. Therefore, three analyses were excluded from calculations. One of the discordant analyses point toward an older crystallisation age compared to the ca. 1090 Ma analyses. One rim analysis had large errors and were excluded from the calculations. Two analyses of rims plot concordant near the lower intercept at ca. 560 Ma (Fig. 5.19).

The Concordia age of 1090 Ma is interpreted as the age of crystallisation of the igneous protolith. The ancient Pb-loss most likely occurred because of a metamorphic overprint, which is also evident from the younger rim analyses. The concordant rim analyses at ca. 560 Ma is interpreted to represent the best age for a metamorphic overprint.

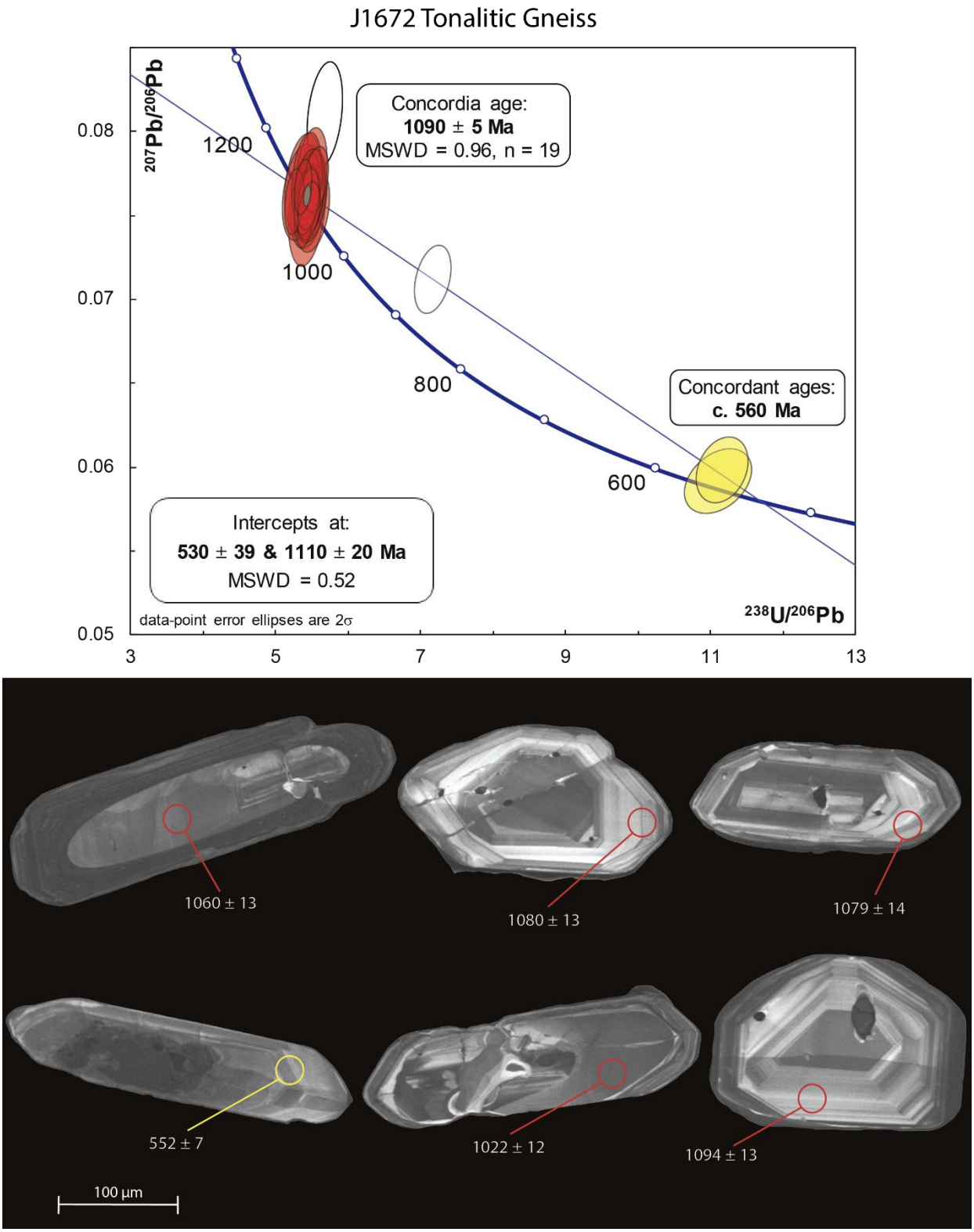

Fig. 5.19: Tera-Wasserburg plot of the analysed zircons of sample J1672. A Concordia age was calculated for the older age group at 1090 ± 5 Ma (red ellipses). The MSWD is that of combined concordance and equivalence. Two analyses show signs of Pb-loss (white ellipses). Two analyses on metamorphic rims gave ages around 560 Ma (yellow ellipses). Bottom figure shows post analysis CL images of selected zircons. The red circles represent the older age group. The yellow circle represents the younger age group.

J1734 Quartzofeldspathic garnet gneiss

The sample contains light brown to clear zircons that are elongated and inclusion-rich. The grains have a length up to 450 µm. On CL images, the zircons are medium to dark. The general aspect ratio is between 2–3. Although many of the grains are dark, oscillatory zoning can be observed. Many of the grains have a thin dark rim, but in most cases, these rims are too thin to analyse (Fig. 5.20).

Twenty-three zircons grains were analysed, including 22 core analyses and one rim analysis. The core analyses have Th/U ratios ranging from 0.05–0.87 and the rim analysis has a ratio of 0.01.

All analyses except one show little common Pb. Therefore, common Pb uncorrected ratios were used apart from one analysis where 204-corrected ratios were used.

Two analysed cores had high errors and were excluded from the calculations. Twelve analyses of cores with oscillatory zoning give a Concordia age of 1103 ± 5 Ma (MSWD = 1.5). Eight of the analysed cores show signs of Pb-loss (Fig. 5.20) and are discordant. The rim analysis is concordant and plots at ca. 538 Ma.

The Concordia age of ca. 1103 Ma is interpreted to represent the crystallisation age of the igneous protolith. The younger rim analysis is interpreted to date a metamorphic zircon re-crystallisation around the older core. The concordant rim analysis at ca. 540 Ma is interpreted to date a significant metamorphic episode.

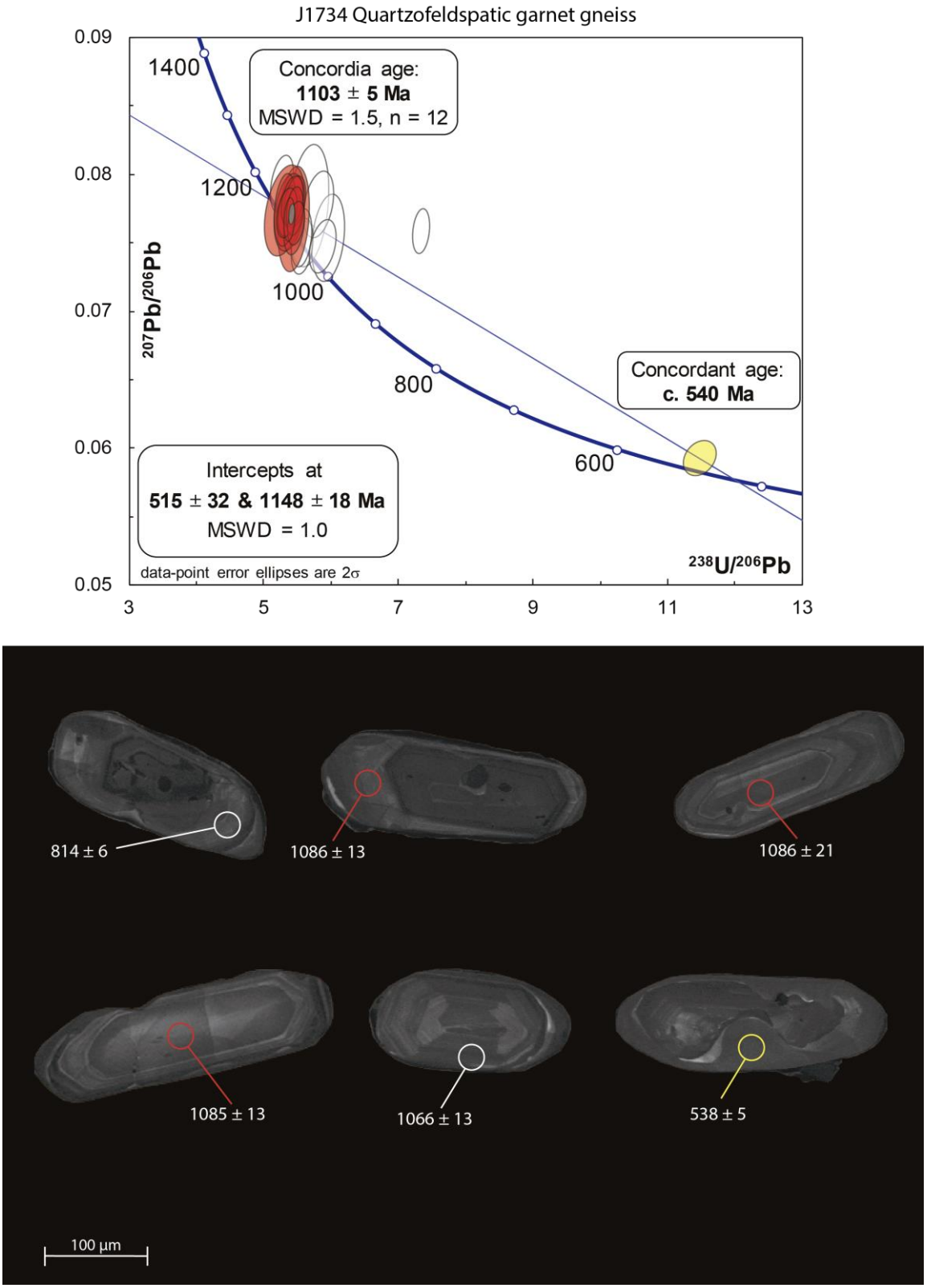

Fig. 5.20: Tera-Wasserburg plot of the analysed zircons of sample J1734. A Concordia age was calculated for the older age group at 1103 ± 5 Ma (red ellipses). The MSWD is that of combined concordance and equivalence. Several analyses show signs of Pb-loss (white ellipses). One analyses on a metamorphic rim gave an age of ca. 540 Ma (yellow ellipse). Bottom figure shows post analysis CL images of selected zircons. The red circles represent the older age group. The yellow circles represent the younger age group. White circles represent Pb-loss.

J1738 Metarhyolite

The sample contains clear to light brown often metamict zircons. The zircons appear subhedral with mostly rounded terminations. On CL images, the grains are generally medium to dark with some brighter grains showing oscillatory zoning. Many grains have thin, dark unzoned rims (Fig. 5.21). The general size of the grains is 150–200 µm, with some grains just above 400 µm. In most cases the rims were too thin to analyse.

All analyses, except four show little common Pb. Therefore, common Pb uncorrected ratios were used apart from four of the analyses where 204-corrected ratios were used.

Twenty-two analyses were completed on 21 oscillatory zoned cores and one rim. The Th/U ratio of the cores ranges between 0.04–0.54, and the rim has a ratio of 0.01.

Five of the oscillatory zoned cores give a Concordia age of 1112 ± 9 Ma (MSWD = 1.4), whilst the other core analyses straddle along the Discordia line due to Pb-loss. One rim analysis plots concordant at ca. 560 Ma (Fig. 5.21).

The Concordia age of ca. 1112 Ma is interpreted to represent the igneous crystallisation age of the granite protolith. Clear evidence of a metamorphic overprint is visible with both the concordant rim analysis with an age of ca. 560 Ma and Pb-loss (lower intercept of the Concordia line at ca. 555 Ma).

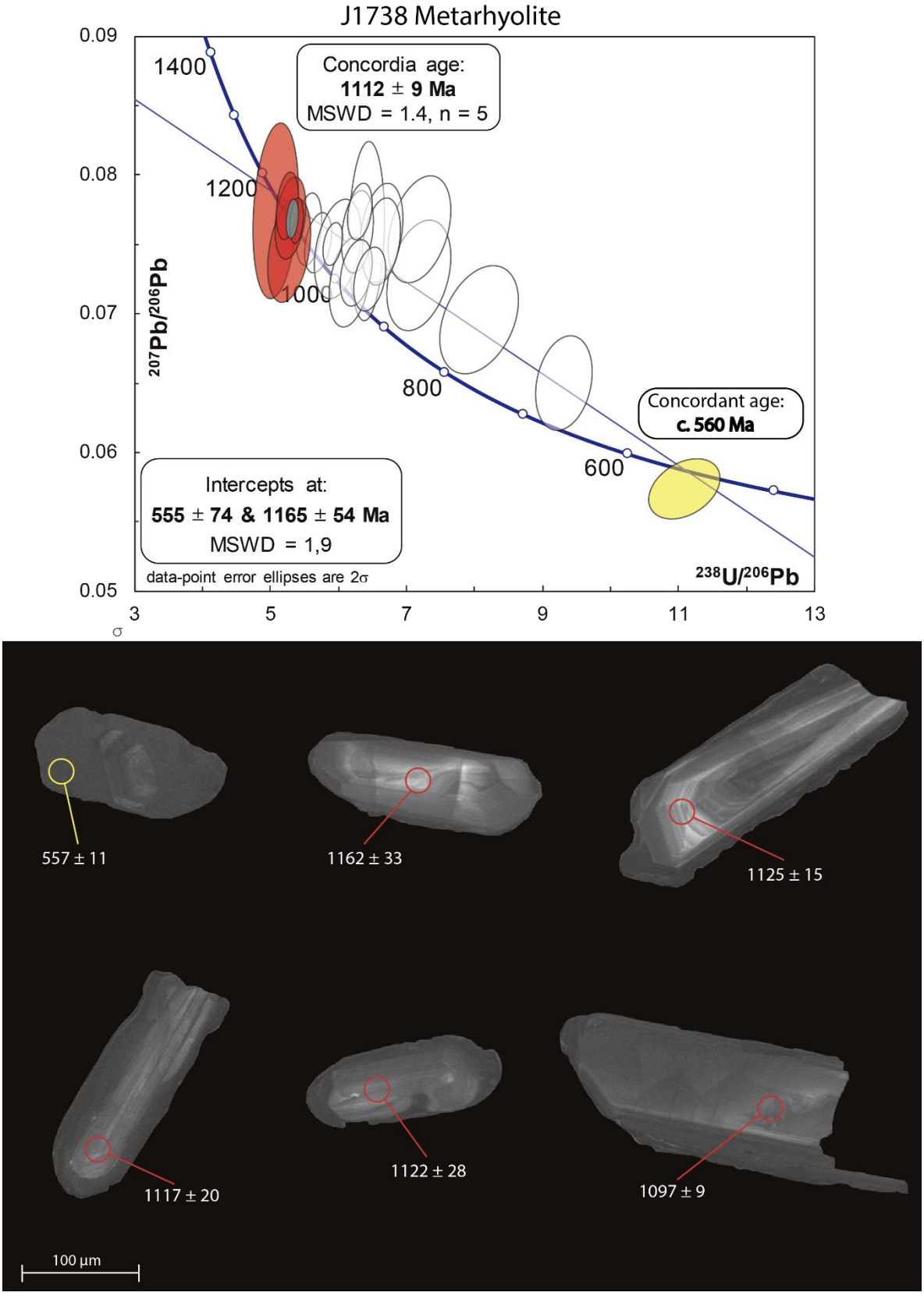

Fig. 5.21: Tera-Wasserburg plot of the analysed zircons of sample J1738. A Concordia age was calculated for the older age group at 1112 ± 8 Ma (red ellipses). The MSWD is that of combined concordance and equivalence. Several of the analyses show signs of Pb-loss (white ellipses). One analyses on a metamorphic rim gave an age of ca. 560 Ma (yellow ellipse). The bottom figure shows post analysis CL images of selected zircons. The red circles represent the older age group. The yellow circle represents the younger age group.

J1773 Garnet-bearing migmatite

The sample contains grains up to 300 µm in length, with aspect ratios generally around 3. The zircons are mostly euhedral, and have a light brown to dark brown colour (Fig. 5.22). On CL images, the sample contains completely dark zircons due to a very high U-content (ranging from 6200–8500 ppm), and the grains therefore appear to be structureless, which could indicate metamictisation (Fig. 5.22).

Despite having a very high U-content, the samples are concordant, which is very unusual for such a high U-content.

This sample appeared to have a significant amount of common lead, and therefore, 208-corrected ratios were used, as common Pb uncorrected and 204-corrected ratois did not give concordant ages.

Twenty core analyses were carried out. The typical Th/U ratios range from 0.04–0.08. Nineteen analyses gave a concordant age of 512 ± 3 Ma (MSWD = 0.87), whereas one of the analyses showed signs of slight Pb-loss (Fig. 5.22).

These analyses are interpreted to represent metamorphic zircon growth during a significant metamorphic event at ca. 512 Ma.

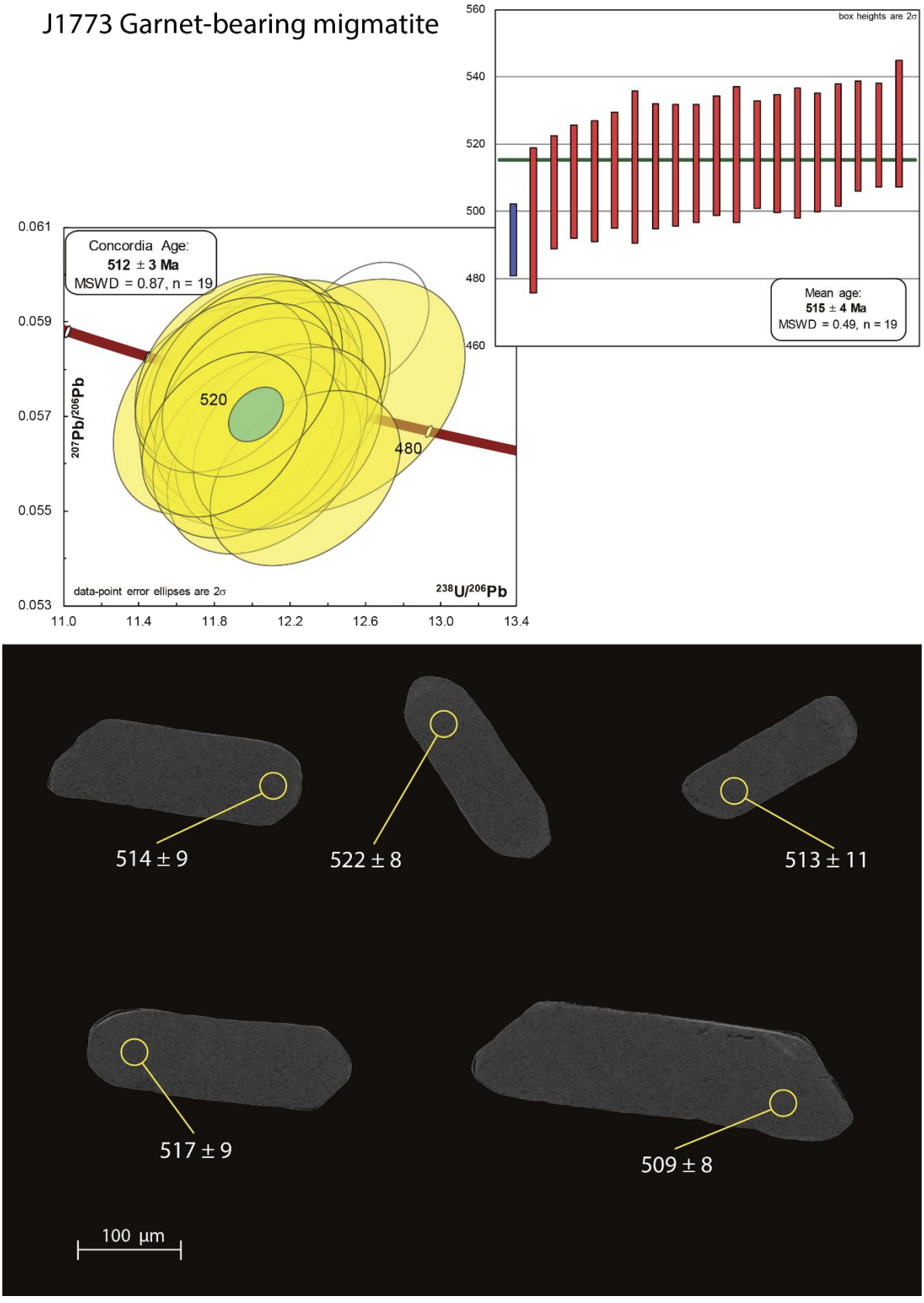

Fig. 5.22: Tera-Wasserburg plot of the analysed zircons of sample J1773. One concordant age was calculated at 512 ± 3 Ma (yellow ellipses). The MSWD is that of combined concordance and equivalence. One analysis show signs of recent Pb-loss (white ellipse). Mean age plot of the concordant 208-corrected ages on the top right side. Bottom figure shows post analysis CL images of selected zircons. The yellow circle represents concordant analyses.

J1782 Garnet gneiss

This sample contains colourless to light brown zircons with rounded terminations, and the grains are mostly anhedral. The grains have a length of up to 400 µm, with aspect ratios between 2 for most of the grains and 3 for some grains (Fig. 5.23). Most of the grains show oscillatory zoned cores, often with thin dark unzoned rims.

This sample appeared to have a significant amount of common lead, and therefore, 208-corrected ratios were used, as the common Pb uncorrected and 204-corrected ratios did not give concordant ages.

Twenty-nine areas were analysed. All the 29 analyses are core analyses with a Th/U ratio between 0.1–0.56.

Ten of the analyses were discarded due to too high analytical errors. Eight analyses gave a Concordia age of 1025 ± 12 Ma (MSWD = 1.7), whilst the other core analyses straddle along the Discordia line. One sample is reversely discordant behind the older grouping, and is not included in the calculations. One completely structureless grain gave a younger age of ca. 611 Ma and is interpreted to have undergone complete Pb-loss during a metamorphic event in this period (Fig. 5.23).

The concordant of ca. 1025 Ma age is interpreted to represent the igneous crystallisation age of the protolith. The concordant age at ca. 611 Ma is interpreted to represent a metamorphic overprint, causing Pb-loss.

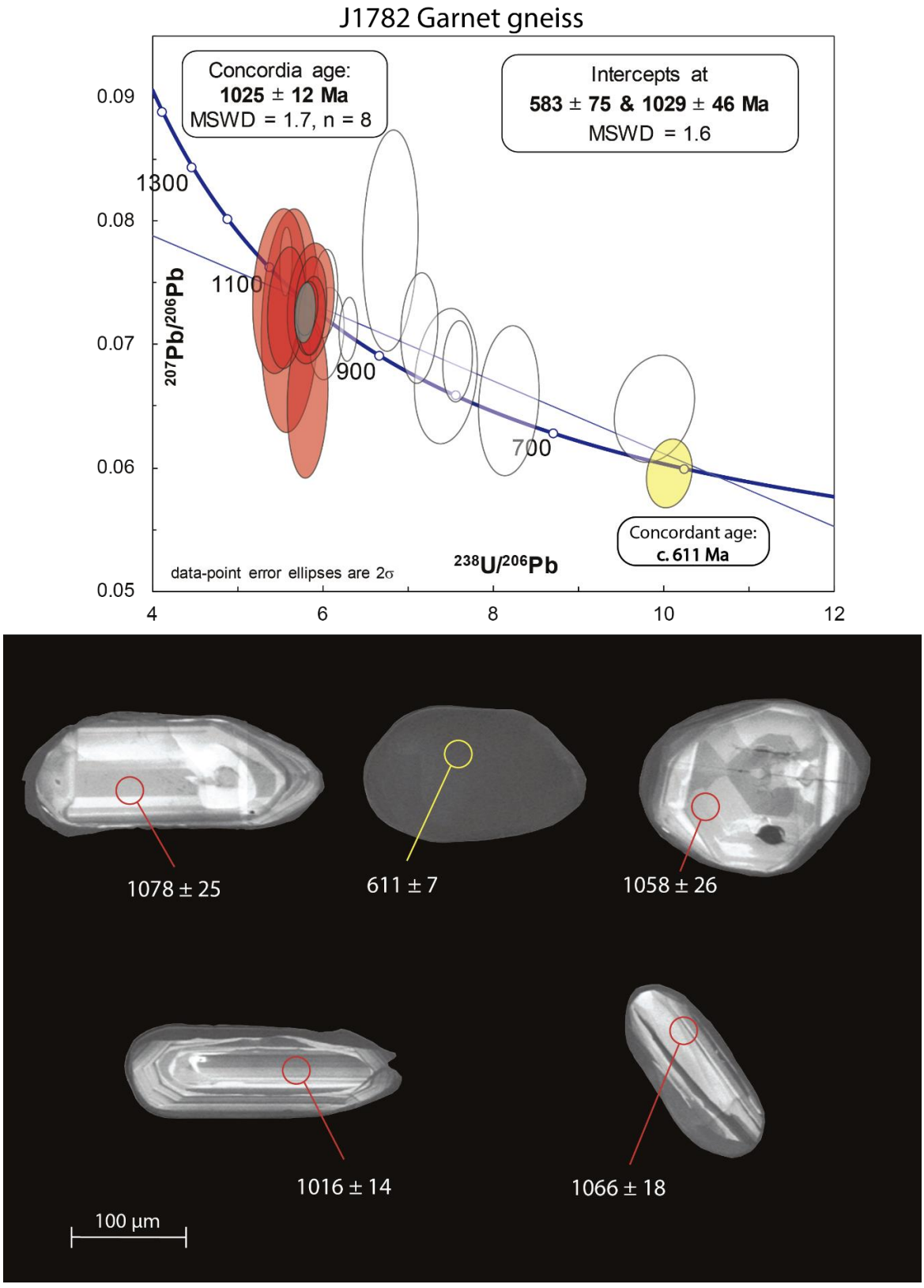

Fig. 5.23: Tera-Wasserburg plot of the analysed zircons of sample J1782. A Concordia age was calculated for the older age group at 1025 ± 12 Ma (red ellipses). The MSWD is that of combined concordance and equivalence. Several analyses show signs of Pb-loss (white ellipses). One analysis on a metamorphic grain gave an age of ca. 611 Ma (yellow ellipse). The bottom image shows post analysis CL images of selected zircons. The red circles represent concordant ages at the upper intercept. The yellow circle represents a concordant age near the lower intercept.

J1793 Migmatitic Tonalite

The sample contains colourless, rounded, anhedral zircons often with inclusions. On CL images, the grains are often light to medium grey and oscillatory zoned, with thin dark unzoned rims. The length of the grains is generally around 200 µm. The aspect ratio of the grains is about 2 (Fig. 5.24). The dark unzoned rims around the zircon grains are in most cases too thin to analyse.

The sample had very little common Pb. Therefore, common Pb uncorrected ratios were used for all analysed grains.

Thirty analyses were carried out on 28 cores and 2 rims. The Th/U ratios of the cores range from 0.29–0.68. One of the analysed rims gave an old age and has a Th/U ratio of 0.26. However, the other analysed rim had a Th/U ratio of 0.01, and gave a younger age.

Twenty-three of the core analyses gave a Concordia age of 1114 ± 5 Ma (MSWD = 1.7), with a few of the cores showing signs of slight Pb-loss (Fig. 5.24). One rim analysis of a younger age plots at ca. 556 Ma and is likely a result of metamorphic re-crystallisation during a metamorphic event.

The concordant age of 1114 ± 5 Ma is interpreted to represent the crystallisation age of the magmatic protolith, and the concordant age of ca. 556 Ma is interpreted to represent a metamorphic overprint.

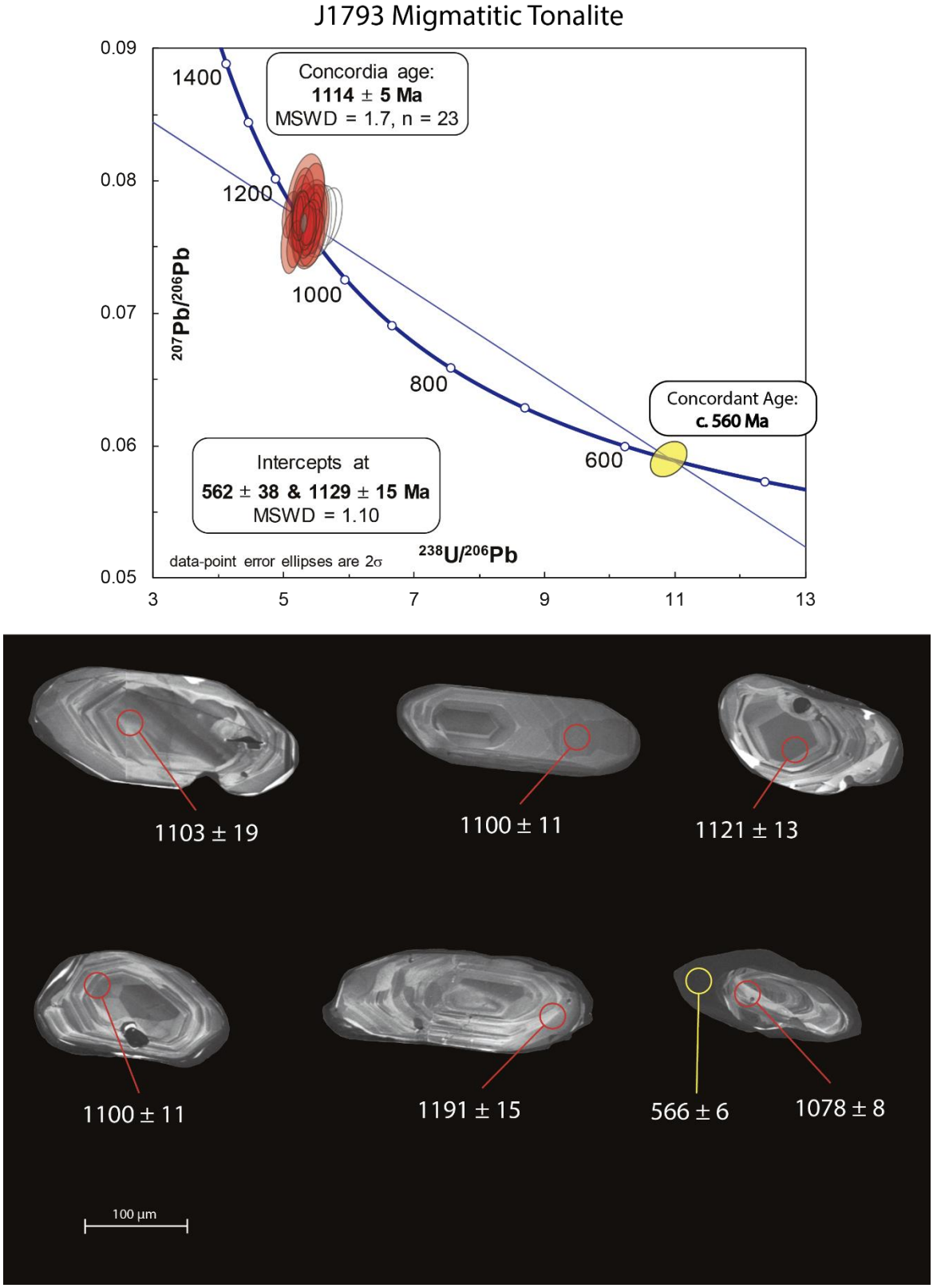

Fig. 5.24: Tera-Wasserburg plot of the analysed zircons of sample J1793. A Concordia age was calculated for the older age group at 1114 ± 5 Ma (red ellipses). The MSWD is that of combined concordance and equivalence. Several analyses show signs of Pb-loss (white ellipses). One analyses on a metamorphic grain gave an age of ca. 560 Ma (yellow ellipse). The bottom image shows post analysis CL images of selected zircons. The red circles represent concordant ages at the upper intercept. The yellow circle represents a concordant analysis near the lower intersect.

J1807 Orthopyroxene-bearing enderbite

This sample contains bright brown zircons often with metamict cores. The size of the grains is around 200 µm, with some zircons up to 400 µm. The zircons are generally subheadral with rounded terminations. The aspect ratio of the grains is generally around 3 (Fig. 5.25). In CL this sample is characterised by bright oscillatory zoned cores with dark unzoned rims, in most cases thick enough to analyse.

In most cases, very little common Pb was present in the analyses. Therefore, common Pb uncorrected ratios were used except for one analysis.

Twenty-seven analyses were placed on 21 rims and 6 cores. The Th/U ratio of the cores is ranging from 0.19–0.36, and the rims have a Th/U ratio between 0.01–0.13.

The six core analyses show significant scatter, mostly due to Pb-loss, and three core analyses show signs Pb-loss and were consequently excluded in the age calculation. The concordant core analyses gave a Concordia age of 1130 ± 11 Ma (MSWD = 1.03), and 19 rim analyses gave a Concordia age of 528 ± 3 Ma (MSWD = 1.17) (Fig. 5.25).

The age of ca. 1130 Ma is interpreted to represent the crystallisation age of the igneous protolith, and the age of 528 ± 3 Ma is interpreted to represent a high-grade metamorphic overprint, forming the wide, dark, unzoned rims.

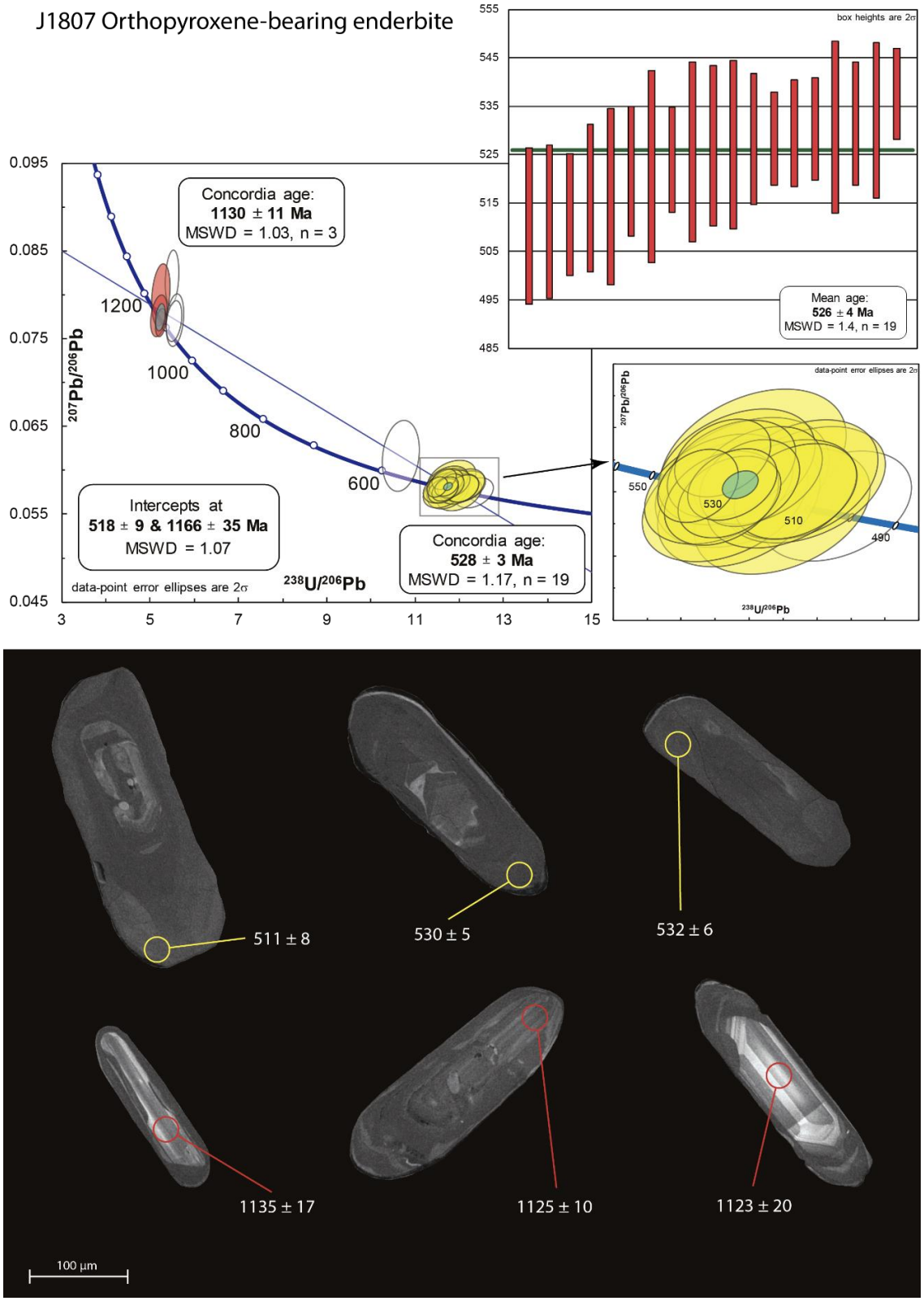

Fig. 5.25: Tera-Wasserburg plot of the analysed zircons of sample J1807. A Concordia age was calculated for the older age group at 1130 ± 11 Ma (red ellipses). The MSWD is that of combined concordance and equivalence. Several analyses show signs of Pb-loss (white ellipses). A Concordia age was calculated for the younger age group at 528 ± 3 Ma (yellow ellipses). Mean age plot for the concordant ages in the top right corner. A zoomed in version of the Concordia age at the lower intercept. The bottom image shows post analysis CL images of selected zircons. The red circles represent concordant ages at the upper intercept. The yellow circles represent concordant ages in the lower intersect.

J1848 Garnet gneiss, supracrustals

The sample contains a mixture of large zircons (700 µm) and smaller zircons (generally between 200–350 µm), often with inclusions. Most crystals are well developed with euhedral to subhedral shapes. The zircons are characterised by bright oscillatory zoned cores with medium to dark unzoned rims. The aspect ratio of the grains is around 3 (Fig. 5.26).

This sample appears to have a significant amount of common lead, and therefore, 208-corrected ratios were used as the common Pb uncorrected and 204-corrected ages did not give concordant ages.

Thirty-three analyses were carried out on 25 grains. Of the 33 analyses, 15 are core analyses and 18 are rim analyses. The Th/U ratios of the core analyses range from 0.17–0.58, and the rims show a range of 0.08–0.25.

The analyses are scattered along the Concordia. This scatter is likely a result of this being a metasedimentary unit. However, two distinct age groups occur. The oldest group has a Concordia age of 637 ± 6 Ma (MSWD = 1.9). The youngest group appear to have a single common age with a Concordia age of 563 ± 3 Ma (MSWD = 1.3) (Fig. 5.26).

The scatter in the plot is interpreted to represent the detrital origin of the zircon cores, and the Concordia age of ca. 637 Ma could represent a single source that was particularly prominent in the source area. The younger age of 563 ± 3 Ma is likely to represent a metamorphic overprint of the sedimentary protolith.

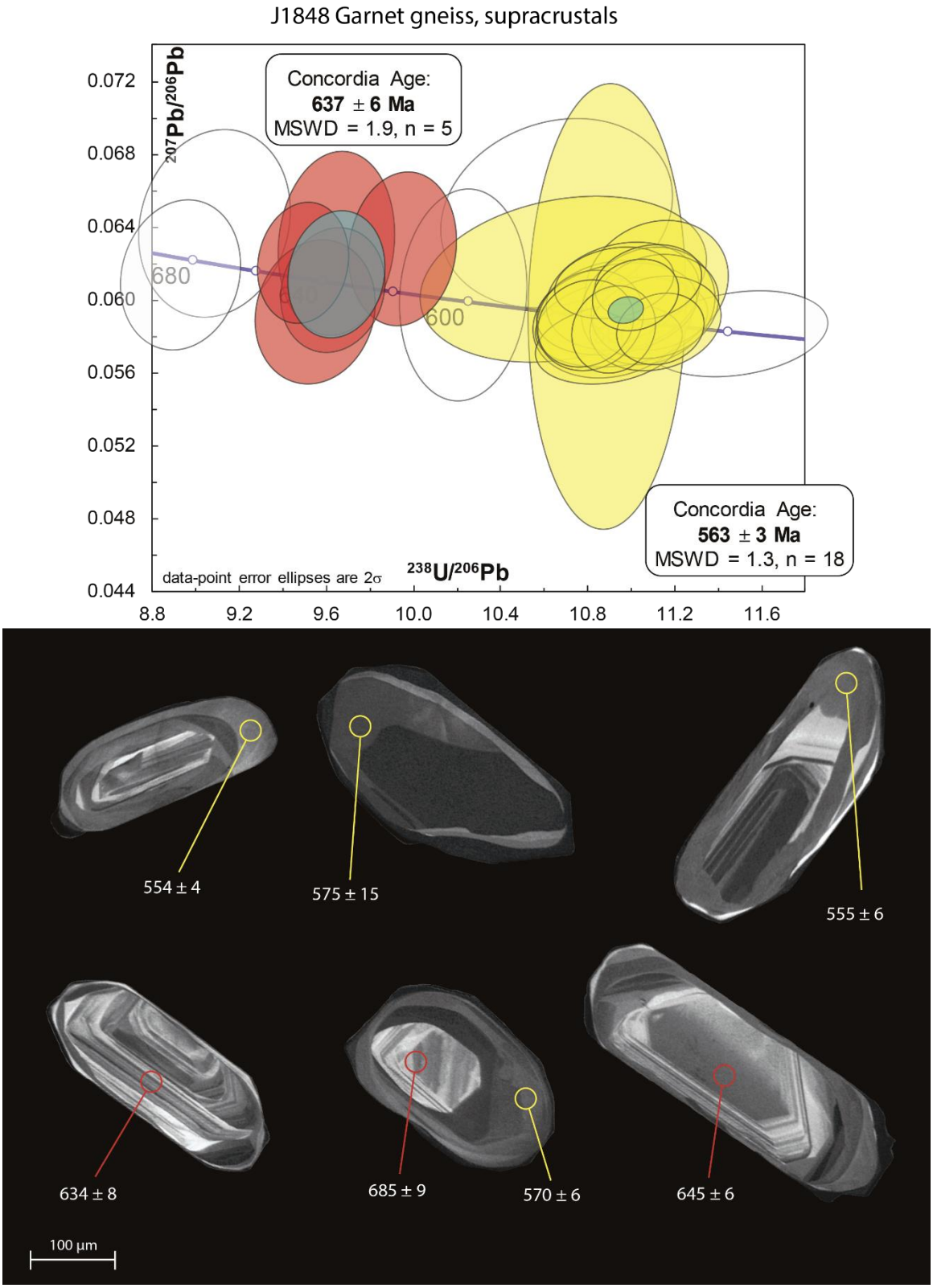

Fig. 5.26: Tera-Wasserburg plot of the analysed zircons of sample J1848. A Concordia age was calculated for the older age group at 637 ± 6 Ma (red ellipses). The MSWD is that of combined concordance and equivalence. Several analyses scatter along the Concordia line (white ellipses). A Concordia age was calculated for the younger age group at 563 ± 3 Ma (yellow ellipses). The bottom image shows post analysis CL images of selected zircons. The red circles represent concordant ages of the older group. The yellow circle represents a concordant analysis near the lower intersect.

J1937 Mafic granulite

This sample contains clear, rounded, anhedral typical metamorphic zircons that have a grain-size between 100–250 µm in length, with aspect ratios of 3 (Fig. 5.27). On CL images, most zircons show either sector zoning, or no zoning at all. There are a few zircons however, that show oscillatory zoning. The zircons in this sample show very different characteristics in CL, compared to the other samples in this study. Many zircons show very small, bright cores with wide sector zoned or unzoned, dark, typical metamorphic rim. Some of the grains lack the small, bright cores, and consist entirely of sector zoned or unzoned apparent metamorphic zircon.

This sample appears to have a significant amount of common lead, and therefore, 208-corrected ratios were used, as the common Pb uncorrected and 204-corrected ratios did not give concordant ages.

Thirty-three analyses were carried out on 31 grains. Twenty-eight spots were chosen on unzoned or sector zoned areas, and the remaining five analyses were on the smaller cores.

Two distinct age groups were calculated. Two of the analysed rims were discarded due to high errors. Two other analysed rims showed slight Pb-loss. Twenty-four of the analyses on unzoned or sector zoned areas gave a Concordia age of 582 ± 3 Ma (MSWD = 0.79) (Fig. 5.27). The four core analyses gave a concordant age of 613 ± 8 Ma (MSWD = 0.96) (Fig. 5.27). One grain in the sample showed an old age of 1048 Ma. This zircon, however, could be a result of inheritance or contamination as the grain looks different from the other zircons in the sample and is therefore excluded.

The younger Concordia age of ca. 580 Ma is interpreted to represent a high-grade metamorphic event. The older age group of ca. 637 Ma might represent the crystallisation age of the igneous protolith.

Summary of calculated ages

Six samples of this study recorded interpreted Mesoproterozoic crystallisation ages ranging from ca. 1130–1025 Ma. Two of the samples recorded younger crystallisation ages at ca. 637 Ma and ca 613 Ma. All nine samples recorded metamorphic ages ranging from ca. 611–512 Ma. The summary of the calculated ages of this study is presented in Fig. 5.28 with parts of the geologic timescale for perspective purposes.

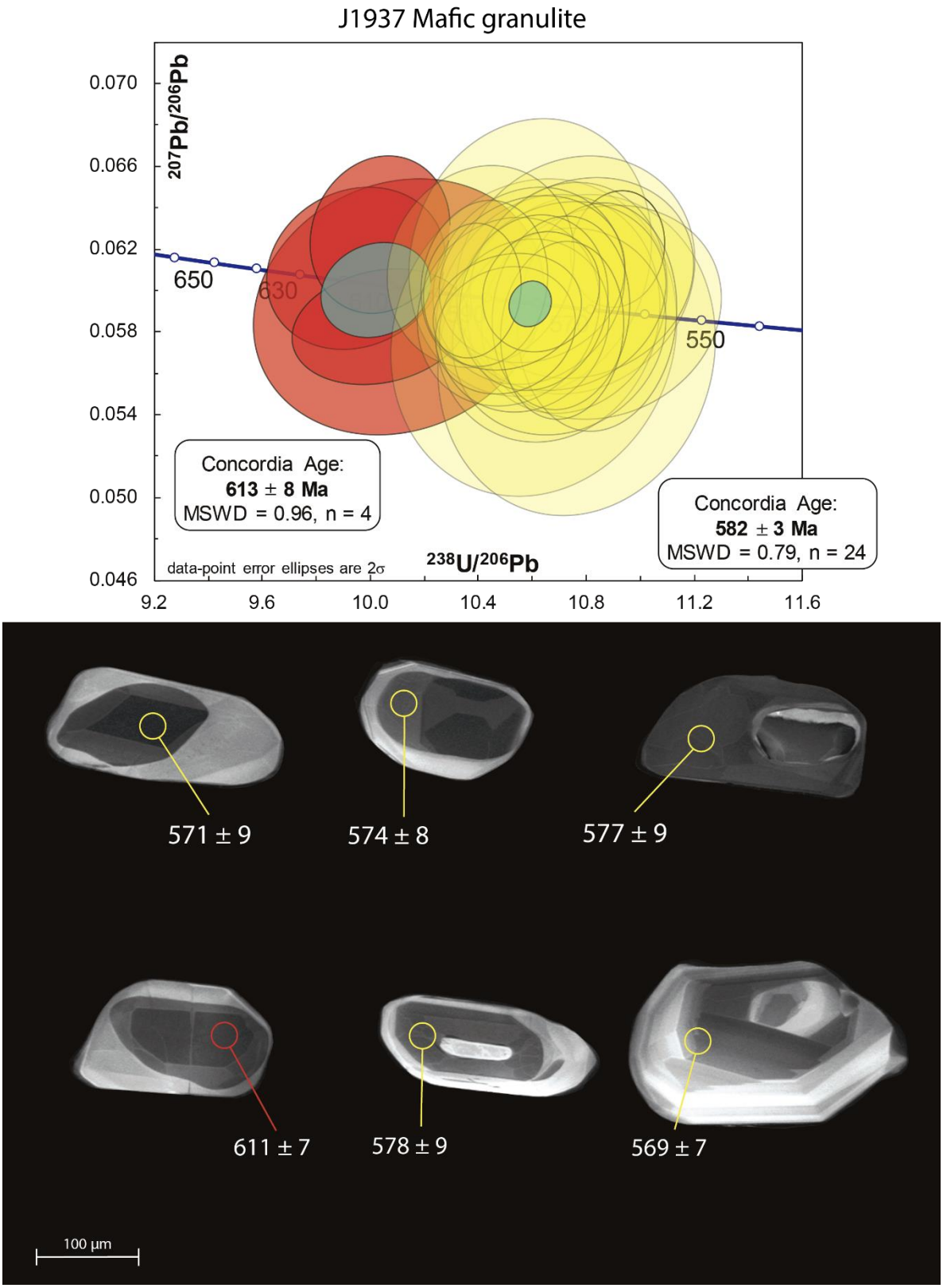

Fig. 5.27: Tera-Wasserburg plot of the analysed zircons of sample J1734. A Concordia age was calculated for the older age group at 613 ± 8 Ma (red ellipses). The MSWD is that of combined concordance and equivalence. A Concordia age was calculated for the younger age group at 582 ± 3 Ma (yellow ellipses). The bottom image shows post analysis CL images of selected zircons. The red circles represent concordant ages of the older group. The yellow circle represents a concordant analysis near the lower intersect.

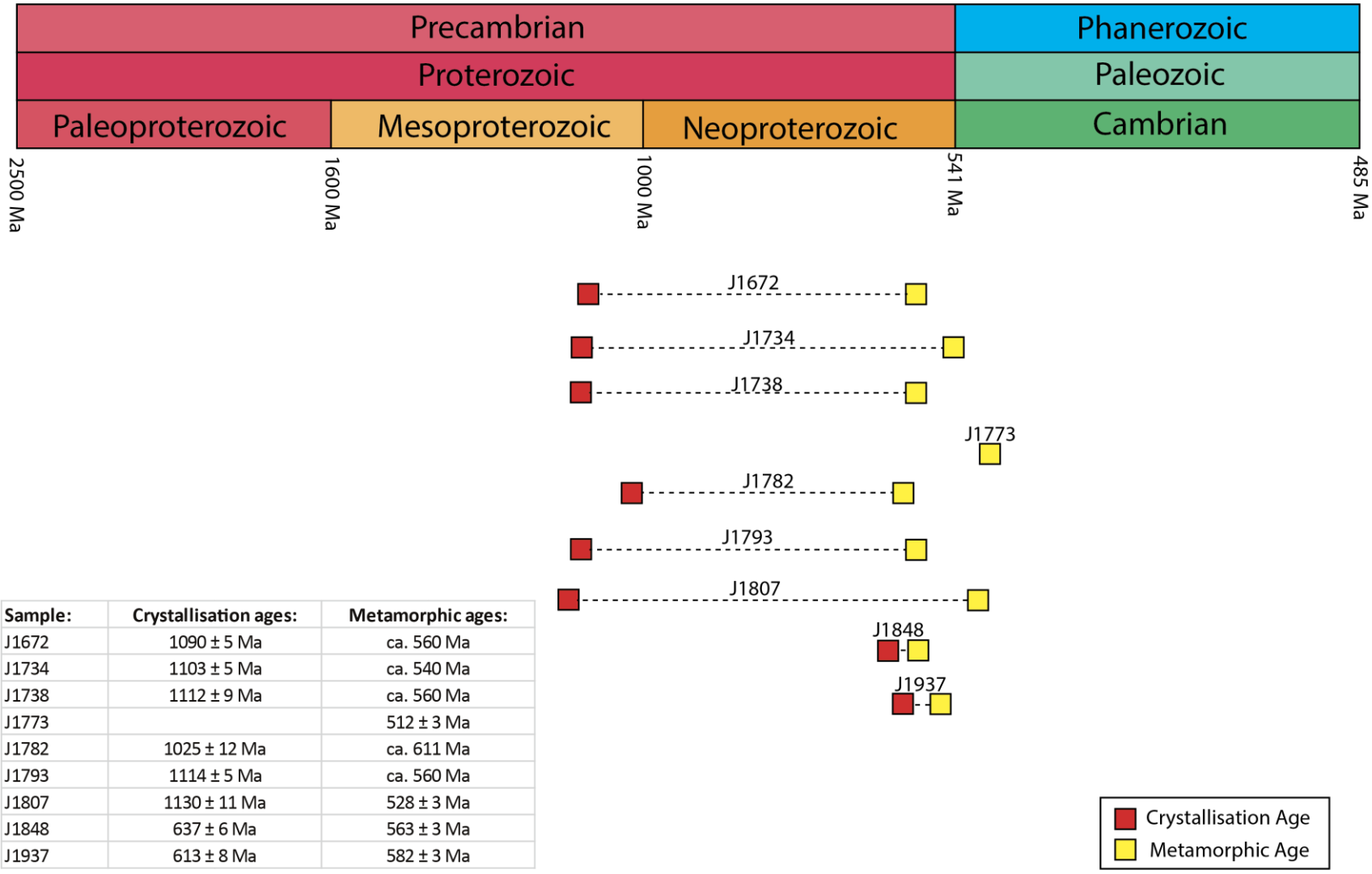

Sample:	Crystallisation ages:	Metamorphic ages:
J1672	1090 ± 5 Ma	ca. 560 Ma
J1734	1103 ± 5 Ma	ca. 540 Ma
J1738	1112 ± 9 Ma	ca. 560 Ma
J1773		512 ± 3 Ma
J1782	1025 ± 12 Ma	ca. 611 Ma
J1793	1114 ± 5 Ma	ca. 560 Ma
J1807	1130 ± 11 Ma	528 ± 3 Ma
J1848	637 ± 6 Ma	563 ± 3 Ma
J1937	613 ± 8 Ma	582 ± 3 Ma

Fig. 5.28: Summary of the calculated geochronological ages in this study. The upper part of the figure consists of the ages plotted within the geological timescale. A table with the calculated ages of this study is presented in the lower left corner.

Geographical position of the calculated ages

The geographical position of the calculated ages is presented in Fig. 5.29. The position of the collected samples is plotted along with the calculated ages.

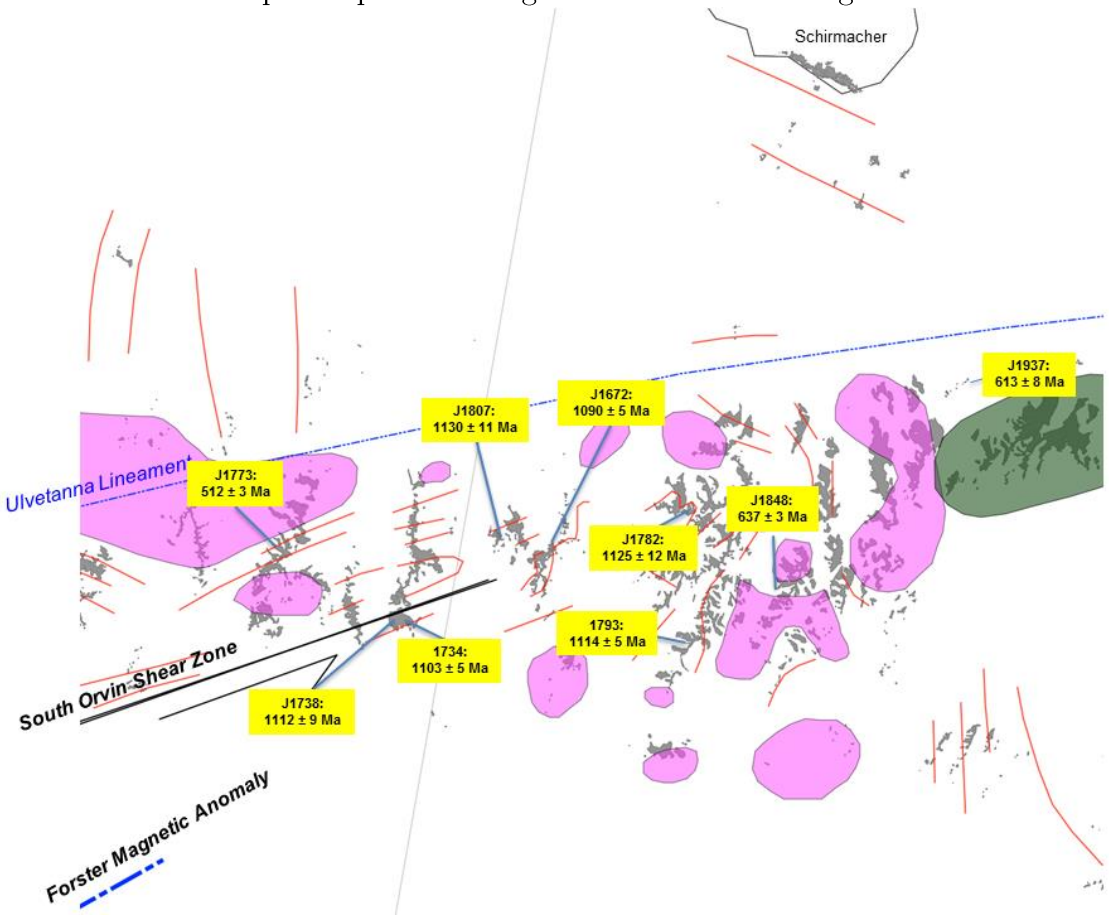

Fig. 5.29: Map of the sample localities along with the calculated ages from the geochronological results of this study.

6. Discussion

This discussion is separated in two main parts: The first part will describe the interpretation of the data from the results chapter. Here an interpretation of petrographic characteristics related to mineral compositions and metamorphic reactions will be presented. The calculated U/Pb ages will be interpreted to understand when the samples formed, and when the samples were transformed during metamorphic processes. The second part of the discussion will compare the interpreted data with the state of the art literature, and discuss the implications the present study provides on the regional geology, based on the research questions presented in the introduction.

6.1 Interpretation of the geochronological and petrography results

J1672, J1734, J1738, J1782, J1793 and J1807

Based on similar crystallization ages, Th/U and petrographic characteristics, I interpret this group of rocks to represent a suite of meta-igneous rocks that formed during the same period or geological event, in Late Mesoproterozoic times. All these samples are interpreted to have an igneous crystallisation age between ca. 1130–1025 Ma. The identification of these samples as igneous rocks is based on the typical igneous oscillatory zoning, and higher Th/U ratios (normally above 0.1) (e.g Corfu et al., 2003). Most of the samples within this group have mineral compositions consisting of quartz along with a mixture of plagioclase and microcline as the dominant minerals. One exception is sample J1738, a metarhyolite, which consists almost entirely of quartz and microcline. In most samples plagioclase predominates over microcline, indicating that these samples have granodioritic to tonalitic protoliths. This in turn, may indicate that these rocks possibly formed within an island arc, continental arc setting. Four of the samples within this group (J1672, J1734, J1782, J1807) show slight signs of inheritance from older sources ranging from ca. 1200–1150 Ma. In general, however, these rocks show little evidence of inheritance, which further supports a volcanic arc setting during formation.

The metamorphic characteristics of the samples vary slightly. However, common characteristics are ribbon quartz, or highly re-crystallised quartz grains with undulose extinction and, in some cases, deformation fissures within the quartz grains. These types of structures are associated with medium to high-grade metamorphism (e.g. Shelley, 1993). The presence of garnet and occasionally orthopyroxene in three samples points towards medium to high-grade metamorphic conditions. This is in some cases accompanied with re-crystallised microcline that indicates temperatures of > 450°C. Evidence for retrogression is present in most of the samples with patchy growth of biotite and symplectic biotite.

The age of metamorphism in these samples is in many cases not well constrained. This is because the zircons often lacked wide enough metamorphic rims to allow for analyses. However, in J1807 several metamorphic rims were analysed, and gave a well constrained age that is interpreted to represent a high-grade metamorphic overprint at 528 ± 3 Ma. Although very few metamorphic rims were analysed on the other samples, all the Mesoproterozoic samples did contain one or two analyses on rims with completely reset grains. These metamorphic rim analyses recorded ages between ca. 611–540 Ma with lower intercept ages of the Discordia between ca. 583–515 Ma. The interpretation of metamorphic overprinting is further supported by both recent and ancient Pb-loss, present in all the samples in this age group, as well as low Th/U dark, unzoned rims.

J1848

Sample J1848 is interpreted to represent a metasedimentary rock based on the zircons having clear detrital characteristics. The smaller eroded magmatic cores have wide unzoned or sector zoned rims interpreted as metamorphic overgrowth (e.g. Corfu et al., 2003). In the Tera-Wasserburg plot, the analysed samples scatter along the Concordia line, which is to be expected for a detrital sample. There are, however, two distinct age groups for which Concordia age could be calculated in this sample. The older concordant age group of 637 ± 6 Ma is interpreted to represent detrital zircons possibly derived from a particularly prominent igneous source. The mineralogical composition of the sample is dominated by plagioclase as well as abundant quartz, with some microcline. As this is a sedimentary protolith, several different sources most likely contribute to the composition. However, the presence of mainly plagioclase and quartz is a good indication that the igneous source/sources of this sample have a granodioritic to tonalitic composition. This in turn indicates that the igneous formation probably occurred in an island arc or continental arc setting at ca. 637 Ma.

This sample is interpreted to have been subjected to medium to high-grade metamorphism based on mineral characteristics such as re-crystallised quartz grains with undulose extinction and the presence of garnets. Sericitised plagioclase is very typical in this sample, indicating that alteration by fluids affected this rock (Que and Allen, 1996). Evidence for retrogression based on patchy growth of biotite around the edges of plagioclase and quartz grains, as well as around garnet grains, indicate that this sample has been subjected to pressures and temperatures above the stability field of biotite.

The younger age group of this sample gave a well constrained age of 563 ± 3 Ma and is interpreted to represent a medium to high-grade metamorphic event. This event caused

the growth of dark, unzoned or sector zoned metamorphic rims around the detrital zircon grains with low Th/U ratios.

J1937

Based on the mineralogical composition and zircon characteristics, this sample is interpreted to represent a meta-igneous rock that crystallised at 613 ± 8 Ma. This interpretation is based on higher Th/U ratios (> 0.1) and characteristic igneous zircon cores. There is, however, a difference between the igneous cores in this sample compared to the other samples in the present study. The cores are in many cases unzoned or sector zoned, and mostly very small. The mineralogical composition of this sample differs from the previous samples in having a more mafic composition. The sample contains mostly pyroxene (both orthopyroxene and clinopyroxene), amphibole and quartz, indicating a more mafic composition.

This sample is interpreted to have undergone high-grade metamorphism, based on the combined occurrence of orthopyroxene and clinopyroxene within the sample, indicating granulite facies conditions. Deformation twinning, and in some cases bending of plagioclase twins, are also good indicators of metamorphism at temperatures exceeding ca. 450°C. Additionally, typical metamorphic unzoned rims further support this interpretation. Signs of retrogression is present in this sample, where amphibole has crystallised over the existing orthopyroxene grains.

The younger age group is therefore interpreted to represent the age of metamorphic overprinting at 580 ± 3 Ma, causing growth of metamorphic zircon rims around the small igneous cores.

J1773

This sample differs from the rest of the analysed samples by having zircons that formed entirely during metamorphism. The zircons in this sample are often euhedral, with very low Th/U ratios (< 0.1), and are interpreted to represent metamorphic zircons that crystallised during migmatitisation at 512 ± 3 Ma. Large ribbon quartz grains with undulose extinction, as well as orthopyroxene are good indicators of granulite facies metamorphism. This sample is interpreted to be of entirely metamorphic origin where the zircons crystallised during migmatisation.

6.1.1 Common Metamorphic ages for all samples of this study

All samples from the present study show signs of high-grade metamorphic overprinting, interpreted to be within upper amphibolite to granulite facies. This metamorphic overprinting has a similar age for all the nine samples, ranging from ca. 611–512 Ma. This interpretation is based on the analyses of darker, unzoned and/or sector zoned rims that represent metamorphic zircon re-crystallisation, in combination with metamorphic petrographical characteristics (e.g. Corfu et al., 2003; Shelley, 1993). The metamorphic ages are interpreted to very likely be related to a major orogenic event resulting in high-grade metamorphism within the study area.

6.1.2 Significance for ages in relation to major orogenic events/cycles

Fig. 6.1 summarises all the single spot analyses sorted by age within this study (analyses with age errors $> 5\%$ are excluded). The ages from all analysed grains show two distinct age-plateaus form. The first group (blue zone) shows an age-plateau within the timeframe of ca. 1130–1050 Ma. The ages of this group are followed by significant tail because of Pb-loss between the blue zone and green zone. The second group (green zone) gives an age-plateau within a timeframe of ca. 590–510 Ma. Within this age-plateau (green), two distinct groups occur between ca. 590–550 Ma (yellow) and ca. 530–510 Ma (purple), which could represent different metamorphic stages during an orogenic event (lower figure). Prior to the metamorphic event in the green zone, igneous formation at ca. 637 Ma is present (red zone). The lower zone (green), can therefore be sub-divided into three groups: (1) The red group represents igneous formation at ca. 637 and ca 613 Ma. (2) The yellow group represents the first metamorphic stage. (3) The purple group represents a secondary metamorphic event.

The data presented in Fig. 6.1 show a pattern of two major groups (green and blue zones). The two age groups are interpreted to represent two separate orogenic cycles with a 500 Ma gap between the cycles, which could relate to the formation of the two supercontinents Rodinia and Gondwana, respectively. This further suggests that Dronning Maud Land is an important area for the reconstruction of both Rodinia and Gondwana supercontinent reconstruction, and likely represents the southern extent of the East African Orogen, as previously suggested by several authors (e.g. Jacobs et al., 1998; Shiraishi et al., 1994).

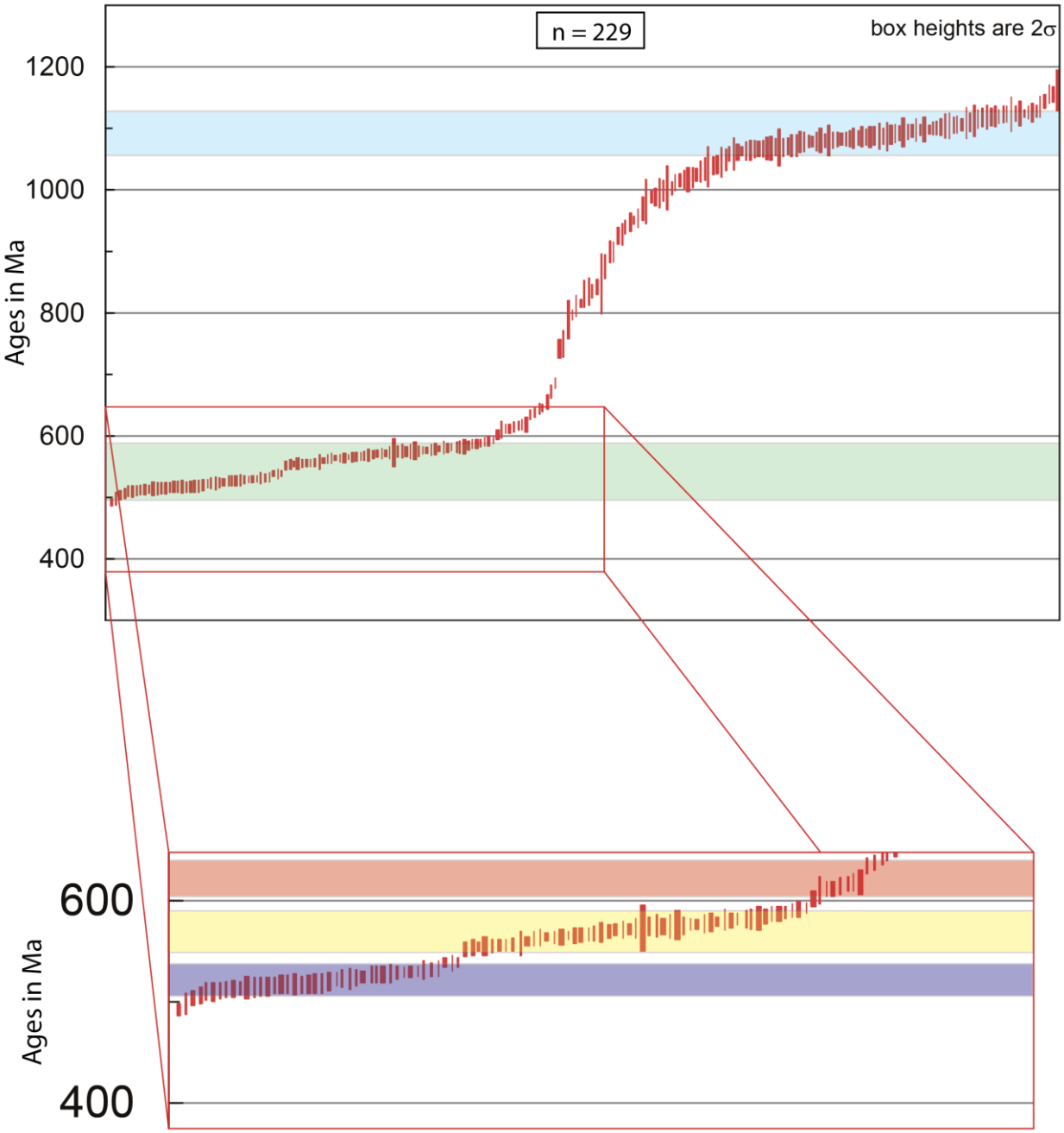

Fig. 6.1: Age distribution of all the acquired ages of this study. All the analysed spots are present, and shown with 2σ–error bars. Ages with errors > 5% are excluded from this plot. The upper figure shows two distinct age groups. The blue zone represents the crystallisation ages of the basement within this study. The green zone represents the tectono-thermal event related to the "Pan-African" event. This event can be further sub-divided (lower figure) into three stages, starting with igneous activity at ca. 637 Ma (red). The second stage represents the first high-grade metamorphic overprinting within the study area (yellow). The third stage represents a secondary late-stage metamorphic event (purple).

6.2 Late Mesoproterozoic crustal formation

Six samples from this study give Concordia ages that are interpreted to represent igneous crystallisation ages of Late Mesoproterozoic basement, with U/Pb ages ranging from ca. 1130–1025 Ma. Previous studies within the same area from Jacobs et al. (1998) reported similar igneous crystallisation ages for various granitic gneisses, ranging from ca. 1130–1070 Ma. Subsequent metamorphism was reported at ca. 1085 to 1075 Ma (Jacobs et al., 1998). No evidence for Grenville-age metamorphism was found in this study. This could be the result of complete resetting of the zircons during the Late Neoproterozoic/Early Paleozoic "Pan-African" tectono-thermal overprinting. The interpreted ages for basement formation within the present study area, therefore, clearly indicate that the entire area is still a part of the Maud Belt within western and central Dronning Maud Land. None of the analysed basement samples of this study revealed ages similar to the Tonian Oceanic Arc Super Terrane (TOAST) (Jacobs et al., 2015). Furthermore, similar Late Mesoproterozoic basement crystallisation ages have been reported throughout central DML and into western DML. This is further connecting the Mesoproterozoic basement ages from the present study with the Mesoproterozoic Maud Belt (e.g. Arndt et al., 1991; Bauer et al., 2003a; Bauer et al., 2003b; Board et al., 2005; Harris et al., 1995; Jackson, 1999; Jacobs et al., 1996; Jacobs et al., 1999; Paulsson and Austrheim, 2003). This study, therefore add new data within an important area north-west of the FMA and concludes that the basement rocks analysed in this study represent the eastern part of the Mesoproterozoic Maud Belt. Thus, the lack of U/Pb-ages related to the TOAST indicate that the boundary between the two terranes must lie further east than the study area of this project.

6.2.1 Implications for the Maud Belt/TOAST boundary

The eastern boundary of the Maud Belt that separates the TOAST in the southeast from the Maud Belt in the northwest is, as mentioned earlier, a matter of ongoing debate. However, the most recent studies suggest that the Forster Magnetic Anomaly (FMA) (Fig. 2.9) represents the main boundary between the two terranes. (Jacobs et al., 2015; Riedel et al., 2013).

This project was aimed at further investigating a previously studied area by Jacobs et al. (1998), in order to confirm that the basement rocks within the study area are in fact entirely made up of the Mesoproterozoic Maud Belt, as previously assumed. Because of

the lack of Tonian U/Pb zircon ages present in this study, the boundary between the TOAST and the Maud Belt cannot be within the study area. Riedel et al. (2013) proposed that this boundary might project into the area around Orvinfjella. If this boundary was present in the study area, one would expect to find U/Pb ages that correlate with the TOAST on the south-eastern side, and U/Pb ages that correlate with the Maud Belt on the north-western side. This is, as previously addressed, not present within this study, nor in previous studies from Jacobs et al. (1998). Therefore, the continuation of the boundary between the Maud Belt and the TOAST can be re-interpreted.

Fig. 6.2 shows the interpreted contact based on the trajectory of the FMA from Riedel et al. (2013) (top left corner with white dashed line). Riedel et al. (2013) proposed that this boundary projected into the study area of this project. However, I propose that this boundary rather slightly bend eastwards as the FMA abruptly stops south of the study area and continues northeast towards the northern coast of central DML (Fig. 6.2 (top left corner with black dashed line)). The figure sows the calculated crystallisation ages of this study on the map marked with blue rectangles. The red rectangles represent the ages reported in Jacobs et al. (1998). The interpreted boundary is based on how far east the typical Maud Belt ages (1100-1000 Ma) can be traced in the study area. This means that the boundary could possibly be close to the study area. Future studies within this key area could reveal the exact position of this boundary.

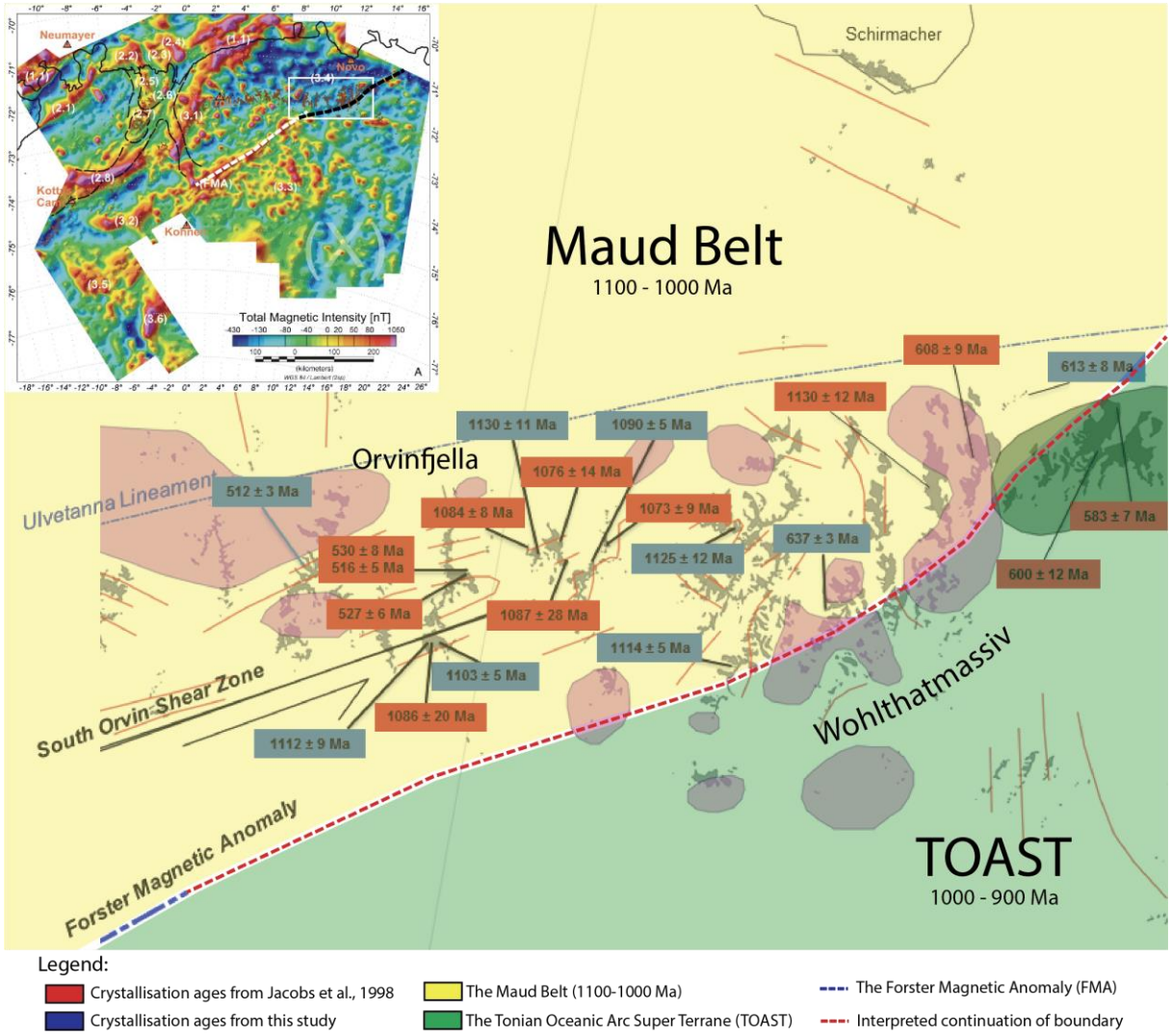

Fig. 6.2: Top left corner: Aeromagnetic anomaly map of western and central Dronning Maud Land. The white dashed line represents the interpreted projection towards Kurze Mts. by Riedel et al. (2013). The black dashed line is the re-interpreted projection of the Maud Belt/TOAST boundary, based on the present study. The white rectangle represents the study area of this project. Figure modified from Riedel et al. (2013). Centre: The geographical position of the crystallisation ages from this study (blue rectangles) on the map. Red rectangles represent the crystallisation ages reported in Jacobs et al. (1998). The interpreted boundary is based on how far east the typical Maud Belt ages (1100-1000 Ma) has been recorded.

6.3 Late Neoproterozoic igneous activity at ca. 637 and 613 Ma

Two samples within this study gave interpreted igneous crystallisation ages of ca. 613 Ma and ca. 637 Ma. One sample is a mafic metaigneous rock (mafic granulite) with a crystallization age at ca. 613 Ma. The second sample is a metasedimentary rock with a pronounced age peak at ca. 637 Ma, which is interpreted to represent the crystallisation age of the igneous source unit within the sediment source area. Similar igneous ages have previously been reported by Jacobs et al. (1998) within the study area of this project.

Charnockite and anorthosite intrusions gave U/Pb crystallisation ages of ca. 608 Ma and ca. 600 Ma respectively. Furthermore, mafic magmatism with a similar age range has also been reported within the Schirmacher Oasis area north of the present study area (Henjes-Kunst, 2004), within Gjelsvikfjella further west of this study area (Grosch et al., 2007), and in Heimefrontfjella in western DML (Bauer et al., 2003a). The mafic intrusions reported within these studies are characterised by mid-ocean ridge basalt (MORB) rare earth element patterns. Therefore, this study interprets the igneous samples with crystallisation ages of ca. 600 Ma present in this study to be related to an extensional period just prior to the main collision between parts of East and West Gondwana. Thus, the Mozambique Ocean between the Kalahari Craton and the East Antarctic Craton cannot have been fully closed by ca. 600 Ma, as previous models have proposed (e.g. Dalziel, 1997; Gose et al., 1997).

The ca. 600 Ma igneous samples reported within this study, and previously by the mentioned authors, could be related to a back-arc spreading within the Mozambique Ocean just prior to the main collision. The newly discovered TOAST (Jacobs et al., 2015), could represent island arcs that existed in the Mozambique Ocean prior to the collision between the Kalahari Craton and the East Antarctic Craton. Periods of extension in relation to evolving subduction zones could explain magmatism at ca. 600 Ma. This, however, is highly speculative, and beyond the scope of this study.

6.4 Late Neoproterozoic/Early Paleozoic tectono-thermal overprinting

In the timeframe between ca. 1050 Ma and ca. 650 Ma, no evidence of igneous or metamorphic activity is present within the study area. However, all nine samples of this study show clear evidence of metamorphic overprinting related to the "Pan-African" event with Late Neoproterozoic/Early Paleozoic (LN/EP) metamorphism. The interpreted metamorphic ages reported within this study fall between ca. 590–510 Ma. As previously addressed, this age group can be further separated onto two events/episodes. The two groups are interpreted to represent two different metamorphic stages during the "Pan-African" event. The oldest group (marked with yellow in the bottom part of Fig. 6.1) has ages ranging from ca. 590–550 Ma. The younger age group (marked with purple in the bottom part of Fig. 6.1) has ages between ca. 530–510 Ma. One analysed metamorphic zircon grain from sample J1782 gave an age of ca. 611 Ma. This indicates that metamorphism within the Maud Belt could have started prior to ca.

590 Ma. This, however, is based on one single grain analysis, and more analyses will be needed to further support this.

Henjes-Kunst (2004) reported peak metamorphic ages at ca. 620 Ma, reaching granulite facies within the Schirmacher Oasis area, north of the study area of this project. Another aim of this study was to find out whether metamorphic overprinting at ca. 600 Ma is present in the study area of this project. This study revealed very limited evidence to support this. Sample J1782 gave one concordant metamorphic rim analysis at ca. 611 Ma, with a poorly constrained lower intercept (Fig. 5.23). This could, however, indicate that medium to high-grade metamorphism within parts of the Maud Belt might have initiated at an earlier stage than previously assumed.

Comparable LN/EP metamorphic ages have previously been reported by Jacobs et al. (1998). They reported metamorphic U/Pb ages ranging from ca. 600–510 Ma, with two similar metamorphic age groups at ca. 570–550 and ca. 530–515 Ma. In Humbolt Mts. (Wohlthatmassiv), Mikhalsky et al. (1995) reported metamorphic U/Pb ages between ca. 588–512 Ma in felsic gneisses. Furthermore, LN/EP metamorphic overprinting is present throughout Dronning Maud Land, and further east in the Lützow-Holm Complex (LHC) (Henjes-Kunst, 2004; Jacobs et al., 1998; Shiraishi et al., 1994). However, the metamorphic grade varies from west to east. The Maud Belt in western and central Dronning Maud Land is characterised by medium to high-grade metamorphism up to granulite facies (Jacobs et al., 1998) (also this study). SE DML is characterised by the TOAST (ca. 1000–900 Ma), with granulite facies metamorphism towards west, and gradual decrease in metamorphic grade towards east (Jacobs et al., 2015).

6.4.1 Two-stage metamorphic overprinting within Late Neoproterozoic/Early Paleozoic “Pan-African” event

As addressed, the two LN/EP metamorphic age groups could represent two important events during the collision between parts of East and West Gondwana. The oldest group with ages between ca. 590–550 Ma is interpreted to represent the main collisional phase between the Kalahari Craton and the East Antarctic Craton. This event is marked by metamorphic zircon re-crystallisation and granulite facies metamorphism. This interpretation agrees well with the timeframe previously proposed by other authors (e.g. Jacobs et al., 1998; Jacobs et al., 2003*b*).

The youngest age group (Fig. 6.1 (purple)) with ages ranging from ca. 530–510 Ma is interpreted to represent a late stage orogenic event. This event could possibly be linked to partial delamination of the orogenic root, as proposed by Jacobs et al. (2008a). This event is marked by tectonic exhumation and granitic and charnockitic intrusions, that formed because of isothermal decompression. Two samples of this study represent the younger group of this study: J1773 and J1807. J1773 is a garnet-bearing migmatite with euhedral zircon grains, and J1807 is an enderbite (plagioclase-rich endmember of charnockite). Based on these samples, they could have formed as partial melts during delamination and isothermal decompression.

In summary, the "Pan-African" event during the Late Neoproterozioc/Early Paleozoic in Dronning Maud Land, was a long lasting orogenic event spanning more than 150 Ma. The onset of this event is characterised by igneous activity at ca. 639–611 Ma, just prior to the main collision at ca. 590 Ma. The collision between parts of East and West Gondwana can be separated into two main events: The period between ca. 590–550 Ma marks the main continent-continent collision between the East African Craton and the Kalahari Craton, reaching granulite facies metamorphism within the study area. The second metamorphic event between ca. 530–510 Ma may mark the delamination of the orogenic root, resulting in isothermal decompression and partial melting of the basement rocks. This event was followed by orogenic collapse, extension and large-scale granitoid intrusions at ca. 485 Ma (Jacobs et al., 2008a).

The metamorphic U/Pb ages reported in the present study, can further be correlated and compared with reported ages within the Mozambique Belt in East Africa. Similar metamorphic ages have been reported within this region, reaching medium to high-grade metamorphism at ca. 555 Ma near the Lurio Belt in northern Mozambique (Bingen et al., 2009). Muhongo and Lenoir (1994) reported granulite facies metamorphism within the Mozambique belt of Tanzania at ca. 650 Ma. Furthermore, late-tectonic granitoid intrusions present in central DML can be traced northwards into northern Mozambique to the Lurio Belt (Jacobs et al., 2008a). Hence, central Dronning Maud Land evidently represents the southern extent of the Mozambique Belt, as part of the major East African-Antarctic Orogen.

7. Conclusions

Based on the results of this study, I propose the following evolution and implications for the study area within central Dronning Maud Land:

- Late Mesoproterozoic basement crystallisation
  - All basement samples crystallised between ca. 1130–1025 Ma, indicating that these rocks are a part of the Mesoproterozoic Maud Belt.
  - Petrographic characteristics indicate that the basement rocks likely formed within a volcanic arc setting.
  - No Late Mesoproterozoic metamorphic ages were recorded within the study area.
  - No samples within the study area gave ages related to the TOAST (ca. 1000–900 Ma).
  - The boundary between the TOAST and Maud Belt must therefore be further east than previously assumed. However, this boundary could possibly be located very close to the study area.

- No igneous or metamorphic activity is recorded between ca. 1025–637 Ma in the study area

- Late Neoproterozoic tectono-thermal overprinting
  - This event is characterised by early igneous activity at ca. 637–613 Ma, prior to the main collision between the Kalahari Craton and the Maud Belt.
  - Limited evidence point to earliest metamorphism within the study area at ca. 611 Ma.
  - This event is followed by a major Late Neoproterozoic/Early Paleozoic tectono-thermal overprinting in two stages: First stage at ca. 590–550 Ma, and second stage at ca. 530–510 Ma.

8. Future Work

The new results from this study revealed insights into the basement rocks of the Maud Belt in central Dronning Maud Land. However, with the new insight, new questions arise:

Where is the Maud Belt/TOAST boundary in central Dronning Maud Land?
It would be interesting to sample rocks further east of the study area, between Wohlthatmassiv (this study) and Payerfjella (Jacobs et al., 2015). Two main issues might prevent pinpointing the exact boundary, or a transitional zone: (1) The ice-coverage of the area limit the exposed outcrops: (2) The nunakaks exposed in this area might represent post-tectonic granitoid intrusions. Hence, no Mesoproterozoic or Neoproterozoic basement might be present in the exposed nunataks.

The formation and evolution of the Maud Belt
Preforming geochemical (trace element and isotope geochemistry) analyses on the samples of this study could give new insight into the formation of the Maud Belt. Geochemical analysis could reveal whether the basement formed in an island arc setting, in a continental arch setting, or a combination of both. It would also be interesting to compare the geochemical compositions with the TOAST rocks, to understand weather the TOAST has affinities with the Kalahari Craton or the East Antarctic Craton.

Igneous activity at ca. 600 Ma
Geochemical analyses of the mafic igneous samples of this study could reveal the nature of this igneous activity. It would be interesting to know if the igneous activity within the study area is related to back-arc spreading during the closure of the Mozambique Ocean. Trace element analyses of these samples could reveal weather this is a possibility.

References

Adachi, T., Osanai, Y., Hokada, T., Nakano, N., Baba, S., and Toyoshima, T., 2013. Timing of metamorphism in the central Sør Rondane Mountains, eastern Dronning Maud Land, East Antarctica: Constrains from SHRIMP zircon and EPMA monazite dating: Precambrian Res., v. 234, p. 136-160.

Ahrens, L. H., 1955. Implications of the Rhodesia age pattern: Geochimica et Cosmochimica Acta, v. 8, p. 1-15.

Arndt, N. T., Todt, W., Chauvel, C., Tapfer, M., and Weber, K., 1991. U-Pb zircon age and Nd isotopic composition of granitoids, charnockites and supracrustal rocks from Heimefrontfjella, Antarctica: Geologische Rundsch., v. 80, p. 759-777.

Baba, S., Osanai, Y., Nakano, N., Owada, M., Hokada, T., Horie, K., Adachi, T., and Toyoshima, T., 2013. Counterclockwise P–T path and isobaric cooling of metapelites from Brattnipene, Sør Rondane Mountains, East Antarctica: Implications for a tectonothermal event at the proto-Gondwana margin: Precambrian Res., v. 234, p. 210-228.

Barton, J. M., Klemd, R., Allsopp, H. L., Auret, S. H., and Copperthwaite, Y. E., 1987. The geology and geochronology of the Annandagstoppane granite, Western Dronning Maud Land, Antarctica: Contributions to Mineralogy and Petrology, v. 97, p. 488-496.

Bauer, W., Fielitz, W., Jacobs, J., Fanning, C. M., and Spaeth, G., 2003a. Mafic Dykes from Heimefrontfjella and implications for the post-Grenvillian to pre-Pan-African geological evolution of western Dronning Maud Land, Antarctica: Antarctic Science, v. 15, p. 379-391.

Bauer, W., Jacobs, J., Fanning, C. M., and Schmidt, R., 2003b. Late Mesoproterozoic Arc and Back-arc Volcanism in the Heimefrontfjella (East Antarctica) and Implications for the Palaeogeography at the Southeastern Margin of the Kaapvaal-Grunehogna Craton: Gondwana Res., v. 6, p. 449-465.

Bauer, W., Jacobs, J., and Paech, H., 2004. Structural evolution of the metamorphic basement of Central Dronning Maud Land, East Antarctica: Geologisches Jahrbuch Reihe B., v. 96, p. 325.

Becker, T., Schreiber, U., Kampunzu, A. B., and Armstrong, R., 2006. Mesoproterozoic rocks of Namibia and their plate tectonic setting: Journal of African Earth Sciences, v. 46, p. 112-140.

Bell, R., and Jefferson, C., 1987. An hypothesis for an Australian-Canadian connection in the Late Proterozoic and the birth of the Pacific Ocean, *in* Proceedings, Pacific Rim Congress 1987, v. 87, p. 39-50.

Bingen, B., Jacobs, J., Viola, G., Henderson, I. H. C., Skår, Ø., Boyd, R., Thomas, R. J., Solli, A., Key, R. M., and Daudi, E. X. F., 2009. Geochronology of the Precambrian crust in the Mozambique belt in NE Mozambique, and implications for Gondwana assembly: Precambrian Res., v. 170, p. 231-255.

Bisnath, A., Frimmel, H. E., Armstrong, R. A., and Board, W. S., 2006. Tectono-thermal evolution of the Maud Belt: New SHRIMP U–Pb zircon data from Gjelsvikfjella, Dronning Maud Land, East Antarctica: Precambrian Res., v. 150, p. 95-121.

Black, L. P., Kamo, S. L., Allen, C. M., Aleinikoff, J. N., Davis, D. W., Korsch, R. J., and Foudoulis, C., 2003. TEMORA 1: a new zircon standard for Phanerozoic U–Pb geochronology: Chemical Geology, v. 200, p. 155-170.

Blasband, B., White, S., Brooijmans, P., De Boorder, H., and Visser, W., 2000. Late Proterozoic extensional collapse in the Arabian–Nubian shield: Journal of the Geological Society, v. 157, p. 615-628.

Board, W. S., Frimmel, H. E., and Armstrong, R. A., 2005. Pan-African Tectonism in the Western Maud Belt: P–T–t Path for High-grade Gneisses in the H.U. Sverdrupfjella, East Antarctica: Journal of Petrology, v. 46, p. 671-699.

Bormann, P., and Fritzsche, D., 1995. The Schirmacher Oasis, Queen Maud Land, East Antarctica, and its surroundings: Justus Perthes Verlag Gotha: Darmstadt, 488 p.

Burke, K., and Dewey, J., 1972, Orogeny in Africa, Ibadan Nigeria, Geol. Dept., Univ. Ibadan, Orogeny in Africa, 583-608 p.

Cherniak, D. J., and Watson, E. B., 2003. Diffusion in Zircon: Reviews in Mineralogy and Geochemistry, v. 53, p. 113-143.

Claoué-Long, J. C., Compston, W., Roberts, J., and Fanning, C. M., 1995. Two Carboniferous ages: a comparison of SHRIMP zircon dating with conventional zircon ages and 40Ar/39Ar analysis, *In* Berggren, W. A., Kent, D. V., Aubry, M. P., Hardenbol, J. (Eds.), Geochronology Time Scalesand Global Stratigraphic Correlation. SEPM (Society for Sedimentary Geology) Special Publication, p. 2-21.

Collins, A. S., and Pisarevsky, S. A., 2005. Amalgamating eastern Gondwana: the evolution of the Circum-Indian Orogens: Earth-Science Reviews, v. 71, p. 229-270.

Colombo, F., and Talarico, F., 2004. Regional metamorphism in the high-grade basement of central Dronning Maud Land, East Antarctica: Geologisches Jahrbuch Reihe B., v. 96, p. 7.

Condon, D. J., McLean, N., Noble, S. R., and Bowring, S. A., 2010. Isotopic composition (238U/235U) of some commonly used uranium reference materials: Geochimica et Cosmochimica Acta, v. 74, p. 7127-7143.

Corfu, F., Hanchar, J. M., Hoskin, P. W., and Kinny, P., 2003. Atlas of zircon textures: Reviews in mineralogy and geochemistry, v. 53, p. 469-500.

Dalziel, I. W. D., 1991. Pacific margins of Laurentia and East Antarctica-Australia as a conjugate rift pair: Evidence and implications for an Eocambrian supercontinent: Geology, v. 19, p. 598-601.

Dalziel, I. W. D., 1997. OVERVIEW: Neoproterozoic-Paleozoic geography and tectonics: Review, hypothesis, environmental speculation: Geological Society of America Bulletin, v. 109, p. 16-42.

Dalziel, I. W. D., 2013. Antarctica and supercontinental evolution: clues and puzzles: Earth and Environmental Science Transactions of the Royal Society of Edinburgh, v. 104, p. 3-16.

Dodson, M. H., 1978. A linear method for second-degree interpolation in cyclical data collection: Journal of Physics E: Scientific Instruments, v. 11, p. 296.

Eby, G. N., 1992. Chemical subdivision of the A-type granitoids: Petrogenetic and tectonic implications: Geology, v. 20, p. 641-644.

Eisbacher, G., 1985. Late Proterozoic rifting, glacial sedimentation, and sedimentary cycles in the light of Windermere deposition, western Canada: Palaeogeography, Palaeoclimatology, Palaeoecology, v. 51, p. 231-254.

Elburg, M., Jacobs, J., Andersen, T., Clark, C., Läufer, A., Ruppel, A., Krohne, N., and Damaske, D., 2015. Early Neoproterozoic metagabbro-tonalite-trondhjemite of Sør Rondane (East Antarctica): Implications for supercontinent assembly: Precambrian Res., v. 259, p. 189-206.

Engvik, A. K., and Elvevold, S., 2004. Pan-African extension and near-isothermal exhumation of a granulite facies terrain, Dronning Maud Land, Antarctica: Geological Magazine, v. 141, p. 649-660.

Fitzsimons, I., 2000a. Grenville-age basement provinces in East Antarctica: evidence for three separate collisional orogens: Geology, v. 28, p. 879-882.

Fitzsimons, I. C. W., 2000b. A review of tectonic events in the East Antarctic Shield and their implications for Gondwana and earlier supercontinents: Journal of African Earth Sciences, v. 31, p. 3-23.

Fitzsimons, I. C. W., 2003. Proterozoic basement provinces of southern and southwestern Australia, and their correlation with Antarctica: Geological Society, London, Special Publications, v. 206, p. 93-130.

Frimmel, H. E., 2004. Formation of a late Mesoproterozoic supercontinent: the South Africa–East Antarctica connection: The Precambrian Earth: Tempos and Events. Developments in Precambrian Geology, v. 12, p. 240-255.

Golynsky, A., and Jacobs, J., 2001. Grenville Age versus Pan African Magnetic Anomaly Imprints in Western Dronning Maud Land, East Antarctica: The Journal of Geology, v. 109, p. 136-142.

Goodge, J. W., Vervoort, J. D., Fanning, C. M., Brecke, D. M., Farmer, G. L., Williams, I. S., Myrow, P. M., and DePaolo, D. J., 2008. A Positive Test of East Antarctica–Laurentia Juxtaposition Within the Rodinia Supercontinent: Science, v. 321, p. 235-240.

Goodge, J. W., Fanning, C. M., Brecke, D. M., Licht, K. J., and Palmer, E. F., 2010. Continuation of the Laurentian Grenville Province across the Ross Sea Margin of East Antarctica: The Journal of Geology, v. 118, p. 601-619.

Gose, W. A., Helper, M. A., Connelly, J. N., Hutson, F. E., and Dalziel, I. W., 1997. Paleomagnetic data and U-Pb isotopic age determinations from Coats Land, Antarctica: Implications for late Proterozoic plate reconstructions: Journal of Geophysical Research: Solid Earth, v. 102, p. 7887-7902.

Grantham, G. H., Jackson, C., Moyes, A. B., Groenewald, P. B., Harris, P. D., Ferrar, G., and Krynauw, J. R., 1995. The tectonothermal evolution of the Kirwanveggen—H.U. Sverdrupfjella areas, Dronning Maud Land, Antarctica: Precambrian Res., v. 75, p. 209-229.

Grantham, G. H., Macey, P. H., Ingram, B. A., Roberts, M. P., Armstrong, R. A., Hokada, T., Shiraishi, K., Jackson, C., Bisnath, A., and Manhica, V., 2008. Terrane correlation between Antarctica, Mozambique and Sri Lanka; comparisons of geochronology, lithology, structure and metamorphism and possible implications for the geology of southern Africa and Antarctica: Geological Society, London, Special Publications, v. 308, p. 91-119.

Groenewald, P. B., Grantham, G. H., and Watkeys, M. K., 1991. Geological evidence for a Proterozoic to Mesozoic link between southeastern Africa and Dronning Maud Land, Antarctica: Journal of the Geological Society, v. 148, p. 1115-1123.

Groenewald, P. B., Moyes, A. B., Grantham, G. H., and Krynauw, J. R., 1995. East Antarctic crustal evolution: geological constraints and modelling in western Dronning Maud Land: Precambrian Res., v. 75, p. 231-250.

Grosch, E. G., Bisnath, A., Frimmel, H. E., and Board, W. S., 2007. Geochemistry and tectonic setting of mafic rocks in western Dronning Maud Land, East Antarctica: implications for the geodynamic evolution of the Proterozoic Maud Belt: Journal of the Geological Society, v. 164, p. 465-475.

Hanson, R. E., Martin, M. W., Bowring, S. A., and Munyanyiwa, H., 1998. U-Pb zircon age for the Umkondo dolerites, eastern Zimbabwe: 1.1 Ga large igneous province in southern Africa–East Antarctica and possible Rodinia correlations: Geology, v. 26, p. 1143-1146.

Harley, S. L., and Kelly, N. M., 2007. Zircon Tiny but Timely: Elements, v. 3, p. 13-18.

Harris, P., Moyes, A., Fanning, C., and Armstrong, R., 1995. Zircon ion microprobe results from the Maudheim high-grade gneiss terrane, western Dronning Maud Land, Antarctica: Centennial Geocongress, p. 3-7.

Henjes-Kunst, F., 2004. Further evidence for Pan-African polyphase magmatism and metamorphism in central Dronning Maud Land, East Antarctica, from rocks at Schirmacheroase: A geochronological study: Geologisches Jahrbuch Reihe B., v. 96, p. 255.

Hoffman, P. F., 1991. Did the Breakout of Laurentia Turn Gondwanaland Inside-Out?: Science, v. 252, p. 1409-1412.

Hoffman, P., 1992. Global Grenvillian kinematics and assembly of the Neoproterozoic supercontinent Rodinia, *in* Proceedings Geol Assoc Canada, Annual Meeting, Wolfville 1992.

Hoskin, P. W. O., and Schaltegger, U., 2003. The Composition of Zircon and Igneous and Metamorphic Petrogenesis: Reviews in Mineralogy and Geochemistry, v. 53, p. 27-62.

Ikeda, Y., and Shiraishi, K., 1998. Petrogenesis of the tonalitic rocks from the Sør Rondane Mountains, East Antarctica: Polar geoscience, v. 11, p. 143-153.

Jackson, C., 1999. Characterization of Mesoproterozoic to Palaeozoic crustal evolution of Western Dronning Maud Land: Unpublished report to South African National Antarctic Program Study, v. 534, p. 80.

Jacobs, J., Thomas, R. J., and Weber, K., 1993. Accretion and indentation tectonics at the southern edge of the Kaapvaal craton during the Kibaran (Grenville) orogeny: Geology, v. 21, p. 203-206.

Jacobs, J., Bauer, W., Spaeth, G., Thomas, R. J., and Weber, K., 1996. Lithology and structure of the Grenville-aged (~1.1 Ga) basement of Heimefrontfjella (East Antarctica): Geologische Rundschau, v. 85, p. 800-821.

Jacobs, J., Falter, M., Weber, K., and Jeßberger, E., 1997. 40Ar-39Ar evidence for the structural evolution of the Heimefront Shear Zone (Western Dronning Maud Land), East Antarctica: The Antarctic Region: Geological Evolution and Processes. Terra Antartica Publication, Siena, p. 37-44.

Jacobs, J., Fanning, C. M., Henjes-Kunst, F., Olesch, M., and Paech, H.-J., 1998. Continuation of the Mozambique Belt Into East Antarctica: Grenville Age Metamorphism and Polyphase Pan-African High Grade Events in Central Dronning Maud Land: The Journal of Geology, v. 106, p. 385-406.

Jacobs, J., Hansen, B., Henjes-Kunst, F., Thomas, R., Weber, K., Bauer, W., Armstrong, R., and Cornell, D., 1999. New age constraints on the Proterozoic/Lower Palaeozoic evolution of Heimefrontfjella, East Antarctica, and its bearing on Rodinia/Gondwana correlations: Terra Antartica, v. 6, p. 377-389.

Jacobs, J., and Thomas, R. J., 2002. The Mozambique belt from an East Antarctic perspective, *in* Proceedings Antarctica at the close of a millennium. Proceedings of the 8th International Symposium on Antarctic Earth Sciences: Royal Society of New Zealand Bulletin 2002, v. 35, p. 3-18.

Jacobs, J., Bauer, W., and Fanning, C. M., 2003*a*. Late Neoproterozoic/Early Palaeozoic events in central Dronning Maud Land and significance for the southern extension of the East African Orogen into East Antarctica: Precambrian Res., v. 126, p. 27-53.

Jacobs, J., Klemd, R., Fanning, C. M., Bauer, W., and Colombo, F., 2003*b*. Extensional collapse of the late Neoproterozoic-early Palaeozoic East African-Antarctic Orogen in central Dronning Maud Land, East Antarctica: Geological Society, London, Special Publications, v. 206, p. 271-287.

Jacobs, J., and Thomas, R. J., 2004. Himalayan-type indenter-escape tectonics model for the southern part of the late Neoproterozoic–early Paleozoic East African–Antarctic orogen: Geology, v. 32, p. 721-724.

Jacobs, J., Bingen, B., Thomas, R. J., Bauer, W., Wingate, M. T. D., and Feitio, P., 2008a. Early Palaeozoic orogenic collapse and voluminous late-tectonic magmatism in Dronning Maud Land and Mozambique: insights into the partially delaminated orogenic root of the East African–Antarctic Orogen?: Geological Society, London, Special Publications, v. 308, p. 69-90.

Jacobs, J., Pisarevsky, S., Thomas, R. J., and Becker, T., 2008b. The Kalahari Craton during the assembly and dispersal of Rodinia: Precambrian Res., v. 160, p. 142-158.

Jacobs, J., Elburg, M., Läufer, A., Kleinhanns, I. C., Henjes-Kunst, F., Estrada, S., Ruppel, A. S., Damaske, D., Montero, P., and Bea, F., 2015. Two distinct Late Mesoproterozoic/Early Neoproterozoic basement provinces in central/eastern Dronning Maud Land, East Antarctica: The missing link, 15–21° E: Precambrian Res., v. 265, p. 249-272.

Jones, D., Bates, M., Li, Z., Corner, B., and Hodgkinson, G., 2003. Palaeomagnetic results from the ca. 1130 Ma Borgmassivet intrusions in the Ahlmannryggen region of Dronning Maud Land, Antarctica, and tectonic implications: Tectonophysics, v. 375, p. 247-260.

Joshi, A., Pant, N., and Parimoo, M., 1991. Granites of Petermann Ranges, East Antarctica and implications on their genesis: Geological Society of India, v. 38, p. 169-181.

Kamei, A., Horie, K., Owada, M., Yuhara, M., Nakano, N., Osanai, Y., Adachi, T., Hara, Y., Terao, M., Teuchi, S., Shimura, T., Tsukada, K., Hokada, T., Iwata, C., Shiraishi, K., Ishizuka, H., and Takahashi, Y., 2013. Late Proterozoic juvenile arc metatonalite and adakitic intrusions in the Sør Rondane Mountains, eastern Dronning Maud Land, Antarctica: Precambrian Res., v. 234, p. 47-62.

Kamenev, E. N., Kamenev, A. G. I., and Kovach, V. P., 1990. Zemlya Korolevy Maud, *In* Ivanov, V. L., and Kamenev, E. N., eds.,: Geologiya i Mineralnye Resursy Antarktidy: Moskva, p. 113–147.

Kaul, M., Singh, R., Srivastava, D., Jayaram, S., and Mukerji, S., 1991. Petrographic and structural characteristics of a part of the East Antarctic Craton, Queen Maud Land, Antarctica: Geological Evolution of Antarctica, p. 89-94.

Kennedy, W., 1964. The structural differentiation of Africa in the Pan-African (±500 my) tectonic episode: Leeds Univ. Res. Inst. Afr. Geol. Annu. Rep, v. 8, p. 48-49.

Kröner, A., 1984. Late Precambrian plate tectonics and orogeny: a need to redefine the term Pan-African: African geology, v. 5, p. 23-28.

Kröner, A., and Stern, R., 2004. Africa: Pan-African orogeny: Encyclopedia of Geology. Elsevier, p. 1-12.

Ksienzyk, A. K., and Jacobs, J., 2015. Western Australia-Kalahari (WAlahari) connection in Rodinia: Not supported by U/Pb detrital zircon data from the Maud Belt (East Antarctica) and the Northampton Complex (Western Australia): Precambrian Res., v. 259, p. 207-221.

Li, Z.-X., Zhang, L., and Powell, C. M., 1995. South China in Rodinia: Part of the missing link between Australia–East Antarctica and Laurentia?: Geology, v. 23, p. 407-410.

Li, Z. X., Bogdanova, S. V., Collins, A. S., Davidson, A., De Waele, B., Ernst, R. E., Fitzsimons, I. C. W., Fuck, R. A., Gladkochub, D. P., Jacobs, J., Karlstrom, K. E., Lu, S., Natapov, L. M., Pease, V., Pisarevsky, S. A., Thrane, K., and Vernikovsky, V., 2008. Assembly, configuration, and break-up history of Rodinia: A synthesis: Precambrian Res., v. 160, p. 179-210.

Loewy, S. L., Dalziel, I. W. D., Pisarevsky, S., Connelly, J. N., Tait, J., Hanson, R. E., and Bullen, D., 2011. Coats Land crustal block, East Antarctica: A tectonic tracer for Laurentia?: Geology, v. 39, p. 859-862.

Ludwig, K. R., 2012. User's manual for Isoplot 3.75 – A geochronological toolkit for Microsoft Excel: Berkeley Geochronology Center Special Publications, v. 5, p. 75.

Marschall, H. R., Hawkesworth, C. J., and Leat, P. T., 2013. Mesoproterozoic subduction under the eastern edge of the Kalahari-Grunehogna Craton preceding Rodinia assembly: The Ritscherflya detrital zircon record, Ahlmannryggen (Dronning Maud Land, Antarctica): Precambrian Res., v. 236, p. 31-45.

Meert, J. G., van der Voo, R., and Ayub, S., 1995. Paleomagnetic investigation of the Neoproterozoic Gagwe lavas and Mbozi complex, Tanzania and the assembly of Gondwana: Precambrian Res., v. 74, p. 225-244.

Meert, J. G., and Van Der Voo, R., 1997. The assembly of Gondwana 800-550 Ma: Journal of Geodynamics, v. 23, p. 223-235.

Meert, J. G., 2003. A synopsis of events related to the assembly of eastern Gondwana: Tectonophysics, v. 362, p. 1-40.

Mendonidis, P., Thomas, R. J., Grantham, G. H., and Armstrong, R. A., 2015. Geochronology of emplacement and charnockite formation of the Margate Granite Suite, Natal Metamorphic Province, South Africa: Implications for Natal-Maud belt correlations: Precambrian Res., v. 265, p. 189-202.

Mieth, M., Jacobs, J., Ruppel, A., Damaske, D., Läufer, A., and Jokat, W., 2014. New detailed aeromagnetic and geological data of eastern Dronning Maud Land: Implications for refining the tectonic and structural framework of Sør Rondane, East Antarctica: Precambrian Res., v. 245, p. 174-185.

Mikhalsky, E., Beliatsky, B., Savva, E., Federov, L., and Hahne, K., 1995. Isotopic systematics and evolution of metamorphic rocks from the northern Humboldt Mountains (the Queen Maud Land, East Antarctica), *in* Proceedings of the VII International Symposium on Antarctic Earth Sciences 1995, p. 270.

Moores, E. M., 1991. Southwest U.S.-East Antarctic (SWEAT) connection: A hypothesis: Geology, v. 19, p. 425-428.

Muhongo, S., and Lenoir, J.-L., 1994. Pan-African granulite-facies metamorphism in the Mozambique Belt of Tanzania: U-Pb zircon geochronology: Journal of the Geological Society, v. 151, p. 343-347.

Möller, A., O'Brien, P. J., Kennedy, A., and Kröner, A., 2003. Linking growth episodes of zircon and metamorphic textures to zircon chemistry: an example from the ultrahigh-temperature granulites of Rogaland (SW Norway): Geological Society, London, Special Publications, v. 220, p. 65-81.

Osanai, Y., Nogi, Y., Baba, S., Nakano, N., Adachi, T., Hokada, T., Toyoshima, T., Owada, M., Satish-Kumar, M., Kamei, A., and Kitano, I., 2013. Geologic evolution of the Sør Rondane Mountains, East Antarctica: Collision tectonics proposed based on metamorphic processes and magnetic anomalies: Precambrian Res., v. 234, p. 8-29.

Paulsson, O., and Austrheim, H., 2003. A geochronological and geochemical study of rocks from Gjelsvikfjella, Dronning Maud Land, Antarctica—implications for Mesoproterozoic correlations and assembly of Gondwana: Precambrian Res., v. 125, p. 113-138.

Peters, M., Haverkamp, B., Emmermann, R., Kohnen, H., and Weber, K., 1991. Palaeomagnetism, K-Ar dating and geodynamic setting of igneous rocks in

western and central Neuschwabenland, Antarctica, *in* Geological evolution of Antarctica, Cambridge Univ. Press, p. 549-555.

Pierce, E. L., Hemming, S. R., Williams, T., van de Flierdt, T., Thomson, S. N., Reiners, P. W., Gehrels, G. E., Brachfeld, S. A., and Goldstein, S. L., 2014. A comparison of detrital U–Pb zircon, 40Ar/39Ar hornblende, 40Ar/39Ar biotite ages in marine sediments off East Antarctica: Implications for the geology of subglacial terrains and provenance studies: Earth-Science Reviews, v. 138, p. 156-178.

Pisarevsky, S. A., Wingate, M. T., Powell, C. M., Johnson, S., and Evans, D. A., 2003. Models of Rodinia assembly and fragmentation: Geological Society, London, Special Publications, v. 206, p. 35-55.

Powell, C. M., Jones, D., Pisarevsky, S., and Wingate, M., 2001a. Palaeomagnetic constraints on the position of the Kalahari craton in Rodinia: Precambrian Res., v. 110, p. 33-46.

Powell, C. M., Pisarevsky, S., and Wingate, M. T., 2001b. A new shape for Rodinia: Gondwana Res., v. 4, p. 736-737.

Powell, C. M., and Pisarevsky, S., 2002. Late Neoproterozoic assembly of east Gondwana: Geology, v. 30, p. 3-6.

Que, M., and Allen, A. R., 1996. Sericitization of plagioclase in the Rosses granite complex, Co. Donegal, Ireland: Mineralogical Magazine, v. 60, p. 927-936.

Ravich, M. G., and Solov' ev, D. S., 1966. Geologiya i petrologiya tsentral'noy chasti gor zemli Korelevy Mod (Geology and petrology of the central Dronning Maud Land): Nedra, Leningrad, 298 p.

Ravich, M. G., and Kamenev, E. N., 1972. Kristallicheskiy fundament arkticheskoj plartformy: Leningrad, Gidrometeoizdat, 658 p. (English ed., Crystalline basement of the Antarctic platform: Jerusalem, 1975, 574 p.).

Riedel, S., Jacobs, J., and Jokat, W., 2013. Interpretation of new regional aeromagnetic data over Dronning Maud Land (East Antarctica): Tectonophysics, v. 585, p. 161-171.

Roland, N. W., 2004*a*. Pan-African granites in central Dronning Maud Land, East Antarctica: Product of collision or intra-plate event?: Zeitschrift der Deutschen Geologischen Gesellschaft, p. 469-479.

Roland, N., 2004*b*. Pan-African granite-charnockite magmatism in central Dronning Maud Land, East Antarctica: petrography, geochemistry and plate tectonic implications: Geologisches Jahrbuch Reihe B, v. 96, p. 187.

Ruppel, A. S., Läufer, A., Jacobs, J., Elburg, M., Krohne, N., Damaske, D., and Lisker, F., 2015. The Main Shear Zone in Sør Rondane, East Antarctica: Implications for the late-Pan-African tectonic evolution of Dronning Maud Land: Tectonics, v. 34, p. 1290-1305.

Shackleton, R. M., 1996. The final collision zone between East and West Gondwana: where is it?: Journal of African Earth Sciences, v. 23, p. 271-287.

Shelley, D., 1993. Igneous and metamorphic rocks under the microscope: classification, textures, microstructures and mineral preferred orientation, Elsevier, v. 20, 446 p.

Shiraishi, K., Ellis, D. J., Hiroi, Y., Fanning, C. M., Motoyoshi, Y., and Nakai, Y., 1994. Cambrian Orogenic Belt in East Antarctica and Sri Lanka: Implications for Gondwana Assembly: The Journal of Geology, v. 102, p. 47-65.

Shiraishi, K., Dunkley, D. J., Hokada, T., Fanning, C. M., Kagami, H., and Hamamoto, T., 2008. Geochronological constraints on the Late Proterozoic to Cambrian crustal evolution of eastern Dronning Maud Land, East Antarctica: a synthesis of SHRIMP U-Pb age and Nd model age data: Geological Society, London, Special Publications, v. 308, p. 21-67.

Stern, R. J., 1994, ARC Assembly and Continental Collision in the Neoproterozoic East African Orogen: Implications for the Consolidation of Gondwanaland: Annual Review of Earth and Planetary Sciences, v. 22, no. 1, p. 319-351.

Stern, R., 1997. The GSC sensitive high resolution ion microprobe (SHRIMP): analytical techniques of zircon U–Th–Pb age determinations and performance evaluation: Geological Survey of Canada, Current Research, p. 1-31.

Takahashi, Y., Arakawa, Y., Sakiyama, T., Osanai, Y., and Makimoto, H., 1990. Rb-Sr and K-Ar whole rock ages of the plutonic bodies from the Sor Rondane Mountains, East Antarctica, *in* Proceedings of the NIPR symposium on Antarctic Geosciences 1990, v. 4, p. 1-8.

Tera, F., and Wasserburg, G. J., 1972. U-Th-Pb systematics in three Apollo 14 basalts and the problem of initial Pb in lunar rocks: Earth and Planetary Science Letters, v. 14, p. 281-304.

Thomas, R., Agenbacht, A., Cornell, D., and Moore, J., 1994. The Kibaran of southern Africa: tectonic evolution and metallogeny: Ore Geology Reviews, v. 9, p. 131-160.

Valentine, J. W., and Moores, E. M., 1970. Plate-tectonic Regulation of Faunal Diversity and Sea Level: a Model: Nature, v. 228, p. 657-659.

Viola, G., Henderson, I., Bingen, B., Thomas, R., Smethurst, M., and De Azavedo, S., 2008. Growth and collapse of a deeply eroded orogen: Insights from structural, geophysical, and geochronological constraints on the Pan-African evolution of NE Mozambique: Tectonics, v. 27, no. 5.

Wetherill, G. W., 1956. Discordant uranium-lead ages, I: EOS, Transactions American Geophysical Union, v. 37, no. 3, p. 320-326.

Williams, I. S., and Claesson, S., 1987. Isotopic evidence for the Precambrian provenance and Caledonian metamorphism of high grade paragneisses from the Seve Nappes, Scandinavian Caledonides: Contributions to Mineralogy and Petrology, v. 97, p. 205-217.

Williams, I. S., 1998. U-Th-Pb Geochronology by Ion Microprobe. In McKibben, M. A., Shanks III, W. C., and Ridley, W. I. (eds.): Applications of microanalytical techniques to understanding mineralizing processes. Reviews in Economic Geology v.7. p. 1-35.

Williams, I. S., and Hergt, J., 2000. U–Pb dating of Tasmanian dolerites: a cautionary tale of SHRIMP analysis of high-U zircon: Beyond, p. 185-188.

Online recourses:

NPI, 2017: http://www.npolar.no/en/services/maps/printed/topographic-antarctica.html (Downloaded: 10.05.2017)

Appendix

Table 1 U-Pb SHRIMP zircon data J1672

									Radiogenic (corrected) ratio[3]					Calculated ages	
Sample ID	**Grain characteristics in CL[1]**	**Comment**	**U (ppm)**	**Th (ppm)**	**206Pb (ppm)**	**Th/U**	**f206_4[2]**	**% discord.**	**206Pb/238U**	**±err**	**207Pb/235U**	**±err**	**rho**	**206Pb/238U**	**±err**
J1672-1.1	CL-B-core-Z	concordant	166	53	26	0.33	0.09	-0.6	0.18478	0.00203	1.91830	0.02716	0.559	1093.1	11.1
J1672-10.1	CL-M-core-Z	concordant	246	93	39	0.39	0.05	0.4	0.18242	0.00346	1.90986	0.03854	0.676	1080.2	18.9
J1672-11.1	CL-M-core-Z	Pb-loss	798	507	114	0.65	0.05	3.4	0.16507	0.00617	1.72984	0.06534	0.713	984.9	34.2
J1672-12.1	CL-M-rim-Z	concordant (young)	271	1	21	0.00	0.09	1.6	0.08949	0.00113	0.73818	0.01158	0.580	552.5	6.7
J1672-13.1	CL-B-core-Z	concordant	139	47	22	0.34	0.12	1.2	0.18061	0.00226	1.90497	0.02940	0.583	1070.3	12.3
J1672-14.1	CL-D-core-single phase	Pb-loss	486	126	74	0.27	**[0,19]**	5.4	0.17555	0.00302	1.96017	0.03840	0.632	1042.6	16.6
J1672-14.2	CL-M-core-Z	concordant	430	108	65	0.26	0.09	3.2	0.17552	0.00564	1.88870	0.06374	0.685	1042.4	30.9
J1672-15.1	CL-M-core-Z	concordant	501	146	79	0.30	0.03	0.4	0.18209	0.00263	1.90601	0.02877	0.690	1078.4	14.4
J1672-16.1	CL-M-core-Z	concordant	371	231	58	0.64	0.03	0.4	0.18189	0.00293	1.90086	0.03234	0.682	1077.3	16.0
J1672-17.1	CL-M-core-Z	concordant	439	184	69	0.43	0.02	0.2	0.18088	0.00299	1.87669	0.03226	0.693	1071.8	16.4
J1672-18.1	CL-B-core-Z	concordant	129	44	21	0.35	0.10	0.6	0.18575	0.00337	1.96998	0.03875	0.663	1098.3	18.3
J1672-19.1	CL-B-core-Z	concordant	121	38	19	0.32	0.13	-0.2	0.18361	0.00362	1.91302	0.04481	0.605	1086.7	19.8
J1672-2.1	CL-M-core-Z	concordant	313	59	50	0.19	0.06	0.4	0.18542	0.00177	1.96019	0.02128	0.635	1096.5	9.7
J1672-20.1	CL-M-core-Z	concordant	372	198	59	0.54	0.02	0.2	0.18355	0.00246	1.92106	0.02697	0.687	1086.3	13.4
J1672-21.1	CL-B-core-Z	concordant	275	85	44	0.32	0.04	0.2	0.18324	0.00199	1.91901	0.02360	0.636	1084.6	10.8
J1672-22.1	CL-M-core-Z	concordant	473	236	75	0.51	0.03	-0.2	0.18257	0.00211	1.89383	0.02305	0.684	1081.0	11.5
J1672-23.1	CL-B-core-Z	concordant	106	36	17	0.35	0.10	0.0	0.18676	0.00350	1.96639	0.03907	0.680	1103.8	19.1
J1672-24.1	CL-M-core-SZ	Ancient Pb-loss	409	134	49	0.34	0.03	4.0	0.13923	0.00198	1.36635	0.02054	0.681	840.3	11.2
J1672-25.1	CL-D-rim-UZ	Concordant (young)	512	8	41	0.02	0.10	3.2	0.09309	0.00377	0.79220	0.03347	0.690	573.8	22.3
J1672-3.1	CL-B-core-Z	concordant	127	49	20	0.39	0.08	1.2	0.18377	0.00273	1.95536	0.03449	0.607	1087.5	14.9
J1672-4.1	CL-M-core-single phase	concordant	275	78	43	0.29	0.06	1.8	0.17931	0.00221	1.90740	0.02540	0.665	1063.2	12.1
J1672-5.1	CL-M-core-single phase	concordant	561	183	92	0.34	0.02	-1.0	0.18985	0.00198	1.98485	0.02492	0.598	1120.6	10.8
J1672-6.1	CL-D-rim-UZ	concordant (young)	1966	12	153	0.01	0.02	0.6	0.08993	0.00153	0.73363	0.01277	0.702	555.1	9.0
J1672-7.1	CL-B-core-Z	concordant	157	61	25	0.40	0.10	0.8	0.18264	0.00219	1.92489	0.02762	0.602	1081.4	12.0
J1672-8.1	CL-B-core-Z	concordant	154	64	24	0.43	0.04	1.2	0.18256	0.00245	1.93442	0.02758	0.678	1080.9	13.3
J1672-9.1	CL-D-core-Z	concordant	467	165	73	0.36	0.10	1.8	0.18134	0.00295	1.93524	0.03580	0.634	1074.3	16.2

(1) CL-B/M/D = bright/medium/dark; Z = zoned, UZ = unzoned, SZ = sector zoned

(2) f206_4 is the percentage of common Pb estimated from the 204 counts. In bulb and paranthesis where they have been corrected for

(3) Ratios after correction. Yellow are corrected with 204 corrected ratios

Grey analyses are excluded due to age error > 5% at 2 σ

Table 2 U-Pb SHRIMP zircon data J1734

									Radiogenic (corrected) ratio[3]					Calculated ages	
Sample ID	**Grain characteristics in CL[1]**	**Comment**	**U (ppm)**	**Th (ppm)**	**206Pb (ppm)**	**Th/U**	**f206_4[2]**	**% discord.**	**206Pb/238U**	**±err**	**207Pb/235U**	**±err**	**rho**	**206Pb/238U**	**±err**
J1734-1.1	CL-D-core-Z	Pb-loss	977	204	142	0.21	0.1	2.6	0.16807	0.00270	1.74998	0.03542	0.572	1082.3	24.4
J1734-10.1	CL-D-core-Z	concordant	615	89	99	0.15	0.1	1.0	0.18575	0.00310	1.98133	0.03695	0.644	1130.5	16.6
J1734-11.1	CL-M-core-Z	concordant	398	114	63	0.29	0.1	0.6	0.18353	0.00221	1.93322	0.02679	0.626	1105.5	13.6
J1734-12.1	CL-D-core-Z	concordant	594	209	96	0.36	0.0	0.6	0.18579	0.00115	1.96757	0.01842	0.478	1116.3	13.8
J1734-13.1	CL-M-core-Z	concordant	601	201	96	0.34	**[0.2]**	1.4	0.18314	0.00164	1.95483	0.02159	0.584	1084.1	8.9
J1734-14.1	CL-M-core-Z	Pb-loss	1368	288	161	0.22	0.1	8.4	0.13634	0.00102	1.42724	0.01435	0.534	1093.1	13.4
J1734-15.1	CL-M-core-Z	Pb-loss	526	222	82	0.43	0.1	0.4	0.17995	0.00199	1.87208	0.02554	0.585	1080.5	15.8
J1734-16.1	CL-D-core-Z	Pb-loss	962	62	144	0.07	0.0	3.6	0.17237	0.00270	1.85170	0.03050	0.684	1144.7	10.2
J1734-17.1	CL-D-rim-UZ	concordant (young)	629	4	47	0.01	0.1	1.4	0.08716	0.00075	0.71332	0.00761	0.584	580.3	13.4
J1734-18.1	CL-M-core-Z	concordant	970	223	153	0.24	0.0	0.8	0.18258	0.00182	1.92687	0.02033	0.678	1109.3	7.0
J1734-19.1	CL-M-core-Z	concordant	688	204	111	0.30	0.0	0.8	0.18715	0.00219	1.99496	0.02436	0.691	1129.1	6.8
J1734-2.1	CL-D-core-Z	Pb-loss	2207	105	325	0.05	0.0	1.6	0.17022	0.00232	1.75666	0.02428	0.711	1064.3	4.4
J1734-20.1	CL-M-core-Z	Pb-loss	529	112	82	0.22	0.1	0.0	0.17981	0.00218	1.85543	0.02593	0.625	1064.1	14.0
J1734-21.1	CL-M-core-Z	concordant	570	126	93	0.23	0.0	0.8	0.18796	0.00233	2.00887	0.03288	0.545	1134.5	21.2
J1734-22.1	CL-M-core-Z	concordant	447	257	71	0.59	0.1	2.0	0.18351	0.00227	1.97641	0.02518	0.698	1149.7	6.2
J1734-23.1	CL-M-core-Z	Pb-loss	469	150	77	0.33	0.1	1.8	0.18987	0.00259	2.07894	0.02907	0.703	1182.5	6.0
J1734-3.1	CL-M-core-Z	concordant	900	167	143	0.19	0.0	1.0	0.18379	0.00331	1.94808	0.04609	0.547	1117.9	30.4
J1734-4.1	CL-M-core-Z	concordant	1307	34	202	0.03	0.0	1.8	0.17890	0.00197	1.89907	0.02519	0.598	1120.9	14.6
J1734-5.1	CL-M-core-Z	Pb-loss	434	89	66	0.21	0.1	2.8	0.17676	0.00388	1.89542	0.05227	0.574	1141.1	32.8
J1734-6.1	CL-M-core-Z	Pb-loss	591	58	90	0.10	0.0	2.0	0.17532	0.00588	1.84825	0.06623	0.674	1107.1	24.8
J1734-7.1	CL-M-core-Z	concordant	621	202	99	0.33	0.1	1.8	0.18417	0.00216	1.98392	0.02479	0.677	1150.1	8.4
J1734-8.1	CL-M-core-Z	concordant	337	285	55	0.87	0.1	0.6	0.18847	0.00436	2.01312	0.04684	0.715	1133.3	5.2
J1734-9.1	CL-D-core-Z	concordant	1092	238	176	0.22	0.0	0.8	0.18656	0.00233	1.99153	0.02573	0.696	1132.1	6.6

(1) CL-B/M/D = bright/medium/dark; Z = zoned, UZ = unzoned, SZ = sector zoned

(2) f206_4 is the percentage of common Pb estimated from the 204 counts. In bulb and paranthesis where they have been corrected for

(3) Ratios after correction. Yellow are corrected with 204 corrected ratios

Grey analyses are excluded due to age error > 5% at 2 σ

Table 3 U-Pb SHRIMP zircon data J1738

									Radiogenic (corrected) ratio[3]					Calculated ages	
Sample ID	**Grain characteristics in CL[1]**	**Comment**	**U (ppm)**	**Th (ppm)**	**206Pb (ppm)**	**Th/U**	**f206_4[2]**	**% discord.**	**206Pb/238U**	**±err**	**207Pb/235U**	**±err**	**rho**	**206Pb/238U**	**±err**
J1738-1.1	CL-M-core-Z	Pb-loss (recent)	390	115	60	0.30	0.0	1.0	0.17953	0.00250	1.88576	0.03166	0.598	1064.0	13.7
J1738-10.1	CL-D-core-Z	Pb-loss (recent)	571	114	89	0.21	0.0	0.2	0.18035	0.00506	1.87284	0.05444	0.696	1068.6	27.7
J1738-11.1	CL-M-core-Z	Pb-loss (recent)	623	119	91	0.20	0.0	2.0	0.16890	0.00172	1.74853	0.01896	0.677	1005.6	9.5
J1738-12.1	CL-M-core-Z	concordant	8	26	15	0.30	0.1	-0.8	0.19717	0.00527	2.10757	0.07980	0.508	1159.3	28.4
J1738-13.1	CL-M-core-Z	concordant	236	124	38	0.54	0.1	0.6	0.18564	0.00143	1.96638	0.01950	0.558	1096.8	7.8
J1738-14.1	CL-B-core-Z	Pb-loss (recent)	340	119	47	0.36	**[0.2]**	5.8	0.15826	0.00185	1.68950	0.02239	0.635	947.1	10.3
J1738-15.1	CL-B-core-Z	Pb-loss (recent)	125	56	18	0.46	**[0.2]**	0.8	0.16255	0.00313	1.62133	0.03613	0.623	971.0	17.5
J1738-16.1	CL-M-core-Z	concordant	171	53	28	0.32	0.1	0.2	0.18930	0.00332	2.00977	0.03932	0.645	1116.9	18.0
J1738-17.1	CL-M-core-Z	concordant	133	47	22	0.36	0.1	0.6	0.19088	0.00246	2.04952	0.03153	0.602	1124.9	13.3
J1738-18.1	CL-M-core-Z	Pb-loss (recent)	510	45	77	0.09	0.0	1.0	0.17556	0.00253	1.82019	0.02739	0.688	1042.4	13.9
J1738-19.1	CL-D-core-UZ	concordant	333	138	55	0.43	0.1	-1.8	0.18960	0.00476	1.95087	0.05155	0.684	1118.6	25.9
J1738-2.1	CL-B-core-Z	Pb-loss (recent)	306	58	37	0.20	0.1	-0.2	0.14028	0.00775	1.29903	0.09027	0.572	845.9	44.0
J1738-20.1	CL-M-core-Z	Pb-loss (recent)	575	162	77	0.29	0.1	2.4	0.15471	0.00228	1.54801	0.02516	0.653	926.7	12.7
J1738-21.1	CL-M-core-Z	Pb-loss (ancient)	254	28	29	0.11	0.0	5.6	0.13108	0.00468	1.28994	0.08765	0.378	793.8	26.7
J1738-22.1	CL-M-core-Z	Pb-loss (recent)	279	51	37	0.19	**[0.4]**	5.4	0.15081	0.00258	1.56616	0.03205	0.601	905.5	14.5
J1738-23.1	CL-M-core-Z	Pb-loss (recent)	511	69	71	0.14	0.0	1.8	0.15980	0.00243	1.60954	0.02691	0.654	955.4	13.5
J1738-24.1	CL-M-core-Z	Pb-loss (ancient)	241	30	22	0.13	0.1	4.0	0.10736	0.00192	0.96364	0.02351	0.529	656.6	11.2
J1738-25.1	CL-D-core-Z	Pb-loss (recent)	574	181	78	0.32	**[0.4]**	5.0	0.15600	0.00248	1.63618	0.05918	0.317	934.5	13.8
J1738-26.1	CL-M-core-Z	Pb-loss (recent)	217	54	30	0.25	0.1	4.4	0.15927	0.00247	1.66833	0.03180	0.586	951.8	13.7
J1738-3.1	CL-D-rim-UZ	concordant (young)	3610	19	288	0.01	0.0	-1.6	0.09022	0.00176	0.71473	0.01438	0.700	556.8	10.4
J1738-4.1	CL-M-core-Z	Pb-loss (recent)	419	57	50	0.14	0.2	8.2	0.13920	0.00363	1.46255	0.03938	0.698	838.4	20.6
J1738-5.1	CL-M-core-Z	Pb-loss (recent)	432	168	62	0.40	0.1	2.0	0.16720	0.00398	1.72246	0.04338	0.680	996.1	22.0
J1738-6.1	CL-M-core-Z	Pb-loss (ancient)	434	68	52	0.16	0.1	5.4	0.13929	0.00373	1.39922	0.04002	0.673	840.0	21.1
J1738-7.1	CL-D-core-UZ	Pb-loss (ancient)	1657	73	178	0.04	0.1	5.4	0.12406	0.00361	1.19119	0.03555	0.702	753.2	20.7
J1738-8.1	CL-M-core-Z	Pb-loss (recent)	276	82	36	0.31	0.1	5.8	0.15084	0.00299	1.57826	0.03697	0.610	904.6	16.8
J1738-9.1	CL-M-core-Z	Pb-loss (recent)	213	45	31	0.22	0.0	2.2	0.16889	0.00614	1.75670	0.06645	0.692	1005.6	34.0

(1) CL-B/M/D = bright/medium/dark; Z = zoned, UZ = unzoned, SZ = sector zoned

(2) f206_4 is the percentage of common Pb estimated from the 204 counts. In bulb and paranthesis where they have been corrected for

(3) Ratios after correction. Yellow are corrected with 204 corrected ratios

Grey analyses are excluded due to age error > 5% at 2 σ

Table 4 U-Pb SHRIMP zircon data J1773

									Radiogenic (corrected) ratio (208-corrected)[3]					Calculated ages	
Sample ID	**Grain characteristics in CL[1]**	**Comment**	**U (ppm)**	**Th (ppm)**	**206Pb (ppm)**	**Th/U**	**f206_4[2]**	**% discord.**	**207Pb/235U**	**±err**	**206Pb/238U**	**±err**	**rho_8cor**	**206Pb/238U**	**±err**
J1773-1.1	CL-D-Z? high U ppm	Pb-loss	7506	489	573	0.07	0.0	2.6	0.64511	0.00776	0.07941	0.00088	0.665	564.1	6.2
J1773-10.1	CL-D-Z? high U ppm	concordant	7829	517	634	0.07	0.0	0.2	0.66620	0.01241	0.08357	0.00146	0.674	522.9	11.8
J1773-11.1	CL-D-Z? high U ppm	concordant	6560	460	525	0.07	0.0	-1.0	0.66931	0.01307	0.08495	0.00150	0.651	497.1	16.6
J1773-12.1	CL-D-Z? high U ppm	concordant	8222	485	660	0.06	0.0	0.0	0.65054	0.01224	0.08218	0.00148	0.688	507.3	9.2
J1773-13.1	CL-D-Z? high U ppm	concordant	7915	535	640	0.07	0.0	-0.8	0.65674	0.01206	0.08339	0.00144	0.679	496.1	10.8
J1773-14.1	CL-D-Z? high U ppm	concordant	8461	530	701	0.06	0.0	-1.6	0.65884	0.01059	0.08436	0.00127	0.675	477.5	9.4
J1773-15.1	CL-D-Z? high U ppm	concordant	7592	592	600	0.08	0.0	-1.2	0.63989	0.01143	0.08207	0.00138	0.676	474.1	10.8
J1773-16.1	CL-D-Z? high U ppm	concordant	7674	580	614	0.08	0.0	-0.8	0.65133	0.01273	0.08286	0.00151	0.672	492.1	13.2
J1773-17.1	CL-D-Z? high U ppm	concordant	8456	695	686	0.08	0.0	-1.4	0.64455	0.01178	0.08262	0.00142	0.675	475.1	11.6
J1773-18.1	CL-D-Z? high U ppm	concordant	7874	528	633	0.07	0.0	-2.2	0.64098	0.01178	0.08291	0.00144	0.681	455.1	10.6
J1773-19.1	CL-D-Z? high U ppm	concordant	7497	456	602	0.06	0.0	-1.8	0.64907	0.01175	0.08348	0.00145	0.689	467.9	8.4
J1773-2.1	CL-D-Z? high U ppm	concordant	7239	396	555	0.06	0.0	0.4	0.63556	0.01451	0.08024	0.00176	0.691	508.7	11.8
J1773-20.1	CL-D-Z? high U ppm	concordant	7901	318	624	0.04	0.0	-2.2	0.62561	0.01095	0.08143	0.00136	0.689	441.3	7.8
J1773-3.1	CL-D-Z? high U ppm	concordant	7972	554	651	0.07	0.0	0.4	0.67159	0.01259	0.08403	0.00150	0.686	528.5	9.6
J1773-4.1	CL-D-Z? high U ppm	concordant	6830	415	541	0.06	0.0	0.2	0.66559	0.01333	0.08357	0.00156	0.672	520.7	13.4
J1773-5.1	CL-D-Z? high U ppm	concordant	7490	538	597	0.07	0.0	0.0	0.65933	0.01250	0.08298	0.00150	0.686	515.7	10.0
J1773-6.1	CL-D-Z? high U ppm	concordant	6210	416	490	0.07	0.0	-0.2	0.67137	0.01134	0.08441	0.00136	0.685	517.9	8.2
J1773-7.1	CL-D-Z? high U ppm	concordant	8300	445	678	0.06	0.0	-0.6	0.65916	0.01364	0.08345	0.00165	0.690	502.7	10.4
J1773-8.1	CL-D-Z? high U ppm	concordant	7815	583	632	0.08	0.1	-0.2	0.66267	0.01103	0.08348	0.00130	0.675	513.5	10.0
J1773-9.1	CL-D-Z? high U ppm	concordant	6187	374	479	0.06	0.0	-0.4	0.65472	0.01555	0.08286	0.00186	0.680	503.5	15.0

(1) CL-B/M/D = bright/medium/dark; Z = zoned, UZ = unzoned, SZ = sector zoned

(2) f206_4 is the percentage of common Pb estimated from the 204 counts. In bulb and paranthesis where they have been corrected for

(3) Ratios after correction. All samples are used with 208-corrected ratios

Table 5 U-Pb SHRIMP zircon data J1782

									Radiogenic (corrected) ratio (208-corrected)[3]					Calculated ages	
Sample ID	**Grain characteristics in CL[1]**	**Comment**	**U (ppm)**	**Th (ppm)**	**206Pb (ppm)**	**Th/U**	**f206_4[2]**	**% discord.**	**206Pb/238U**	**±err**	**207Pb/235U**	**±err**	**rho_8cor**	**206Pb/238U**	**±err**
J1782-1.1	CL-M-core-Z	Pb-loss	393	37	50	0.10	0.1	-6.0	0.14825	0.00477	1.28751	0.06044	0.494	891.1	26.8
J1782-10.1	CL-M-core-Z	concordant	417	186	50	0.46	0.1	-0.6	0.17034	0.00185	1.69995	0.03314	0.401	1014.0	10.2
J1782-11.1	CL-M-core-Z	Pb-loss (ancient)	614	60	50	0.10	0.0	1.6	0.17955	0.00102	1.90144	0.02894	0.269	1064.5	5.6
J1782-12.1	CL-M-core-Z	Pb-loss (ancient)	283	75	50	0.27	0.1	0.4	0.13711	0.00503	1.26901	0.08630	0.388	828.3	28.5
J1782-13.1	CL-M-core-Z	Pb-loss (ancient)	290	51	50	0.18	0.1	1.8	0.12472	0.00501	1.13713	0.06020	0.546	757.7	28.8
J1782-14.1	CL-B-core-Z	Pb-loss (ancient)	167	64	50	0.39	0.0	4.6	0.13359	0.00455	1.30252	0.07454	0.428	808.3	25.9
J1782-15.1	CL-M-core-Z	Pb-loss (recent)	800	123	50	0.16	0.0	-1.0	0.16541	0.00229	1.61767	0.03775	0.427	986.8	12.7
J1782-16.1	CL-M-core-Z	Pb-loss (ancient)	124	41	50	0.34	0.2	2.4	0.11744	0.00474	1.06062	0.06554	0.470	715.8	27.4
J1782-17.1	CL-B-core-Z	Pb-loss (ancient)	121	34	50	0.29	0.1	4.4	0.15100	0.01352	1.54428	0.18984	0.524	906.6	76.2
J1782-18.1	CL-M-core-Z	Pb-loss (ancient)	126	34	50	0.28	0.1	-0.8	0.16579	0.00752	1.62633	0.12188	0.436	988.9	41.7
J1782-19.1	CL-M-core-Z	concordant	215	102	50	0.49	0.1	0.2	0.17075	0.00236	1.72402	0.04174	0.410	1016.2	12.9
J1782-2.1	CL-M-core-Z	concordant	368	126	50	0.35	0.0	-0.2	0.17207	0.00165	1.73276	0.02402	0.498	1023.5	9.1
J1782-20.1	CL-M-core-Z	Pb-loss (ancient)	580	150	50	0.27	0.0	5.0	0.10111	0.00196	0.90388	0.02731	0.462	620.9	11.5
J1782-21.1	CL-M-core-Z	Pb-loss (recent)	188	46	50	0.25	0.1	8.6	0.14727	0.00286	1.59409	0.07699	0.289	885.6	16.0
J1782-22.1	CL-D-core-Z	Pb-loss (ancient)	700	300	50	0.44	0.0	3.0	0.13188	0.00126	1.25050	0.02562	0.336	798.6	7.2
J1782-23.1	CL-D-core-Z	Pb-loss (ancient)	343	95	50	0.28	0.0	1.4	0.13440	0.00274	1.25061	0.04481	0.410	812.9	15.6
J1782-24.1	CL-M-core-Z	concordant	241	105	50	0.45	0.1	0.2	0.17080	0.00326	1.72815	0.05189	0.458	1016.5	18.0
J1782-25.1	CL-M-core-Z	Pb-loss (recent)	474	258	50	0.56	0.0	1.8	0.16601	0.00175	1.69773	0.03546	0.363	990.1	9.7
J1782-26.1	CL-B-core-Z	concordant	242	76	50	0.32	0.0	-1.4	0.17940	0.00304	1.80757	0.05356	0.411	1063.7	16.6
J1782-27.1	CL-B-core-Z	concordant	130	44	50	0.35	0.1	-2.2	0.17781	0.00443	1.76555	0.09547	0.332	1055.0	24.3
J1782-28.1	CL-D-core-UZ	concordant (young)	1227	345	50	0.29	0.0	-0.6	0.09933	0.00105	0.81683	0.01678	0.371	610.5	6.2
J1782-29.1	CL-B-core-Z	Pb-loss (ancient)	166	49	50	0.31	0.1	-4.4	0.17703	0.00513	1.69632	0.08536	0.415	1050.7	28.1
J1782-3.1	CL-M-core-Z	Pb-loss (recent)	366	185	50	0.52	0.1	0.6	0.15887	0.00111	1.56256	0.02428	0.325	950.5	6.2
J1782-4.1	CL-B-core-Z	concordant	110	52	50	0.49	0.2	-0.8	0.18207	0.00418	1.86750	0.07385	0.418	1078.3	22.9
J1782-5.1	CL-M-core-Z	Pb-loss (ancient)	471	80	50	0.18	0.1	4.0	0.14021	0.00175	1.38005	0.03703	0.335	845.9	9.9
J1782-6.1	CL-M-core-Z	Pb-loss (ancient)	450	54	50	0.12	0.0	-2.6	0.17525	0.00512	1.71832	0.06146	0.588	1041.0	28.1
J1782-7.1	CL-B-core-Z	concordant	118	30	50	0.26	0.1	-7.2	0.17167	0.00283	1.55555	0.06509	0.284	1021.3	15.6
J1782-8.1	CL-M-core-Z	Pb-loss (ancient)	418	64	50	0.16	0.1	5.8	0.13495	0.01031	1.34833	0.12103	0.613	816.1	58.9
J1782-9.1	CL-M-core-Z	Pb-loss (ancient)	540	60	50	0.11	0.0	1.6	0.12217	0.00217	1.10356	0.04361	0.324	743.1	12.5

(1) CL-B/M/D = bright/medium/dark; Z = zoned, UZ = unzoned, SZ = sector zoned

(2) f206_4 is the percentage of common Pb estimated from the 204 counts. In bulb and paranthesis where they have been corrected for

(3) Ratios after correction. 208-corrected ratios used for all analyses

Grey analyses are excluded due to age error > 5% at 2 σ

Table 6 U-Pb SHRIMP zircon data J1793

									Radiogenic (corrected) ratio[3]					Calculated ages	
Sample ID	**Grain characteristics in CL[1]**	**Comment**	**U (ppm)**	**Th (ppm)**	**206Pb (ppm)**	**Th/U**	**f206_4[2]**	**% discord.**	**206Pb/238U**	**±err**	**207Pb/235U**	**±err**	**rho**	**206Pb/238U**	**±err**
J1793-1.1	CL-B-core-Z	concordant	215	87	36	0.42	0.1	0.0	0.19110	0.00153	2.03831	0.02270	0.519	1127.3	8.3
J1793-10.1	CL-M-core-Z	concordant	254	104	41	0.42	0.1	-0.2	0.18697	0.00226	1.96192	0.02620	0.651	1104.9	12.2
J1793-11.1	CL-M-core-Z	concordant	155	76	25	0.50	0.1	0.2	0.18669	0.00322	1.96876	0.03817	0.640	1103.4	17.5
J1793-12.1	CL-B-core-Z	Pb-loss (recent)	173	75	27	0.44	0.1	1.6	0.18022	0.00226	1.91365	0.03185	0.542	1068.2	12.3
J1793-13.1	CL-M-core-Z	Pb-loss (recent)	215	111	36	0.53	0.1	-0.6	0.19588	0.00211	2.09101	0.02450	0.662	1153.1	11.4
J1793-14.1	CL-M-core-Z	concordant	185	89	31	0.49	0.1	0.0	0.19046	0.00085	2.02627	0.01872	0.349	1123.8	4.6
J1793-15.1	CL-M-core-Z	concordant	256	169	42	0.68	0.0	-0.2	0.18986	0.00214	2.00651	0.02707	0.603	1120.6	11.6
J1793-16.1	CL-M-core-Z	concordant	173	82	28	0.49	0.1	0.4	0.18966	0.00186	2.02812	0.02199	0.651	1119.5	10.1
J1793-17.1	CL-B-core-Z	concordant	255	108	42	0.44	0.1	0.2	0.18955	0.00298	2.01894	0.03435	0.666	1119.0	16.2
J1793-18.1	CL-M-core-Z	concordant	201	83	33	0.42	0.1	0.2	0.19032	0.00193	2.02935	0.02451	0.606	1123.1	10.5
J1793-19.1	CL-M-core-Z	concordant	236	67	38	0.29	0.1	0.0	0.18439	0.00263	1.92551	0.02902	0.682	1090.9	14.3
J1793-2.1	CL-B-core-Z	Pb-loss (recent)	166	66	25	0.41	0.1	2.6	0.17549	0.00250	1.86987	0.02791	0.688	1042.3	13.8
J1793-20.1	CL-M-core-Z	concordant	226	83	37	0.37	0.1	1.4	0.18906	0.00246	2.04710	0.03146	0.611	1116.3	13.4
J1793-21.1	CL-M-core-Z	Pb-loss (recent)	225	70	38	0.32	0.1	-2.2	0.19527	0.00247	2.02920	0.03152	0.585	1149.8	13.3
J1793-22.1	CL-M-core-Z	Pb-loss (recent)	226	94	38	0.42	0.0	-2.0	0.19319	0.00196	2.00265	0.02310	0.632	1138.6	10.5
J1793-23.1	CL-D-core-Z	concordant	299	123	48	0.42	0.1	0.4	0.18612	0.00178	1.97001	0.02115	0.641	1100.3	9.7
J1793-24.1	CL-M-core-Z	Pb-loss (recent)	242	100	38	0.42	0.1	1.0	0.18309	0.00179	1.93782	0.02667	0.511	1083.9	9.8
J1793-25.1	CL-M-core-Z	Pb-loss (recent)	183	78	29	0.44	0.1	1.0	0.18243	0.00140	1.93059	0.01827	0.583	1080.2	7.6
J1793-25.2	CL-D-rim-UZ	concordant (young)	1779	16	141	0.01	0.0	0.0	0.09176	0.00098	0.74632	0.00859	0.667	566.0	5.8
J1793-26.1	CL-M-core-Z	concordant	226	108	36	0.49	0.1	0.0	0.18608	0.00189	1.95409	0.02357	0.608	1100.1	10.3
J1793-27.1	CL-M-core-Z	concordant	153	77	25	0.51	0.1	0.4	0.18941	0.00227	2.02181	0.03553	0.491	1118.2	12.3
J1793-28.1	CL-M-core-Z	Pb-loss (recent)	168	80	26	0.49	0.0	1.8	0.18266	0.00153	1.95983	0.02154	0.547	1081.5	8.3
J1793-3.1	CL-B-core-Z	concordant	331	134	53	0.41	0.1	1.0	0.18433	0.00259	1.95922	0.03308	0.598	1090.6	14.1
J1793-4.1	CL-B-core-Z	concordant	195	93	31	0.49	0.1	0.0	0.18709	0.00156	1.97174	0.02109	0.561	1105.6	8.5
J1793-5.1	CL-B-core-Z	concordant	250	102	40	0.42	0.1	0.6	0.18490	0.00398	1.95550	0.04457	0.680	1093.7	21.7
J1793-6.1	CL-B-core-Z	concordant	168	70	27	0.43	0.1	1.4	0.18793	0.00421	2.02842	0.04953	0.661	1110.2	22.9
J1793-7.1	CL-B-core-Z	concordant	228	106	36	0.48	0.1	1.2	0.18338	0.00289	1.95335	0.03248	0.682	1085.4	15.7
J1793-8.1	CL-M-core-Z	concordant	194	81	31	0.43	0.1	2.6	0.18413	0.00260	2.00596	0.03022	0.675	1089.5	14.2
J1793-9.1	CL-M-core-Z	concordant	242	156	39	0.66	0.1	0.8	0.18484	0.00203	1.95814	0.02310	0.671	1093.3	11.0
J1793-9.2	CL-M-rim-Z	Pb-loss (recent)	971	249	151	0.26	0.0	1.6	0.18038	0.00331	1.91389	0.03608	0.700	1069.1	18.1

(1) CL-B/M/D = bright/medium/dark; Z = zoned, UZ = unzoned, SZ = sector zoned

(2) f206_4 is the percentage of common Pb estimated from the 204 counts. In bulb and paranthesis where they have been corrected for

(3) Ratios after correction. Common Pb uncorrected ratios used for all analyses

Table 7 U-Pb SHRIMP zircon data J1807

									Radiogenic (corrected) ratio[3]					Calculated ages	
Sample ID	**Grain characteristics in CL[1]**	**Comment**	**U (ppm)**	**Th (ppm)**	**206Pb (ppm)**	**Th/U**	**f206_4[2]**	**% discord.**	**206Pb/238U**	**±err**	**207Pb/235U**	**±err**	**rho**	**206Pb/238U**	**±err**
J1807-1.1	CL-D-rim-UZ	concordant	3275	132	243	0.04	0.0	1.6	0.08458	0.00160	0.68836	0.01359	0.691	523.3	9.5
J1807-10.2	CL-D-rim-UZ	concordant	3155	149	228	0.05	0.0	1.0	0.08246	0.00132	0.66216	0.01098	0.695	510.6	7.9
J1807-11.1	CL-D-rim-UZ	concordant	1281	166	95	0.13	0.1	-0.4	0.08592	0.00102	0.68509	0.00894	0.653	531.2	6.1
J1807-12.1	CL-D-rim-UZ	concordant	2838	23	210	0.01	0.0	0.6	0.08502	0.00151	0.68360	0.01262	0.694	525.8	9.0
J1807-13.1	CL-D-rim-UZ	Pb-loss (recent)	5078	261	375	0.05	0.0	0.4	0.08120	0.00119	0.64464	0.01005	0.676	503.3	7.1
J1807-14.1	CL-M-core-Z	concordant (Old)	370	129	61	0.36	0.1	0.0	0.19253	0.00286	2.06186	0.03284	0.672	1134.6	15.5
J1807-15.1	CL-D-rim-UZ	concordant	1201	160	87	0.14	0.1	1.0	0.08436	0.00110	0.68088	0.00932	0.684	522.1	6.6
J1807-16.1	CL-D-core-Z	concordant (Old)	1019	298	168	0.30	0.0	-0.2	0.19061	0.00176	2.02233	0.02101	0.641	1124.6	9.6
J1807-17.1	CL-D-rim-UZ	concordant	3172	117	238	0.04	0.0	-0.4	0.08579	0.00146	0.68314	0.01202	0.698	530.4	8.7
J1807-18.1	CL-D-rim-UZ	concordant	3069	131	228	0.04	0.1	1.2	0.08528	0.00137	0.69134	0.01140	0.701	526.9	8.1
J1807-19.1	CL-D-rim-UZ	concordant	2309	74	173	0.03	0.1	0.0	0.08696	0.00074	0.69784	0.00686	0.623	537.4	4.4
J1807-2.1	CL-D-rim-UZ	concordant	1080	125	77	0.12	0.0	1.2	0.08262	0.00128	0.66522	0.01103	0.670	511.5	7.6
J1807-20.1	CL-D-rim-UZ	concordant	1926	229	141	0.12	0.0	0.6	0.08473	0.00086	0.68103	0.00793	0.629	524.3	5.1
J1807-21.1	CL-M-core-Z	Pb-loss (recent)	461	85	72	0.19	0.1	5.0	0.18230	0.00212	2.06128	0.03621	0.477	1080.3	11.6
J1807-22.1	CL-M-core-Z	concordant (Old)	278	89	46	0.33	0.1	2.2	0.19113	0.00323	2.11154	0.04493	0.572	1126.2	17.5
J1807-23.1	CL-D-rim-UZ	concordant	6318	288	492	0.05	0.0	-0.4	0.08336	0.00147	0.65993	0.01199	0.698	516.3	8.8
J1807-24.1	CL-M-core-Z	Pb-loss (recent)	507	122	79	0.25	0.1	1.8	0.17993	0.00263	1.91569	0.03530	0.570	1066.6	14.4
J1807-25.1	CL-D-rim-UZ	concordant	4120	37	316	0.01	0.0	0.0	0.08606	0.00132	0.68958	0.01092	0.700	532.1	7.9
J1807-26.1	CL-D-rim-UZ	concordant	4259	58	325	0.01	0.0	-0.4	0.08518	0.00142	0.67717	0.01205	0.672	526.9	8.4
J1807-27.1	CL-D-rim-UZ	concordant	3180	120	232	0.04	0.0	0.4	0.08339	0.00125	0.66635	0.01036	0.693	516.1	7.4
J1807-3.1	CL-D-rim-UZ	concordant	2809	101	209	0.04	0.0	-0.2	0.08559	0.00091	0.68279	0.00779	0.669	529.3	5.3
J1807-4.1	CL-M-core-Z	Pb-loss (recent)	456	111	71	0.25	0.1	1.6	0.18076	0.00238	1.92086	0.02880	0.631	1069.7	13.0
J1807-5.1	CL-D-rim-UZ	Pb-loss (ancient)	2388	101	198	0.04	**[0.6]**	0.4	0.09373	0.00153	0.79800	0.02281	0.411	577.6	9.1
J1807-6.1	CL-D-rim-UZ	concordant	5916	71	469	0.01	0.0	1.0	0.08551	0.00113	0.69241	0.00952	0.691	528.6	6.7
J1807-7.1	CL-D-rim-UZ	concordant	1815	179	130	0.10	0.0	0.6	0.08283	0.00101	0.66278	0.00876	0.666	512.8	6.0
J1807-8.1	CL-D-rim-UZ	concordant	2664	101	198	0.04	0.0	1.4	0.08587	0.00085	0.69948	0.00748	0.670	530.6	5.1
J1807-9.1	CL-D-rim-UZ	concordant	4642	106	358	0.02	0.0	0.4	0.08545	0.00078	0.68621	0.00680	0.667	528.7	4.7

(1) CL-B/M/D = bright/medium/dark; Z = zoned, UZ = unzoned, SZ = sector zoned

(2) f206_4 is the percentage of common Pb estimated from the 204 counts. In bulb and paranthesis where they have been corrected for

(3) Ratios after correction. Orange are corrected with 208-corrected ratios

Table 8 U-Pb SHRIMP zircon data J1848

									Radiogenic (corrected) ratio (208-corrected)[3]					Calculated ages (208)	
Sample ID	**Grain characteristics in CL[1]**	**Comment**	**U (ppm)**	**Th (ppm)**	**206Pb (ppm)**	**Th/U**	**f206_4[2]**	**% discord.**	**206Pb/238U**	**±err**	**207Pb/235U**	**±err**	**rho_4cor**	**206Pb/238U**	**±err**
J1848-1.1	CL-M-core-Z	concordant (old)	294	166	27	0.58	0.3	1.0	0.10538	0.00096	0.90243	0.02054	0.288	645.9	5.6
J1848-10.1	CL-D-rim-Z	concordant (young)	364	82	29	0.23	0.0	2.0	0.09075	0.00067	0.75502	0.01062	0.377	560.0	4.0
J1848-11.1	CL-B-core-Z	concordant (old)	187	79	17	0.43	0.2	2.6	0.10367	0.00118	0.90261	0.03027	0.245	635.9	6.9
J1848-12.1	CL-B-core-Z	concordant	164	79	16	0.50	0.0	-1.0	0.11198	0.00142	0.94869	0.02720	0.319	684.3	8.3
J1848-12.2	CL-M-rim-Z	concordant (young)	260	55	21	0.22	0.3	-0.2	0.09249	0.00087	0.75170	0.01521	0.334	570.3	5.2
J1848-13.1	CL- M-rim-Z	concordant (young)	292	71	23	0.25	0.1	0.2	0.09164	0.00126	0.74579	0.01794	0.411	565.2	7.4
J1848-14.1	CL-M-core-UZ	concordant (old)	300	103	26	0.35	0.2	3.0	0.10053	0.00103	0.87120	0.02454	0.261	617.5	6.0
J1848-15.1	CL-B-core-Z	Pb-loss	148	67	16	0.46	0.1	4.8	0.12390	0.00953	1.18047	0.17781	0.368	753.0	55.0
J1848-15.2	CL-M-rim-Z	concordant (young)	251	49	20	0.20	0.2	0.8	0.09147	0.00127	0.75165	0.01474	0.509	564.2	7.5
J1848-16.1	CL-M-rim-Z	concordant (young)	201	43	16	0.22	0.0	-0.2	0.08980	0.00066	0.72418	0.01051	0.363	554.3	3.9
J1848-17.1	CL-M-core-Z	concordant	213	119	20	0.57	-0.2	2.6	0.11007	0.00173	0.97530	0.03366	0.329	673.2	10.1
J1848-17.2	CL-M-rim-UZ	concordant (young)	274	53	22	0.20	-0.1	-0.4	0.09266	0.00077	0.75077	0.01320	0.340	571.3	4.6
J1848-18.1	CL-M-core-Z	concordant (young)	163	26	13	0.17	0.5	1.2	0.09027	0.00101	0.74346	0.01730	0.346	557.1	5.9
J1848-19.1	CL-M-rim-UZ	concordant (young)	141	30	11	0.22	0.3	0.2	0.08997	0.00100	0.72914	0.01422	0.410	555.4	5.9
J1848-2.1	CL-M-core-UZ	concordant (young)	210	34	16	0.17	0.2	2.8	0.09028	0.00082	0.75954	0.01144	0.433	557.2	4.9
J1848-20.1	CL-M-core-Z	concordant	233	110	20	0.49	0.5	0.6	0.09776	0.00114	0.81362	0.03251	0.211	601.3	6.7
J1848-21.1	CL-M-rim-UZ	concordant (young)	233	47	18	0.21	-0.1	1.8	0.09121	0.00119	0.75820	0.01655	0.432	562.7	7.1
J1848-22.1	CL-M-rim-UZ	concordant (young)	311	70	25	0.23	0.1	0.0	0.09127	0.00135	0.74088	0.01461	0.540	563.1	8.0
J1848-23.1	CL-M-rim-Z	concordant (old)	425	103	39	0.25	0.0	-2.0	0.10476	0.00123	0.85818	0.02424	0.300	642.2	7.2
J1848-24.1	CL-M-core-UZ	concordant (old)	371	198	33	0.55	0.4	-0.4	0.10386	0.00106	0.86800	0.02102	0.305	637.0	6.2
J1848-25.1	CL-B-core-Z	Pb-loss	356	117	34	0.34	0.2	2.0	0.11198	0.00339	0.98804	0.04431	0.487	684.2	19.7
J1848-25.2	CL-M-rim-Z	concordant (young)	343	68	27	0.20	0.2	2.6	0.09154	0.00094	0.76983	0.01146	0.495	564.6	5.5
J1848-3.1	CL-M-core-UZ	Pb-loss	466	125	40	0.27	0.1	2.4	0.09965	0.00300	0.85499	0.04682	0.396	612.3	17.6
J1848-4.1	CL-D-rim-UZ	concordant (young)	383	73	31	0.19	0.1	2.4	0.09356	0.00235	0.78963	0.02725	0.524	576.6	13.9
J1848-5.1	CL-B-core-Z	concordant	114	37	9	0.33	0.4	6.4	0.09386	0.00192	0.83880	0.02967	0.416	578.3	11.3
J1848-5.2	CL-M-rim-UZ	Pb-loss	208	39	16	0.19	-0.1	0.6	0.08623	0.00291	0.69511	0.02935	0.575	533.2	17.3
J1848-6.1	CL-M-rim-UZ	concordant (young)	279	49	22	0.18	0.1	1.4	0.09001	0.00097	0.74132	0.01540	0.373	555.6	5.7
J1848-7.1	CL-B-rim-Z	concordant (young)	291	127	23	0.45	0.2	2.8	0.08995	0.00109	0.75493	0.01897	0.346	555.2	6.4
J1848-7.2	CL-D-rim-UZ	concordant	687	51	52	0.08	0.2	0.0	0.08703	0.00129	0.69868	0.01342	0.554	538.0	7.7
J1848-8.1	CL-B-core-Z	Pb-loss	177	50	15	0.29	0.4	5.0	0.10022	0.00401	0.89255	0.05158	0.498	615.7	23.6
J1848-8.2	CL-M-rim-Z	concordant (young)	191	37	15	0.20	0.0	-0.6	0.09159	0.00066	0.73824	0.01270	0.301	564.9	3.9
J1848-9.1	CL-B-core-Z	concordant (young)	105	35	8	0.34	0.3	1.0	0.09183	0.00125	0.75638	0.06369	0.117	566.4	7.5
J1848-9.2	CL-M-rim-Z	concordant (young)	321	59	26	0.19	0.2	-1.8	0.09178	0.00116	0.72965	0.01278	0.521	566.0	6.8

(1) CL-B/M/D = bright/medium/dark; Z = zoned, UZ = unzoned, SZ = sector zoned

(2) f206_4 is the percentage of common Pb estimated from the 204 counts. In bulb and paranthesis where they have been corrected for

(3) Ratios after correction. All samples are used with 208-corrected ratios

Grey analyses are excluded due to age error > 5% at 2 σ

Table 9 U-Pb SHRIMP zircon data J1937

									Radiogenic (corrected) ratio (208-corrected)[3]					Calculated ages	
Sample ID	**Grain characteristics in CL[1]**	**Comment**	**U (ppm)**	**Th (ppm)**	**206Pb (ppm)**	**Th/U**	**f206_4[2]**	**% discord.**	**206Pb/238U**	**±err**	**207Pb/235U**	**±err**	**rho_4cor**	**206Pb/238U**	**±err**
J1937-10.1	CL-D-rim-UZ	concordant	342	191	28	0.57	0.4	-1.4	0.09462	0.00115	0.76131	0.02304	0.289	582.8	6.8
J1937-11.1	CL-M-core-UZ	concordant	207	74	17	0.37	0.3	-0.6	0.09519	0.00101	0.77455	0.01599	0.371	586.2	6.0
J1937-12.1	CL-M-rim-UZ	concordant	220	136	18	0.63	0.5	0.0	0.09433	0.00100	0.77327	0.02320	0.255	581.1	5.9
J1937-13.1	CL-B-rim-UZ	concordant	66	33	5	0.52	2.0	-2.2	0.09430	0.00192	0.75097	0.04198	0.262	580.9	11.3
J1937-14.1	CL-D-core-UZ	concordant	213	123	18	0.59	0.4	3.0	0.09966	0.00105	0.86178	0.02213	0.295	612.4	6.1
J1937-15.1	CL-M-rim-UZ	concordant	217	124	18	0.59	0.8	0.8	0.09409	0.00079	0.77797	0.01582	0.296	579.7	4.7
J1937-16.1	CL-M-rim-UZ	concordant	174	76	14	0.45	0.6	3.8	0.09164	0.00060	0.78382	0.01480	0.250	565.2	3.5
J1937-17.1	CL-M-rim-UZ	concordant	256	131	21	0.52	0.6	-1.8	0.09526	0.00097	0.76327	0.01740	0.320	586.6	5.7
J1937-18.1	CL-M-rim-UZ	concordant	160	77	13	0.49	0.9	-0.8	0.09385	0.00150	0.75962	0.03259	0.269	578.3	8.9
J1937-19.1	CL-M-core-UZ	concordant	200	83	17	0.43	0.4	0.4	0.09637	0.00069	0.79726	0.01805	0.226	593.1	4.0
J1937-20.1	CL-M-core-UZ	concordant	193	28	17	0.15	0.4	-2.4	0.09968	0.00133	0.80134	0.01713	0.450	612.5	7.8
J1937-21.1	CL-B-rim-Z	slight pb loss	82	56	7	0.70	1.1	2.8	0.09443	0.00164	0.80195	0.03675	0.273	581.7	9.7
J1937-22.1	CL-M-rim-UZ	concordant	218	116	18	0.55	0.4	-0.6	0.09514	0.00124	0.77399	0.02540	0.287	585.9	7.3
J1937-23.1	CL-D-core-UZ	concordant	332	182	27	0.56	0.1	1.2	0.09451	0.00090	0.78728	0.06207	0.087	582.2	5.3
J1937-23.2	CL-M-rim-UZ	concordant	169	87	14	0.53	0.1	-0.4	0.09343	0.00091	0.75951	0.02498	0.213	575.8	5.4
J1937-24.1	CL-D-core-UZ	concordant	197	97	16	0.50	0.5	0.0	0.09213	0.00154	0.74932	0.02792	0.324	568.1	9.1
J1937-24.2	CL-D-rim-UZ	concordant	337	191	28	0.58	0.0	1.0	0.09598	0.00088	0.79903	0.02215	0.239	590.8	5.2
J1937-25.1	CL-M-rim-UZ	concordant	183	68	15	0.38	0.4	1.8	0.09608	0.00131	0.81041	0.02732	0.290	591.4	7.7
J1937-26.1	CL-M-rim-UZ	concordant	178	86	16	0.49	0.3	1.2	0.10427	0.00185	0.89236	0.05986	0.191	639.4	10.8
J1937-27.1	CL-M-rim-UZ	concordant	259	103	21	0.41	0.3	1.4	0.09437	0.00126	0.78798	0.02247	0.336	581.3	7.4
J1937-28.1	CL-M-rim-UZ	slight pb loss	132	72	11	0.56	0.7	0.6	0.09340	0.00138	0.76932	0.02510	0.325	575.6	8.1
J1937-29.1	CL-M-rim-UZ	concordant	122	80	10	0.67	0.8	-0.4	0.09227	0.00103	0.74764	0.02919	0.206	569.0	6.1
J1937-30.1	CL-B-core-UZ	concordant	71	47	11	0.68	0.8	1.0	0.17683	0.00305	1.84161	0.07097	0.322	1049.6	16.7
J1937-31.1	CL-M-rim-UZ	concordant	234	119	19	0.52	0.1	2.0	0.09296	0.00157	0.77930	0.03121	0.303	573.0	9.3
J1937-32.1	CL-M-core-UZ	concordant	208	95	18	0.47	0.5	-1.2	0.09898	0.00215	0.80862	0.03627	0.349	608.4	12.6
J1937-1.1	CL-D-core-UZ	concordant	450	206	36	0.47	0.2	1.8	0.09273	0.00145	0.77519	0.02651	0.329	571.7	8.6
J1937-2.1	CL-M-core-UZ	concordant	192	125	15	0.67	0.5	-3.0	0.09292	0.00181	0.72941	0.04153	0.247	572.8	10.7
J1937-3.1	CL-D-core-UZ	concordant	191	97	20	0.52	0.3	6.2	0.12391	0.02988	1.20479	0.69939	0.299	753.0	173.7
J1937-4.1	CL-D-core-UZ	concordant	161	92	13	0.58	0.8	0.6	0.09323	0.00132	0.76716	0.03002	0.261	574.6	7.8
J1937-5.1	CL-D-rim-UZ	concordant	230	122	19	0.55	0.6	-1.6	0.09349	0.00142	0.74810	0.02729	0.299	576.1	8.3
J1937-6.1	CL-M-core-UZ	concordant	131	73	10	0.57	2.9	-5.8	0.09008	0.00390	0.67724	0.12112	0.174	556.0	23.1
J1937-7.1	CL-M-rim-UZ	concordant	157	76	13	0.50	0.5	1.0	0.09448	0.00130	0.78482	0.02642	0.293	582.0	7.7
J1937-8.1	CL-M-core-UZ	concordant	251	120	22	0.49	0.3	0.8	0.10056	0.00138	0.84723	0.02356	0.354	617.7	8.0
J1937-9.1	CL-M-rim-UZ	concordant	181	97	15	0.55	0.6	-1.4	0.09339	0.00081	0.74839	0.02303	0.203	575.6	4.8

(1) CL-B/M/D = bright/medium/dark; Z = zoned, UZ = unzoned, SZ = sector zoned

(2) f206_4 is the percentage of common Pb estimated from the 204 counts. In bulb and paranthesis where they have been corrected for

(3) Ratios after correction. All samples are used with 208-corrected ratios

Grey analyses are excluded due to age error > 5% at 2 σ